

DISSERTATION

QUASIDIMENSIONAL MODELING OF REACTING FUEL SPRAYS USING DETAILED
CHEMICAL KINETICS

Submitted by

Aron Peter Dobos

Department of Mechanical Engineering

In partial fulfillment of the requirements

For the Degree of Doctor of Philosophy

Colorado State University

Fort Collins, Colorado

Fall 2016

Doctoral Committee:

Advisor: Allan T. Kirkpatrick

Anthony Marchese

Xinfeng Gao

Karan Venayagamoorthy

Copyright by Aron Peter Dobos 2016

All Rights Reserved

ABSTRACT

QUASIDIMENSIONAL MODELING OF REACTING FUEL SPRAYS USING DETAILED CHEMICAL KINETICS

Since its invention in the late 1800s, the internal combustion engine has been indispensable to society for motive transport at all scales worldwide. Despite growing concern about the environmental damage caused by the pervasive use of these engines, no compelling alternative has yet emerged that matches the internal combustion engine's robustness, versatility, and high power-to-weight ratio. Consequently, as requirements on engine designs continue to increase to meet new emissions and efficiency standards, there is a strong need for computationally efficient and accurate predictive modeling of complex engine combustion processes.

This work presents an efficient approach to direct injection engine combustion simulation that uses detailed chemical kinetics with a quasidimensional fuel spray model. Instead of a full multidimensional approach that solves continuity, momentum, energy, and chemistry equations simultaneously over a fine grid, the spatial information is greatly reduced and modeled phenomenologically. The model discretizes the fuel spray into independent parcels that entrain air from the surroundings and account for liquid fuel vaporization. Gas phase species concentrations and heat release in each parcel are calculated by detailed chemical kinetic mechanisms for the fuel under consideration. Comparisons of predicted pressure, heat release, and emissions with data from diesel engine experiments show good agreement overall, and suggest that spray combustion processes can be modeled without calibration of empirical

constants at a significantly lower computational cost than with standard multidimensional tools.

The new combustion model is also used to investigate spray structure and emissions trends for biodiesel fuels in a compression ignition engine. Results underscore the complex relationships among operational parameters, fuel chemistry, and NO_x emissions, and provide further evidence of a link between stoichiometry near the flame lift-off length and formation of NO_x . In addition, fuel molecular structure is demonstrated to be a significant factor in NO_x emissions, but more robust chemical kinetic mechanisms and soot models for biodiesel are likely needed for improved predictive accuracy in modeling alternative fuels.

ACKNOWLEDGEMENTS

I am incredibly grateful for having had the opportunity to work with my advisor, Dr. Allan Kirkpatrick, over the last five years. Never would I have expected a PhD to become a fun hobby, but it turned out to be, and probably only because I could work on it with a truly nice and smart person who also enjoyed the ride.

I thank my committee members, Dr. Anthony Marchese, Dr. Xinfeng Gao, and Dr. Karan Venayagamoorthy, for their assistance and excellent recommendations, offered always most congenially and collaboratively, that resulted in much better research.

Many thanks to Dr. Rolf Reitz and Dr. Youngchul Ra for sharing CHEMKIN input files for their chemical kinetic mechanisms that were used throughout this research, and also to Dr. Hu Wang of the State Key Laboratory of Engines at Tianjin University in China, who shared CHEMKIN input files used for some comparisons in this work.

I would like to thank my employer, the National Renewable Energy Laboratory (NREL), for funding my PhD through its tuition reimbursement program, and my supervisors Laura Vimmerstedt and Nate Blair for supporting the effort and offering generous work schedule flexibility.

I am so grateful to my parents Julia and Laszlo, and sister Nora, who cheerfully suggested that I just try a little harder when equations weren't working out right, but reminded me to go to bed before our new little boys would inevitably start their middle of the night parental interactions.

My boys, Peter and Rodger, thank you for being the amazing little creatures that you are. And, to my loving wife Hillary, a simple full-hearted thank you. I am so lucky to be on this adventure of life with you. Where to shall we voyage next? I can't wait.

TABLE OF CONTENTS

Abstract	ii
Acknowledgements	iv
List of Tables	viii
List of Figures	ix
Chapter 1. Introduction	1
1.1. Preliminaries	1
1.2. Modeling Approaches	2
1.3. Alternative Fuels	6
1.4. Summary	10
Chapter 2. Modeling Approach	11
2.1. Overview	11
2.2. Thermodynamics	12
2.3. Engine Geometry	15
2.4. Chemical Kinetics	16
2.5. Gas Jets Applied to Diesel Sprays	20
2.6. Spray Modeling	26
2.7. Large Scale Fluid Motion	30
2.8. Atomization and Evaporation	34
2.9. Turbulent Combustion	39
2.10. Parcel Mixing	42
2.11. Emissions Models	44

2.12.	Heat Transfer	46
2.13.	Fuel Properties	48
2.14.	Equivalence Ratios.....	48
2.15.	Solution Procedure	50
2.16.	Calculation of Species Mole Fraction Change.....	52
2.17.	Summary	54
Chapter 3. Validation with Diesel Engine Experiments.....		55
3.1.	Overview	55
3.2.	Baseline Scenario	55
3.3.	Evaluation of Submodels.....	56
3.4.	Evaluation of Spray Structure.....	60
3.5.	Sensitivity to Key Submodels	63
3.6.	Prediction of Pollutant Emissions	67
3.7.	Optical Test Engine Evaluation	69
3.8.	Summary	71
Chapter 4. Investigation of Biodiesel Sprays.....		73
4.1.	Overview	73
4.2.	Baseline Identical Operating Conditions.....	73
4.3.	Biodiesel Spray Structure	79
4.4.	Stoichiometry at the Lift-off Length.....	81
4.5.	Comparisons Under Normalized Operating Conditions.....	84
4.6.	Fuel Molecular Structure Effects	88
4.7.	Summary	93

Chapter 5. Computational Robustness and Efficiency	94
5.1. Overview	94
5.2. Sensitivity to Discretizations	94
5.3. Sensitivity to Mixing and Entrainment Parameters	97
5.4. Computational Scalability	100
Chapter 6. Conclusions	103
References	106

LIST OF TABLES

2.1	Fuel properties.....	48
2.2	Stoichiometric air-fuel ratios for biodiesel surrogate species.....	50
3.1	Engine and model parameters.....	56
3.2	Predicted vs measured engine-out emissions.....	68
4.1	Cycle simulation metrics for diesel and biodiesel.....	75

LIST OF FIGURES

1.1	Multidimensional model of a 150cc two stroke engine showing short circuiting of charge from side intake ports to the exhaust	4
1.2	Biodiesel surrogate fuel molecules methyl decanoate ($C_{11}H_{22}O_2$) and methyl-9-decenoate ($C_{11}H_{20}O_2$).	7
2.1	Transformation of a thermodynamic zone (“parcel”) from liquid fuel to combustion products.	11
2.2	Cylinder geometry parameters.	15
2.3	Selected ignition delay comparisons between the new C++ chemistry solver versus Cantera at medium-low pressure (30 bar).	18
2.4	Selected ignition delay comparisons between the new C++ chemistry solver versus Cantera at medium high pressure (70 bar).	19
2.5	Diagram of gas jet parameters.	21
2.6	Spray parcel concept.	27
2.7	Normalized radial spray velocity profiles.	29
2.8	Influence of swirl ratio on spray tip penetration length.	30
2.9	Instantaneous swirl ratio as a function of piston geometry.	33
2.10	Turbulence intensity and squish velocity as a function of piston geometry.	33
2.11	χ^2 volume distribution function for droplets.	35
2.12	Effect of multiple droplet sizes on the fuel evaporation process.	36
2.13	Fuel properties for diesel and biodiesel as a function of temperature.	49

2.14	Block diagram of solution procedure to advance one time step.	51
3.1	Engine 1, 50 % load @ 1800 rpm, pressure and AHRR.	57
3.2	Engine 1, 900 rpm, pressure and AHRR. $\theta_i = -11$, $\theta_d = 5$, $P_{BDC} = 1.2$ bar	58
3.3	Injected, vaporized, fuel burned, and hydrocarbon burned mass fractions for the baseline case.	59
3.4	Instantaneous fractions of injected, vaporized, and burned fuel mass.	59
3.5	Predicted zone temperatures for engine 1, baseline.	60
3.6	Predicted total and radiative heat transfer for engine 1, baseline.	60
3.7	Predicted NO _x and soot emissions for engine 1, baseline case.	61
3.8	Engine 1, spray liquid mass fraction and temperature distribution.	62
3.9	Engine 1, NO _x and soot locations.	63
3.10	Engine 1, ϕ vs. temperature @ 1800 rpm (a) 25 % load, (b) 50 % load, (c) 75 % load	64
3.11	Engine 1, AHRR with and without parcel mixing model.	65
3.12	Engine 1, sensitivity to chemical kinetic mechanism, baseline conditions.	66
3.13	Engine 1, swirl ratio sensitivity.	66
3.14	Engine 1, piston bowl size sensitivity for swirl ratio of 2.	67
3.15	Engine 2, 80 % load, 1600 rpm, pressure and AHRR.	69
3.16	Engine 2, modeled soot versus NO _x tradeoff curve.	70
3.17	Engine 3, pressure and heat release rate comparison.	71

3.18	Engine 3, liquid mass fraction and instantaneous gas phase equivalence ratio inside reacting fuel spray.....	72
4.1	Comparison of diesel and biodiesel apparent heat release rates.....	75
4.2	Comparison of diesel and biodiesel pressure traces.....	76
4.3	Comparison of diesel and biodiesel mass fractions of liquid, vapor, and burned fuel.	76
4.4	Comparison of diesel and biodiesel temperatures.....	77
4.5	Comparison of diesel and biodiesel pollutant emissions.....	78
4.6	Comparison of diesel and biodiesel soot-NO _x tradeoff curve with varying start of injection timing.....	78
4.7	Comparison of diesel (left) and biodiesel (right) spray liquid lengths.....	79
4.8	Comparison of diesel (left) and biodiesel (right) temperature distributions.....	80
4.9	Comparison of diesel (left) and biodiesel (right) normalized NO _x distributions....	81
4.10	Comparison of diesel (left) and biodiesel (right) normalized soot distributions....	82
4.11	Comparison of diesel and biodiesel liquid lengths.....	82
4.12	Comparison of diesel and biodiesel flame lift-off lengths.....	83
4.13	Instantaneous equivalence ratio at the flame lift-off length, mass-weighted cross-sectional average.....	85
4.14	Relative NO _x emissions change of biodiesel compared to diesel at various IMEPs and engine speeds.....	86
4.15	Local peak temperatures at various IMEPs and engine speeds.....	86

4.16	Stoichiometry at the lift-off length at (a) 700 rpm, and (b) 1100 rpm. Both at IMEP \approx 8 bar.	87
4.17	Relative soot emissions change of biodiesel compared to diesel at various IMEPs and engine speeds.	88
4.18	Impact of fuel molecular structure on NO _x and peak temperatures at different engine speeds.	90
4.19	Impact of fuel molecular structure on apparent heat release rate shape at different engine speeds.	91
5.1	Effect of simulation step on key metrics.	95
5.2	Sensitivity of soot predictions to step size and choice of precursor molecule.	96
5.3	Effect of number of radial spray zones on key metrics.	97
5.4	NO _x , IMEP, peak temperature, and thermal efficiency as a function of parcel mixing intensity factor.	98
5.5	Comparison of heat release rate with different parcel mixing intensity factors.	99
5.6	Effect of changing the entrainment constant K_u on key metrics.	100
5.7	Effect of changing the entrainment constant K_u on heat release rate shape.	101
5.8	Scalability of decoupled parallel simulation procedure on an i7-5820k 6-core processor.	102

CHAPTER 1

INTRODUCTION

1.1. PRELIMINARIES

Despite their ubiquity, internal combustion engines have been designed largely by empiricism since their invention in the late 1800s. Often, the engine yielding the best test results out of a handful of prototypes would be put into production, and could remain in service with minor incremental modifications for several decades. With increasing concern for environmental degradation resulting from engine pollution, strict new regulatory limits on emissions and mandated increases in fuel economy have resulted in a need for a more scientific approach to engine design and optimization process. Only recently have analytical and computational tools become sufficiently sophisticated and robust enough to predict the behavior of the complex processes that unfold inside an engine's combustion chamber with enough accuracy to warrant their use. The advent of high performance computers in the 1990s coupled with advances in computational fluid dynamics (CFD) tools have enabled detailed analysis of engine flows, combustion, and pollutant formation processes. When used successfully, CFD analysis can be an accurate predictor of the particular behavior of a specific engine configuration. With great accuracy and detail, though, comes great complexity, computational burdens, debugging challenges, and difficulties in analyzing and verifying results, if not simply for the sheer volume of data generated. Consequently, a need remains for better engine simulation tools that run fast, predict behavioral trends and engine-specific performance accurately, and can be integrated into optimization frameworks that may pick out better designs while considering a much larger variable space than would be practically

possible with CFD tools. Quasidimensional models can fill this role by jettisoning the multidimensional partial differential equations governing fluid flow and solving only the energy equation for each of multiple zones with phenomenological models for the physical processes in a fuel spray.

The United States Energy Information Administration (EIA) predicts that sales of light duty vehicles powered solely by internal combustion engines will still comprise roughly 85 % of total sales in 2040 in the United States [1]. The predominance of these engines for the next several decades coupled with increasingly stringent regulation of emissions and desire for improved efficiency mandates better engine designs. Since building and testing an engine prototype remains very expensive and time consuming, there is a strong need for predictive modeling and accurate computer simulation of complex engine processes.

1.2. MODELING APPROACHES

Spray combustion technology has progressed rapidly in the past several decades, and advanced direct injection engines have become a promising pathway towards decreased fuel consumption and carbon dioxide emissions in the transportation sector. Stringent tailpipe regulations remain a very difficult hurdle to overcome even with advanced combustion and aftertreatment technologies. The complex interplay among injection, evaporation, in-cylinder flows, fuel-air mixing, and combustion and emissions processes requires detailed computer models to predict engine performance and uncover design options that may prove able to balance emissions, efficiency, and cost.

Multidimensional computational fluid dynamics (CFD) models simultaneously solve unsteady continuity, momentum, and energy equations for the flow of fluid at each cell of a spatially discretized volume. For engine simulation, these equations are extended to include

models for turbulence, combustion, multiple phase interactions, sprays, and time-variant geometry with automatic mesh modification. These models can be terrifically complex to set up, run, and debug, but can yield impressive detail in describing the specific nature of flow interactions during intake and exhaust strokes, large scale in-cylinder flows such as swirl and tumble, as well as spatial variations in combustion processes resulting from turbulence and other factors. Fig. 1.1 shows the level of detail available in the complex flow behavior predicted by a CFD model for the scavenging process in a two-stroke engine. Although the semi-empirical sub-models used within multidimensional tools often require calibrated parameters to achieve good comparison with measurements, these requirements are reduced relative to thermodynamic models since much more of the underlying physical processes are explicitly modeled. Significant advancement and interest in multidimensional models in the 1980s and 1990s yielded remarkable success in describing engine processes. Perhaps the foremost multidimensional code with specific applicability to engine simulation are the KIVA series of CFD codes developed by the Los Alamos National Laboratory [3], and the commercial Converge package [4]. These codes are designed specifically for chemically reactive sprays and dynamic meshing of valve and piston motion. Judging from publication trends in the literature, thermodynamic models somewhat fell out of favor in the 1990s and 2000s, as research appeared to gravitate towards improving multidimensional tools. However, the primary disadvantages of multidimensional modeling of engines remain today: complexity and long simulation times. Despite recent advancements, the most comprehensive application of modern multidimensional tools to internal combustion engine design and optimization by Shi et al. in [2] suggests supercomputer simulation times on the order of months to consider a sufficient variety of different engine configurations. If the goal is to explore a large design

variable space, perhaps with many variants on geometry, an approach based on multidimensional tools can quickly become a phenomenally burdensome proposition. Simpler and more robust thermodynamic models may yield insight much more quickly and reliably.

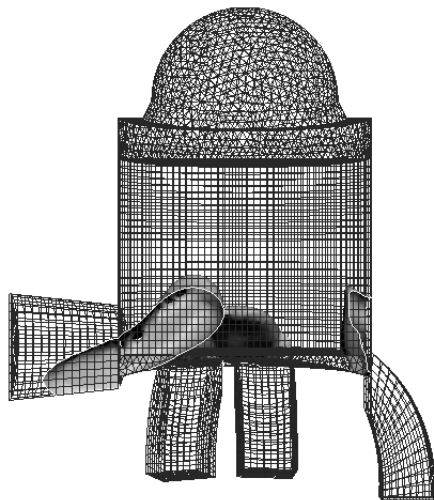


FIGURE 1.1. Multidimensional model of a 150cc two stroke engine showing short circuiting of charge from side intake ports to the exhaust

Chief among the thermodynamic cycle models are the so-called quasidimensional or multi-zone spray codes. Hiroyasu and colleagues [10, 53, 12] describe a diesel combustion model that discretized the fuel spray into a series of packets that, upon entering the combustion chamber, entrained air at a rate governed by momentum conservation and semi-empirical correlations for spray penetration and breakup. Empirical correlations for ignition delay were used to calculate the moment when the premixed fuel and air started burning. Upon calibrating combustion rate constants to experimental data for a specific engine, this approach was able to match the apparent heat release rate in both premixed and diffusion burn phases reasonably well. These models leveraged a variety of works on fuel atomization processes [13–15, 17] and spawned further research into simplified models of sprays in swirling flows [16], droplet Sauter mean diameters [18], and dispersion and wall impingement [20].

Early versions of these packetized fuel spray models assumed that combustion occurred at stoichiometric conditions at small scales, although later extensions by researchers Bazari [21], Rakopoulos [22], and Jung [25] adjusted the burn rate according to local zone equivalence ratios. Rakopoulos modeled the swirling flows in the cylinder to spread the fuel spray and generate two dimensional maps of local equivalence ratio, and later extensions described in [24] added blowby effects and improved combustion rate models. Jung's model offered updated fuel spray penetration correlations for modern injector nozzles with higher discharge coefficients, and showed good agreement with experiment for nitric oxide and soot emissions, indicated mean effective pressure, and heat release rate. The model was integrated into the diesel cycle simulation of [9], and later added considerations for spray over-penetration and estimates of unburned hydrocarbon emissions [26]. More recent efforts also incorporated turbulence effects into the combustion rate [27], as well as improved soot modeling [28]. All of these quasidimensional spray models, however, required calibration of several empirical constants to match heat release rate and pressure data to experiments, and so cannot be used in a truly predictive fashion.

This work describes a new quasidimensional model that uses detailed chemical kinetics to eliminate empirical calibration constants in the combustion modeling. The chemical kinetics place a much greater burden on the phenomenological fluid mechanics models to correctly predict fuel air mixing processes for the determination of local equivalence ratios and temperatures in the sprays. The shortcomings of the spray flow modeling in previous work appears to have been largely absorbed into the empirical burn rate constants to yield proper heat release rates, and so a new parcel mixing model was developed to improve heat release rate predictions with detailed kinetics.

1.3. ALTERNATIVE FUELS

Using detailed chemical kinetics opens the door to evaluating alternative fuel chemistry impacts predictively with a quasidimensional model. With conventional fossil fuels being a finite resource, there is a need for development of alternative liquid fuels that have the potential to reduce net life cycle carbon dioxide emissions into the atmosphere and aid efforts to counteract global warming trends. Diesel engines are fairly adaptable to running on a variety and quality of fuel oils, and thus are prime candidates for fueling with organic biodiesels. A comprehensive review of biodiesel characteristics and engine performance is offered in [63]. Many findings show minimal impact on energy-based fuel economy, lower levels of particulate emissions, but generally higher NO_x when running engines with biodiesel relative to petroleum diesel [64].

Biodiesel is a blend of various methyl ester vegetable oils such as soybean, canola, sunflower, and algae oils, among others. It is produced through the transesterification of the vegetable oil feedstock with a low molecular weight alcohol. In the United States, soy is a common feedstock that, upon processing, results in a blend of five primary methyl esters: methyl palmitate ($\text{C}_{17}\text{H}_{34}\text{O}_2$), methyl stearate ($\text{C}_{19}\text{H}_{38}\text{O}_2$), methyl oleate ($\text{C}_{19}\text{H}_{36}\text{O}_2$), methyl linoleate ($\text{C}_{19}\text{H}_{34}\text{O}_2$), and methyl linolenate ($\text{C}_{19}\text{H}_{32}\text{O}_2$) [73]. Biodiesels are fully miscible with conventional diesel, and can be blended at various levels denoted by the volume percent of biodiesel (i.e. B20, B100).

Both the physical properties and combustion pathways of methyl ester fuels are different from typical petroleum-based diesel fuel. For example, biodiesel has a higher molecular weight, density, viscosity, and surface tension, and lower vapor pressure and heating value. Chakravarthy and colleagues developed relations for typical soy-based biodiesel [65] that were

used by Ra et al. to investigate the impact on diesel combustion solely due to changes in physical properties [66]. In general, biodiesel exhibits longer vaporization times and ignition delays relative to diesel, but no single thermophysical property was primarily responsible for these effects. However, the commonly observed increase in NO_x and lower soot levels when using biodiesel were only partially explained by differences in physical properties, and the chemical kinetic pathways may play a significant role too.

For comprehensive numerical simulation of biodiesel combustion, sophisticated chemical kinetic mechanisms are needed to predict combustion phasing, heat release, and emissions. Detailed chemical kinetic mechanisms to represent biodiesel were first developed for short chain oxygenated fuels such as methyl butanoate and methyl formate [67]. These methyl esters were found to inadequately capture ignition delays [68–70], and further research suggested the importance of modeling longer chain lengths. In addition, accounting for the presence of carbon-carbon double bonds was found to be necessary to adequately predict the combustion process [71]. A detailed biodiesel surrogate mechanism with methyl decanoate and methyl-9-decenoate was developed and validated by Herbinet and colleagues [72] with 3299 species and 10806 reactions. This mechanism was reduced to a size suitable for detailed engine simulations with 71 species and 192 reactions by Brakora [73], and is used in this work. Structures of the two biodiesel surrogate fuel molecules are shown in Fig. 1.2.

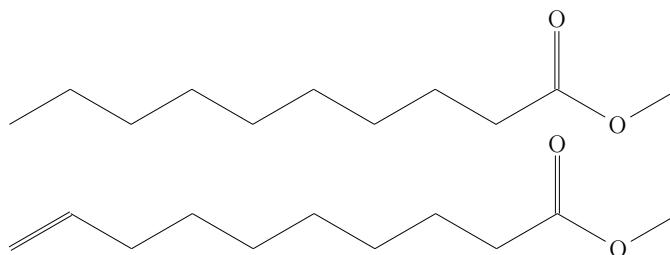


FIGURE 1.2. Biodiesel surrogate fuel molecules methyl decanoate ($\text{C}_{11}\text{H}_{22}\text{O}_2$) and methyl-9-decenoate ($\text{C}_{11}\text{H}_{20}\text{O}_2$).

Efforts towards modeling the impact on engine behavior when using biodiesel range from fairly simple calibrated thermodynamic models to multidimensional models incorporating detailed chemistry. Several works adapted cycle simulations with empirical burn rate constants to experiments with biofuels [83–86]. These simulations required calibration of the model to measured data, and were thus limited in their general predictive capability, particularly when considering the importance of fuel chemistry for understanding biodiesel combustion. Subsequent numerical modeling with computational fluid dynamics (CFD) tools yielded more predictive information about the biodiesel combustion and emissions formation processes [87, 88], and largely agreed with the experimental work of Zhu [89] that there is a slight to notable increase in NO_x with biodiesel, but that moderate exhaust gas recirculation (EGR) may mitigate the increased NO_x formation tendency. In both modeling efforts, however, deficiencies were noted in the soot predictions due to inadequate understanding of soot formation and oxidation processes particularly for biodiesel fuels. Although there appears to be some collective understanding in the literature that fueling with biodiesel tends to slightly increase NO_x while reducing other pollutants [78], both increases [81, 80, 82] and reductions [79, 74] in NO_x have been observed in experimental and numerical research efforts. Two studies considering several engines and biodiesel fuel blends both showed, in general, higher NO_x for biodiesel, even though some data points showed lower NO_x [90, 91]. This apparent ambiguity suggests that the mechanisms for increased NO_x are generally complex and involve many factors whose effects may alternatively compound one another or cancel out, depending on the particulars of fuel properties, chemical kinetics, engine design, and operational parameters.

Several hypotheses put forth in the literature to explain the tendency of biodiesel to exhibit higher NO_x are briefly listed here [76, 77, 92]:

- (1) The combustion process may be advanced for biodiesel relative to diesel due to differences in physical properties (viscosity, density, compressibility) that effectively advance fuel injection timing in the injector,
- (2) Reduced soot formation with biodiesels increases local temperatures due to reduced radiative heat transfer from particulates,
- (3) Higher adiabatic flame temperatures for some biodiesels could promote NO_x formation,
- (4) Higher cetane numbers (shorter ignition delay) may lead to advanced combustion timing, higher temperatures, and more NO_x ,
- (5) Spray droplet breakup behavior of biodiesel fuels may influence how much fuel burns in a premixed or diffusion flame,
- (6) Possible increased activity of the prompt NO_x mechanism with biodiesel due to different chemical kinetic combustion pathways.

On the whole, one may find a considerable number of works in the literature both that alternatively provide evidence for and against each of these biodiesel NO_x increase hypotheses. Collectively taken, there still does not appear to be a consistent explanation or theory for NO_x with regards to biodiesel fuels. Even in the presence of numerous studies showing opposite trends, the most generally applicable observation for the NO_x increase, seems to be the advance of injection start of biodiesel relative to diesel due to the higher density and viscosity of biodiesel [76].

The influence of prompt NO_x in biodiesel combustion is particularly not well understood. Prompt NO_x in engine combustion is usually considered negligible relative to NO_x formation by the thermal or Zeldovich mechanism [7]. Prompt NO_x chemistry occurs in early stages of combustion at rich flame boundaries in which hydrocarbon radicals react with molecular nitrogen, producing intermediates such as hydrogen cyanide (HCN) that then subsequently oxidize to NO_x [75]. The significance of prompt NO_x in biodiesel combustion will need further investigation with fairly detailed chemical kinetic mechanisms for biodiesel to yield credible estimates of the role of prompt NO_x .

1.4. SUMMARY

The several aims of the new model presented in this work include prediction of: 1) heat release rate, cylinder pressure, and emissions without model calibration for several different engines with reasonable accuracy, 2) trends and tradeoffs among engine design and operational parameters such as injector geometry, swirl ratio, and kinetic mechanisms, and 3) impacts of fuel properties and chemical kinetics, all at an order of magnitude lower computational burden than CFD tools.

The core purpose of modeling engine performance is to help designers create engines with lower emissions and higher efficiency. A 20 % improvement in average engine efficiency in the United States, if possible, would roughly eliminate the need for petroleum imports from the Persian Gulf [2], not to mention the sizable positive environmental impact in terms of reduced pollutant and greenhouse gas emissions. With the internal combustion engine likely to remain a mainstay in modern life for many decades to come, the motivation for this work, then, would seem clear.

CHAPTER 2

MODELING APPROACH

2.1. OVERVIEW

The conceptual starting point for a quasidimensional fuel spray model is the thermodynamic zone. Each zone tracks its own mass, temperature, and composition history in time, and all zones are assumed to be at the same uniform cylinder pressure. At the beginning of the simulation, a single zone represents a mixture of combustion residuals and fresh air. This single zone is compressed according to piston motion. Upon start of fuel injection, new zones containing liquid fuel penetrating the cylinder are added at each simulation step. Fig. 2.1 illustrates the conversion processes for each zone, or parcel, from liquid to combustion products. The mass of fuel in each zone remains constant throughout the simulation, and each spray zone entrains air from the surroundings as the spray penetrates the cylinder and slows down.

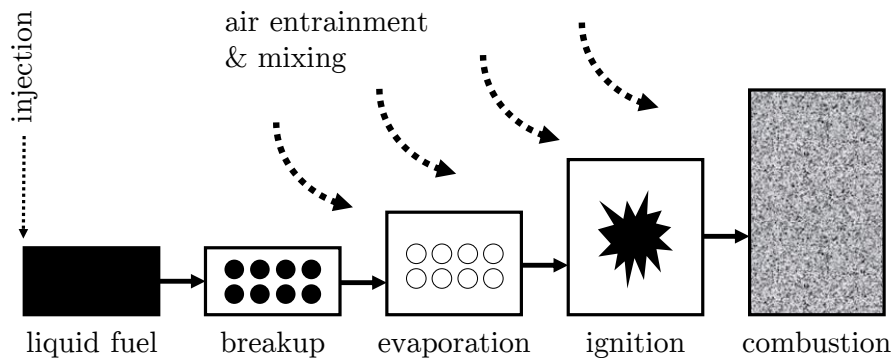


FIGURE 2.1. Transformation of a thermodynamic zone (“parcel”) from liquid fuel to combustion products.

This model only considers the closed portion of the engine combustion cycle. Intake and exhaust strokes are not modeled, and the cylinder conditions at bottom dead center (BDC), including any residuals and exhaust gas recirculation (EGR), are specified as initial conditions.

2.2. THERMODYNAMICS

In this section, equations for the rate of change of temperature and pressure are developed for the gas phase. The liquid fuel phase is considered separately and the vaporizing fuel spray is included as a source term in the gas phase analysis. Continuity is preserved only for the gas phase, under the assumption that the liquid mass in the cylinder is a very small fraction of the total cylinder mass since the fuel will vaporize completely. The differentials in the subsequent analysis may be interpreted as with respect to time or crank angle, which are related to one another by the engine speed N (rpm):

$$(2.1) \quad \frac{d}{d\theta} = \frac{1}{\omega} \frac{d}{dt} \quad \text{where} \quad \omega = \frac{\pi N}{30} \quad \frac{\text{rad}}{\text{s}}$$

The first law of thermodynamics is applied to each zone, which is treated as an open system [7]:

$$(2.2) \quad dU = dQ - PdV + \sum_i dm_i h_i$$

Zones are comprised of a mixture of N species, each of mole fraction y_k . The zone specific internal energy u is given by:

$$(2.3) \quad u = \sum_k^N y_k u_k \quad \text{with} \quad u_k = u_k(T)$$

Differentiating with the chain rule:

$$(2.4) \quad du = \sum_k^N d(y_k u_k) = \sum_k^N \left(y_k \frac{du_k}{dT} dT + u_k dy_k \right)$$

Expanding the left hand side of Eqn. 2.2:

$$(2.5) \quad dU = d(mu) = dm \sum_k^N y_k u_k + m \sum_k^N \left(y_k \frac{du_k}{dT} dT \right) + m \sum_k^N u_k dy_k$$

Recalling the definition of the constant volume specific heat for a mixture of species,

$$(2.6) \quad c_v = \sum_k^N y_k \frac{du_k}{dT}$$

Then, Eqn. 2.5 can be written in a simpler form in which u and c_v represent the mixture internal energy and specific heat:

$$(2.7) \quad dU = u dm + m c_v dT + m \sum_k^N u_k dy_k$$

Next, the ideal gas law $PV = mRT$ is differentiated and applied to a zone:

$$(2.8) \quad PdV = mRdT + mTdR + RTdm - VdP$$

Combining Eqns. 2.2, 2.7, and 2.8:

$$(2.9) \quad u dm + m c_v dT + m \sum_k^N u_k dy_k = dQ - mRdT - mTdR - RTdm + VdP + \sum dm_i h_i$$

Using the specific heat relation for ideal gases $c_p - c_v = R$, and collecting dT terms, yields an equation for the rate of temperature change in each zone:

$$(2.10) \quad dT = \frac{1}{mc_p} \left(dQ - u dm - m \sum_k^N u_k dy_k - mT dR - RT dm + \sum m_i h_i \right) + \frac{RT}{P c_p} dP$$

To solve for the rate of pressure change dP , the ideal gas law is applied again, but to the entire cylinder contents:

$$(2.11) \quad PdV_c + V_c dP = \sum_z m_z R_z dT_z + \sum_z m_z T_z dR_z + \sum R_z T_z dm_z$$

Writing Eqn. 2.10 in the form $dT_z = A_z + B_z dP$ and rearranging terms:

$$(2.12) \quad dP = \frac{-PdV_c + \sum_z (m_z R_z A_z + m_z T_z dR_z + R_z T_z dm_z)}{V_c - \sum_z m_z R_z B_z}$$

where

$$(2.13) \quad A_z = \frac{1}{m_z c_p} \left(dQ_z - u_z dm_z - m_z \sum_k^N u_{z,k} dy_{z,k} - m_z T_z dR_z - R_z T_z dm_z + \sum m_{z,i} h_{z,i} \right)$$

and

$$(2.14) \quad B_z = \frac{R_z T_z}{P c_{p,z}}$$

The rate of gas constant change dR can be written as:

$$(2.15) \quad dR = -\frac{R_u}{M^2} dM = -\frac{R_u}{\left(\sum_k^N y_k M_k \right)^2} \sum_k^N dy_k M_k$$

Finally, the rate of change of species mole fraction dy_k in each zone is calculated by advancing the chemical kinetics of each zone independently at each simulation step. Species internal energies are calculated from the same NASA polynomials for nondimensional enthalpy h/RT that are also used in the chemical kinetics.

2.3. ENGINE GEOMETRY

The cylinder volume and rate of volume change is determined by the geometry and is a function of crank angle θ [5]. A schematic is shown in Fig. 2.2. Here, r_c is the compression ratio, B is the cylinder bore, S is the stroke, and R is the ratio of connecting rod length l to crank radius a .

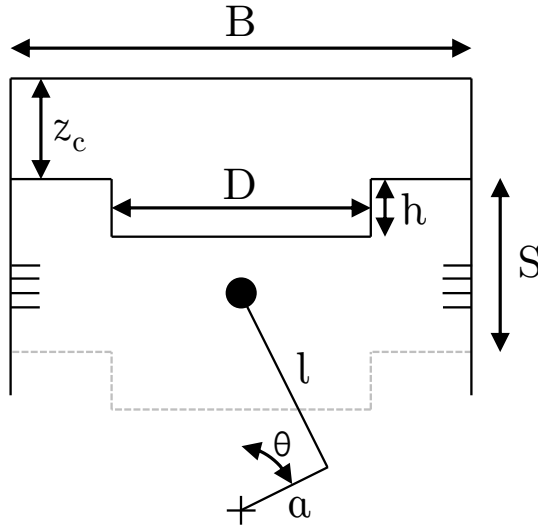


FIGURE 2.2. Cylinder geometry parameters.

The cylinder volume is:

$$(2.16) \quad V = V_0 \left(1 + \frac{1}{2} (r_c - 1) \left(R + 1 - \cos \theta - \sqrt{R^2 - \sin^2 \theta} \right) \right)$$

where V_0 is the cylinder volume at top dead center (TDC) given by:

$$(2.17) \quad V_0 = \frac{\pi}{4} B^2 S \cdot \frac{1}{r_c - 1}$$

Differentiating Eqn. 2.16 gives rate of volume change:

$$(2.18) \quad dV = V_0 \cdot \frac{r_c - 1}{2} \left(\sin \theta + \frac{\cos \theta \sin \theta}{\sqrt{R^2 - \sin^2 \theta}} \right)$$

The cycle mean piston speed is given by:

$$(2.19) \quad \bar{U}_p = 2NS$$

The instantaneous piston speed is [7]:

$$(2.20) \quad U_p = \bar{U}_p \cdot \frac{\pi}{2} \sin \theta \left(1 + \frac{\epsilon \cos \theta}{\sqrt{1 - \epsilon^2 \sin^2 \theta}} \right);$$

where ϵ is the ratio of crank radius to connecting rod length and is equivalent to $1/R$.

2.4. CHEMICAL KINETICS

The chemical kinetics solver used in this model is a C++ implementation of the CHEMKIN-II [41] methodology, and uses standard CHEMKIN-II formatted reaction and thermodynamic property database input files. The species concentrations in each zone are evolved in time from an initial pressure, temperature, and composition using a constant volume perfectly stirred reactor model. Each i -th elementary reaction can be written in the form



where ν_{ki} are stoichiometric coefficients and the χ_k represent the species. The production rate $d\omega_k/dt$, in moles/cm³/sec, for the k -th species is:

$$(2.22) \quad \frac{d\omega_k}{dt} = \sum_i (\nu''_{ki} - \nu'_{ki}) q_i$$

The net rate of progress for the i -th reaction q_i incorporates the species concentrations $[X_k]$ and the forward (k_{fi}) and reverse (k_{ri}) rates for that reaction:

$$(2.23) \quad q_i = k_{fi} \prod_k [X_k]^{\nu'_{ki}} - k_{ri} \prod_k [X_k]^{\nu''_{ki}}$$

The forward rates of most elementary reactions are assumed to have an Arrhenius temperature dependence, from which the corresponding reverse reaction rate can be obtained from the species equilibrium constant.

More complex reaction rates involving species-enhanced third-body reactions, or pressure-dependent falloffs of the Lindemann, 3-parameter Troe, or 4-parameter Troe forms are all supported, though the reader is referred to the Chemkin documentation for the specifics [41].

The C++ implementation of the CHEMKIN methodology was extensively compared against the Cantera software package [42] to validate the model across a wide range of temperatures, pressures, equivalence ratios, and fuel compositions. A small subset of the results is shown in Figs. 2.3-2.4. Excellent agreement is evident in all cases.

For the engine simulations in this paper, the reduced primary reference fuel (PRF) kinetic mechanism of Ra and Reitz [66] is used. The mechanism has 41 species and 130 reactions, and has been used extensively in CFD simulations of reacting fuel sprays. The coupling of the chemical kinetics with the zone gas phase energy and continuity equations is outlined later in §2.15.

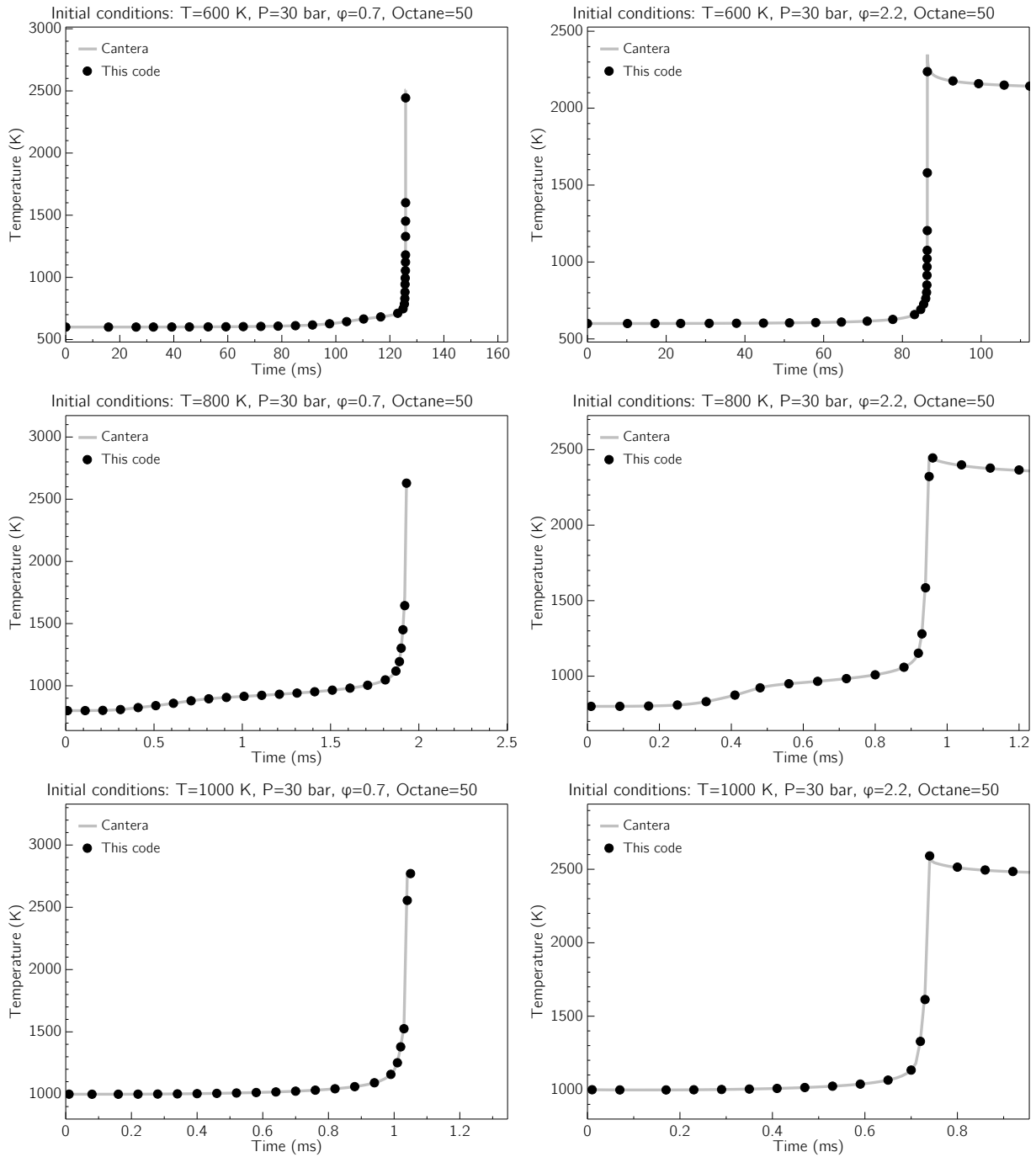


FIGURE 2.3. Selected ignition delay comparisons between the new C++ chemistry solver versus Cantera at medium-low pressure (30 bar).

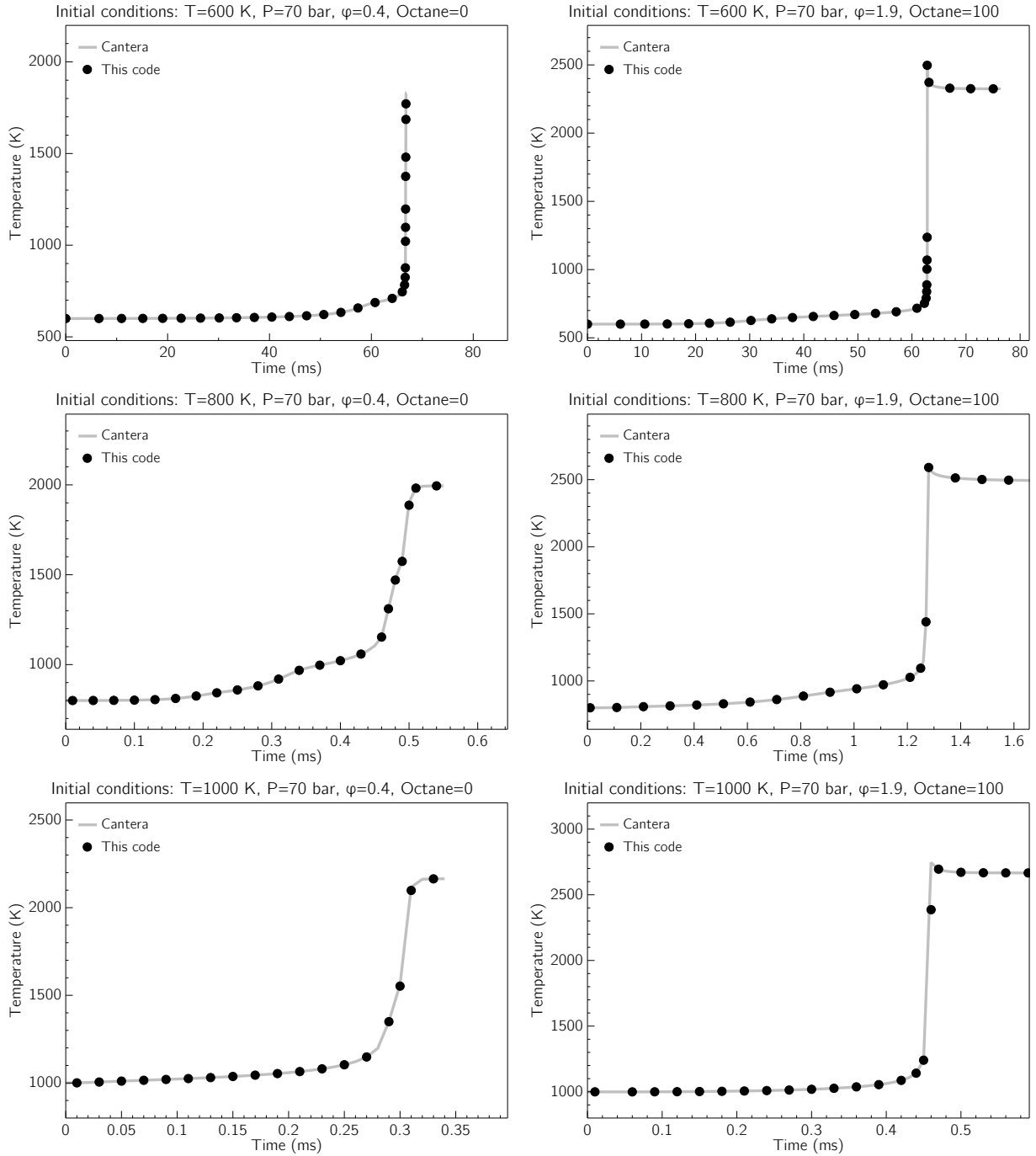


FIGURE 2.4. Selected ignition delay comparisons between the new C++ chemistry solver versus Cantera at medium high pressure (70 bar).

For the biodiesel investigations, chemical kinetics are modeled using the reduced multi-chemistry mechanism of Brakora [73]. The mechanism consists of 71 species and 192 reactions, and uses a blend of n-heptane, methyl decanoate, and methyl-9-decenoate as surrogates to represent the chemical kinetic behavior of a generic soy-based biodiesel. Comparisons with experimental data for a 100 % (B100) soy-based biodiesel and the full mechanism of [72] suggested that a blend of 50 % n-heptane, 25 % methyl decanoate, and 25 % methyl-9-decenoate best captured ignition behavior over a wide range of temperatures and pressures [73, 74]. Absent alternate annotations, results labeled as “biodiesel” in subsequent chapters use this blend of surrogate species for biodiesel combustion.

2.5. GAS JETS APPLIED TO DIESEL SPRAYS

The overall behavior of a dense evaporating diesel fuel spray can be quite satisfactorily modeled as a turbulent gaseous jet [31–35]. Applying the approach of [36] and accounting for differences between the densities of the injected and ambient gases [29], good predictions of spray tip penetration and centerline velocity were possible [37, 38]. In this section, a general analytical derivation is presented for a gas jet, and it is shown how the empirical relations and constants for spray tip penetration frequently used in quasidimensional modeling of diesel engines such as in [25] can be readily recovered. The approach presented here largely follows the forthcoming analysis in [39].

Fig. 2.5 shows the conceptual structure used as the starting point for the analysis. Defining the half angle $\theta/2$ at the position in the spray where the velocity u is half the centerline velocity u_x :

$$(2.24) \quad \tan\left(\frac{\theta}{2}\right) = \frac{R}{x} \quad \text{where} \quad \frac{u}{u_x} = 0.5$$

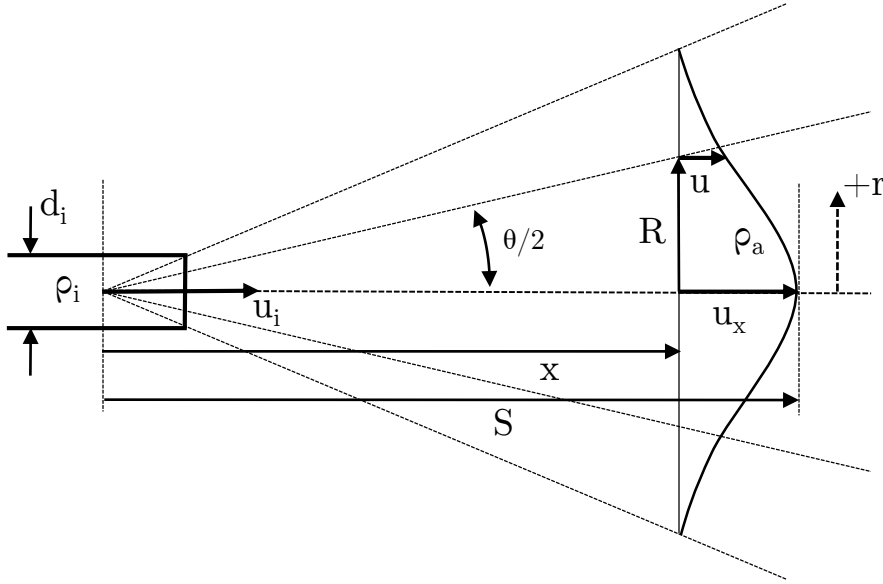


FIGURE 2.5. Diagram of gas jet parameters.

Assuming an exponential velocity profile in the radial direction, the velocity at any position in the spray can be written in an axial or radial form:

$$(2.25) \quad \frac{u}{u_x} = \exp \left[-C \left(\frac{r}{x} \right)^2 \right] \quad \text{'axial'}$$

$$(2.26) \quad = \exp \left[-\alpha \left(\frac{r}{R} \right)^2 \right] \quad \text{'radial'}$$

At a given r ,

$$(2.27) \quad \frac{C}{x^2} = \frac{\alpha}{R^2} \quad \longrightarrow \quad C = \alpha \left(\frac{x}{R} \right)^2 = \frac{\alpha}{\tan^2(\theta/2)}$$

Assuming a spray edge ($r = R$) defined by half the centerline velocity yields an equation for α :

$$(2.28) \quad \frac{u}{u_x} = 0.5 \quad \longrightarrow \quad 0.5 = \exp[-\alpha \cdot 1^2] \quad \longrightarrow \quad \alpha = \ln 2$$

Substituting back into Eqn. 2.26:

$$(2.29) \quad \frac{u}{u_x} = \exp\left[-\ln 2 \left(\frac{r}{R}\right)^2\right]$$

The jet centerline velocity decay is:

$$(2.30) \quad \frac{u_x}{u_i} = K \left(\frac{\rho_i}{\rho_a}\right)^{1/2} \frac{d_i}{x - x_p} \approx K \left(\frac{\rho_i}{\rho_a}\right)^{1/2} \frac{d_i}{x}$$

Solving for the decay constant K :

$$(2.31) \quad K = \left(\frac{\rho_a}{\rho_i}\right)^{1/2} \frac{u_x \cdot x}{u_i \cdot d_i}$$

A relation between the decay constant and half angle can be derived by assuming a constant jet momentum \dot{M} and assuming a ‘top hat’ velocity profile at the nozzle of u_i :

$$\begin{aligned} \dot{M} &= \rho_i \frac{\pi}{4} d_i^2 u_i^2 = \int_0^\infty \rho_a 2\pi r u^2(r) dr \\ &= 2\pi \rho_a u_x^2 \int_0^\infty \exp\left[-2 \ln 2 \left(\frac{r}{R}\right)^2\right] dr \\ &= 2\pi \rho_a u_x^2 \frac{R^2}{2 \ln 2} \cdot \int_0^\infty x \exp[-x^2] dx \\ &= 2\pi \rho_a u_x^2 \frac{R^2}{2 \ln 2} \cdot \frac{1}{2} \end{aligned}$$

Collecting and rearranging terms:

$$(2.32) \quad \rho_i \frac{\pi}{4} d_i^2 u_i^2 = 2\pi \rho_a u_x^2 \frac{R^2}{2 \ln 2} \cdot \frac{1}{2}$$

$$(2.33) \quad \frac{u_x^2 R^2}{u_i^2 d_i^2} = \left(\frac{\rho_i}{\rho_a} \right) \frac{\ln 2}{2}$$

$$(2.34) \quad \frac{u_x R}{u_i d_i} = \left(\frac{\rho_i}{\rho_a} \right)^{1/2} \left(\frac{\ln 2}{2} \right)^{1/2}$$

Incorporating this result into Eqn. 2.31 with the help of Eqn. 2.24:

$$(2.35) \quad K = \left(\frac{\rho_a}{\rho_i} \right)^{1/2} \frac{u_x \cdot x}{u_i \cdot d_i} = \left(\frac{\rho_a}{\rho_i} \right)^{1/2} \frac{u_x \cdot R}{u_i \cdot d_i} \cdot \frac{1}{\tan \theta/2} = \left(\frac{\ln 2}{2} \right)^{1/2} \cdot \frac{1}{\tan \theta/2}$$

From experiments, $K \approx 5.9$. Then, the spray half angle is:

$$(2.36) \quad \tan \theta/2 = \frac{(0.5 \ln 2)^{1/2}}{5.9} = 0.0998 \quad \longrightarrow \quad \frac{\theta}{2} = 5.7^\circ$$

A commonly used semi-empirical expression for diesel spray angle is [25]:

$$(2.37) \quad \tan \frac{\theta}{2} = \frac{1}{A} 4\pi \left(\frac{\rho_a}{\rho_i} \right)^{1/2} \frac{\sqrt{3}}{6} \quad \text{and} \quad A = 3.0 + 0.28 \frac{l_i}{d_i}$$

Assuming a ρ_a/ρ_i density ratio of 25×10^{-3} and a nozzle length to diameter ratio l_i/d_i of 6 gives a similar spray half angle of 6.9° . However, the empirical relation represents the angle of the full spray envelope, and is likely more representative of an edge defined by $u/u_m \approx 0.01$, thus the slightly larger half angle, compared to the gas jet analysis with $K = 5.9$.

The jet tip penetration $S(t)$ can be found by integrating the velocity decay equation. Since there is entrainment and mixing occurring, $u_x(S) \neq dS/dt$, but they can be related

with an entrainment constant K_u following the approach of [37]:

$$(2.38) \quad u_x(x = s) = K_u \frac{dS}{dt}$$

This assumes that the front of the injection plume will move at an effective “group velocity” that is different from the individual parcel velocity within the spray. Applying a constant momentum approach to an individual parcel with a constant fuel mass m_f , at any instant along the centerline at $x = S$, where m_a is the mass of entrained air into the parcel, gives:

$$(2.39) \quad m_f u_i = (m_f + m_a) u_x = (m_f + m_a) K_u \frac{dS}{dt}$$

Rearranging terms:

$$(2.40) \quad m_f \left(u_i - K_u \frac{dS}{dt} \right) = m_a K_u \frac{dS}{dt}$$

$$(2.41) \quad m_a = m_f \left(\frac{u_i}{K_u} \left(\frac{dS}{dt} \right)^{-1} - 1 \right)$$

Differentiating with respect to time gives an equation for the rate of air entrainment into the parcel:

$$(2.42) \quad \frac{dm_a}{dt} = -m_f u_i \frac{1}{K_u} \left(\frac{dS}{dt} \right)^{-2} \frac{d^2 S}{dt^2}$$

Although by default $K_u = 1$ in this work, [37] makes an argument for a value of $K_u \approx 2$.

Returning to the jet tip location $S(t)$:

$$(2.43) \quad \frac{u_x}{u_i} = K \left(\frac{\rho_i}{\rho_a} \right)^{1/2} \frac{d_i}{x} \quad \text{and} \quad u_x = K_u \frac{dS}{dt}$$

Letting $x \rightarrow S$, then:

$$(2.44) \quad \frac{dS}{dt} = u_i \left(\frac{\rho_i}{\rho_a} \right)^{1/2} \cdot \frac{K}{K_u} \cdot \frac{d_i}{S}$$

Separating variables and integrating:

$$(2.45) \quad \begin{aligned} SdS &= \left[u_i \left(\frac{\rho_i}{\rho_a} \right)^{1/2} \cdot \frac{K}{K_u} d_i \right] dt \\ \frac{1}{2} S^2 &= \left[u_i \left(\frac{\rho_i}{\rho_a} \right)^{1/2} \cdot \frac{K}{K_u} d_i \right] t \\ S &= \left[2u_i \left(\frac{\rho_i}{\rho_a} \right)^{1/2} \cdot \frac{K}{K_u} d_i \right]^{1/2} t^{1/2} \end{aligned}$$

The injection velocity can be calculated by applying Bernoulli's equation to the nozzle pressure difference:

$$(2.46) \quad u_i = C_d \left(\frac{2\Delta P}{\rho_i} \right)^{1/2}$$

Incorporating into Eqn. 2.45, the penetration $S(t)$ is:

$$(2.47) \quad S = \left[2\sqrt{2}C_d \cdot \frac{K}{K_u} \left(\frac{\rho_i}{\rho_a} \right)^{1/2} \right]^{1/2} \left(\frac{\Delta P}{\rho_i} \right)^{1/4} (d_i t)^{1/2}$$

$$(2.48) \quad = \left[2\sqrt{2}C_d \cdot \frac{K}{K_u} \right]^{1/2} \left(\frac{\Delta P}{\rho_a} \right)^{1/4} (d_i t)^{1/2}$$

If $C_d = 0.6$, $K = 5.9$, $K_u = 1.2$, then the leading coefficient is:

$$(2.49) \quad \left[2\sqrt{2}C_d \cdot \frac{K}{K_u} \right]^{1/2} = 2.9$$

which is very close to the experimentally observed leading constant of 2.95 in the spray penetration equation of the same mathematical form in [25] that is used in the quasidimensional model described in the following sections. The effects of varying the entrainment constant K_u on heat release rate and various metrics are explored in §5.3. Overall, the analysis presented in this section suggests that using a one dimensional momentum conservation model of a gas jet for predicting diesel spray entrainment and penetration is quite reasonable, and that the jet centerline velocity decay constant K is a key parameter for describing many aspects of spray behavior.

2.6. SPRAY MODELING

The spray parcel concept is sketched in Fig. 2.6. At the beginning of each simulation step, a new set of radial zones is created during the fuel injection period.

Liquid fuel is injected into the cylinder with a total mass flow rate and velocity given by:

$$(2.50) \quad \frac{dm_f}{dt} = C_d A_n \sqrt{2\rho_f(P_{inj} - P)} \quad \text{and} \quad u_i = C_d \sqrt{\frac{2(P_{inj} - P)}{\rho_f}}$$

The total fuel mass injected into each new radial zone over the simulation step is given by:

$$(2.51) \quad m_{fi} = N_H f_A \frac{dm_f}{dt} \Delta t_{step}$$

where N_H is the number of injector holes and Δt_{step} is the simulation time step. Since the zones emerge from consecutive concentric circular areas of the nozzle cross section, f_A

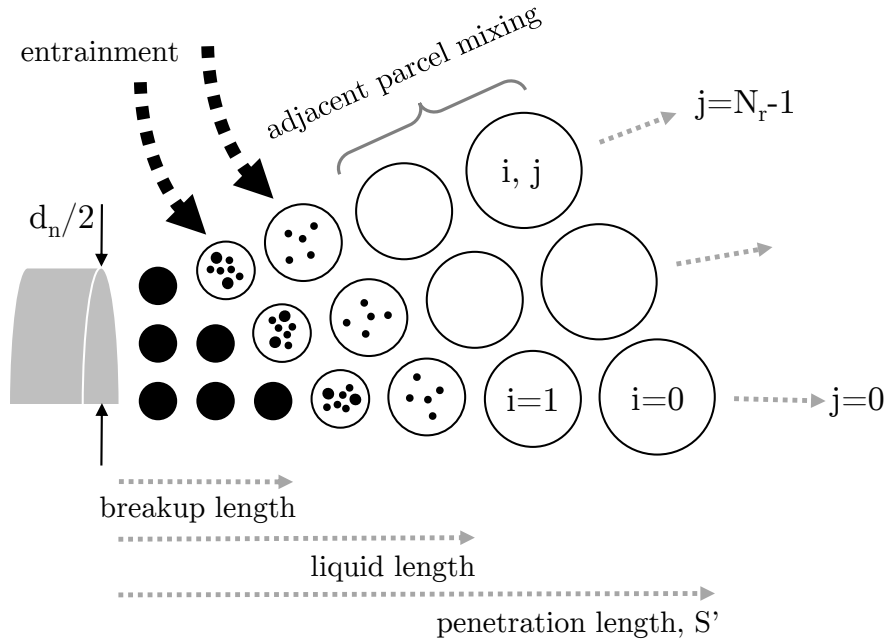


FIGURE 2.6. Spray parcel concept

represents the area fraction corresponding to each radial zone:

$$(2.52) \quad f_A = \frac{(j+1)^2 - j^2}{N_r^2}$$

where j is the zero-based radial zone index and N_r is the number of radial zones in the model. The liquid fuel temperature upon injection is a model input, with a default value of 370 K.

The time from liquid parcel injection to breakup for the centerline parcel is given by the correlation of Jung [25], in seconds:

$$(2.53) \quad t_{brk,center} = 4.351 \frac{\rho_f d_n}{C_d^2 \sqrt{\rho(P_{inj} - P)}}$$

Spray parcels towards the edge of the spray are assumed to break up sooner due to the greater shear forces with the surrounding air. According to observations by Dec [8], liquid

jet breakup at the edge occurs at roughly 1/3 of the liquid core length. Consequently, the breakup time for a parcel at radial position j is given by:

$$(2.54) \quad t_{brk} = t_{brk,center} \left(1 - \frac{2}{3} \frac{j}{N_r - 1} \right)$$

Prior to breakup, the parcels penetrate at their initial injection velocity according to Eqn. 2.50. After breakup, the spray penetration length is given by Jung's correlation, which is suitable for high discharge coefficient injectors [25],

$$(2.55) \quad S = 2.95 \cdot \exp(-Cf^2) \sqrt{d_n} \left(\frac{P_{inj} - P}{\rho} \right)^{0.25} t^\beta$$

Similar to the gas jet analysis in §2.5, Eqn. 2.55 assumes an exponential velocity distribution in the radial direction [6]. The radial position of each parcel in the spray is given by $f = j/N_r$, and the constant C is determined from an appropriate edge velocity fraction E_f when $f = 1$,

$$(2.56) \quad C = -\ln(E_f)$$

Hiroyasu used a value of $E_f \approx 0.42$ [53], but in this work, E_f is set to 0.3 based on better agreement with experiment for diffusion burn heat release rate shapes. Spray velocity profiles for various E_f values are shown in Fig. 2.7.

Prior to wall impingement, the parcels penetrate according to the square root of time ($\beta=0.5$). After colliding with the cylinder wall, piston crown, or piston bowl surface, the effective penetration is reduced and according to measurements by Hiroyasu [19], the spray length proceeds roughly with a β of 0.75. Therefore, the spray velocity goes with $t^{-0.25}$.

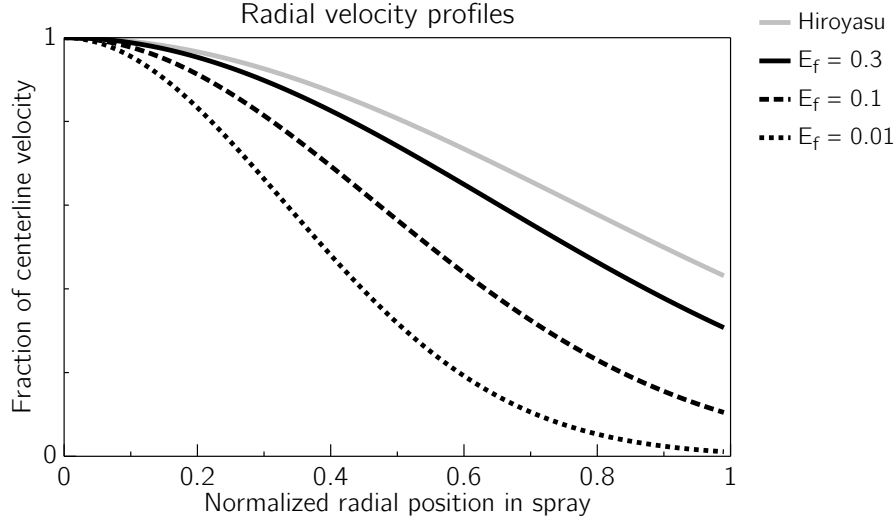


FIGURE 2.7. Normalized radial spray velocity profiles.

As the spray parcels penetrate the combustion chamber, they slow down due to exchange of momentum with the surrounding air. The rate of air entrainment is calculated by applying conservation of momentum to each zone. As discussed in §2.5, an entrainment constant K_u is included to account for differences between local parcel velocity and spray tip velocity. Recalling that the fuel mass m_f in each zone remains constant after injection,

$$(2.57) \quad m_f u_i = (m_f + m_a) K_u \frac{dS'}{dt}$$

where S' is the modified penetration length according to radial position in the spray and large scale flow effects described in §2.7. Rearranging terms and differentiating with respect to time:

$$(2.58) \quad \frac{dm_a}{dt} = -\frac{m_f u_i}{K_u} \left(\frac{dS'}{dt} \right)^{-2} \frac{d^2 S'}{dt^2}$$

2.7. LARGE SCALE FLUID MOTION

Rapid fuel-air mixing is frequently achieved in diesel engines by introducing a swirling flow inside the cylinder. In the presence of swirl, the effective spray penetration is reduced due to the spreading effect on the spray. Arai and colleagues proposed Eqn. 2.59 to adjust the spray penetration length in swirling flows [16]:

$$(2.59) \quad S' = \frac{S}{1 + 2\pi N R_S / 60 \times S / u_i}$$

where R_S is the instantaneous swirl ratio inside the cylinder. With some effort, Eqn. 2.59 can be differentiated with respect to S to obtain the spray velocity and acceleration in the presence of swirl. Fig. 2.8 shows nondimensional spray tip penetration length for different swirl ratios. Under high swirl, the effective spray tip distance is greatly shortened, resulting in more rapid deceleration of the liquid jet and higher initial rate of air entrainment into the spray plume.

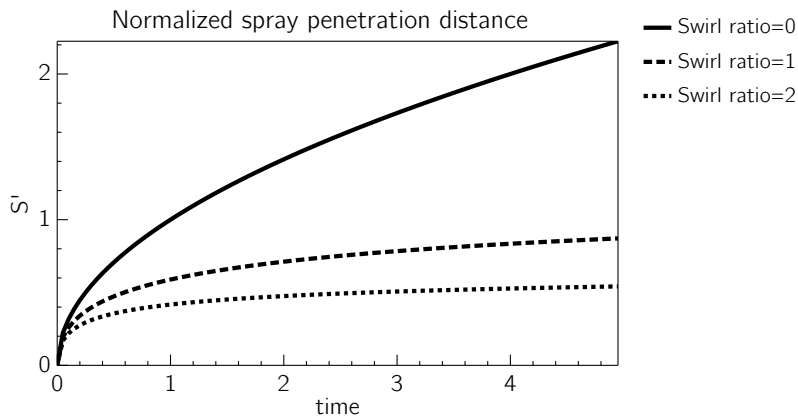


FIGURE 2.8. Influence of swirl ratio on spray tip penetration length.

Swirling flows are introduced by intake manifold and valve geometry that produce flow patterns that may be approximated by a solid-body rotation model of the gaseous cylinder

contents [40]. From conservation of angular momentum through the cycle, the instantaneous swirl ratio can be estimated at any crank angle. Given a user-specified swirl ratio at bottom dead center $R_{S,0}$, the initial cylinder angular momentum Γ and angular velocity ω_s are:

$$(2.60) \quad \Gamma = I\omega_s \quad \text{where} \quad \omega_s = \frac{2\pi R_{S,0}N}{60}$$

The moment of inertia of the cylinder contents at any time is:

$$(2.61) \quad I = \frac{1}{2}\pi\rho \left(z_c \left(\frac{B}{2} \right)^4 + h \left(\frac{D}{2} \right)^4 \right)$$

where B is the cylinder bore, D is the piston bowl diameter, z_c is the piston crown to cylinder head distance, and h is the piston bowl depth.

The initial angular momentum decays through the compression and expansion processes due to frictional shear forces at gas-solid interfaces at the cylinder wall, piston bowl, and piston crown:

$$(2.62) \quad \frac{d\Gamma}{dt} = -(T_c + T_b + T_p)$$

The three torques are [23]:

$$(2.63) \quad T_c = \tau_c \pi B z_c \frac{B}{2} \quad \text{and} \quad \tau_c = \frac{f_c \rho}{2} \left(\frac{\omega_s B}{2} \right)^2$$

$$(2.64) \quad T_b = \tau_b \pi D h \frac{D}{2} \quad \text{and} \quad \tau_b = \frac{f_b \rho}{2} \left(\frac{\omega_s D}{2} \right)^2$$

$$(2.65) \quad T_p = \tau_p \frac{\pi B^3}{2 \cdot 4} \quad \text{and} \quad \tau_p = \frac{f_p \rho}{2} \left(\frac{\omega_s B}{4} \right)^2$$

Note that Eqn. 2.65 is an approximation to the correct value that would result from integrating the frictional loss over the piston radius. For expediency, the mean cylinder radius $B/4$ is chosen as a representative approximation. The friction factors are calculated as if for a flat plate:

$$(2.66) \quad f = 0.058 \text{Re}^{-0.2} \quad \text{where} \quad \text{Re} = \frac{\rho(\omega_s R)R}{\mu}$$

The characteristic length scale R in the Reynolds number is chosen to be the cylinder and piston bowl radii for f_c and f_b , respectively, and half the cylinder radius for f_p . The viscosity is approximated by that of air as a function of temperature [48]. At each simulation step, Eqn. 2.62 is advanced in time to provide a value for Γ from which the instantaneous swirl ratio R_S may be recovered using Eqn. 2.60. This relatively basic analysis correctly predicts that a deep bowl piston (large h and small D) results in a large amplification of swirl during compression, reduces spray penetration, and increases the rate of air entrainment into the spray and thus yields more rapid fuel-air mixing. Fig. 2.9 shows the instantaneous swirl ratio for two different piston bowl shapes, and confirms that a narrow and deep bowl results in more intense rotational motion in the cylinder.

As the piston approaches TDC, the fluid between the piston crown and cylinder head is squished into the bowl as a concentric jet. The squish velocity is calculated with an equation from [5]:

$$(2.67) \quad V_{sq} = \frac{U_p D}{4z_c} \left(\left(\frac{B}{D} \right)^2 - 1 \right) \frac{V_b}{A_c z_c + V_b}$$

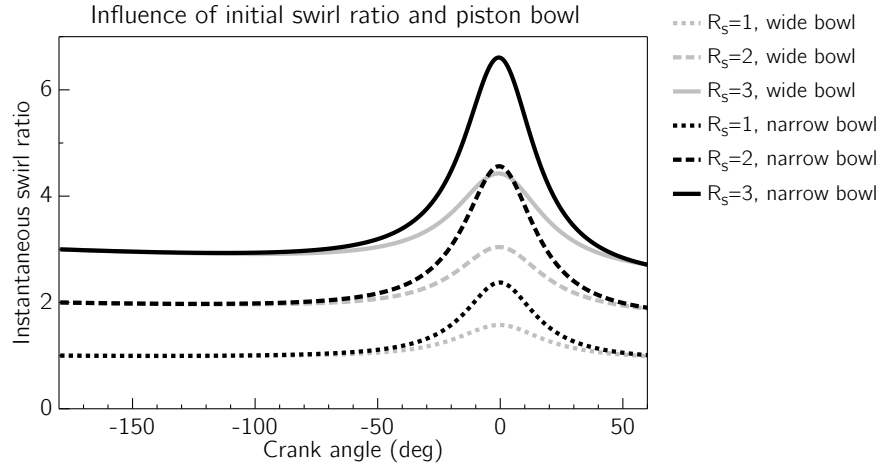


FIGURE 2.9. Instantaneous swirl ratio as a function of piston geometry.

where U_p is the instantaneous piston speed (see §2.3), A_c is the cylinder head area, and V_b is the piston bowl volume. In this model, the squish velocity contributes to the cylinder-averaged mean flow kinetic energy in the turbulence model, to be discussed in §2.9. Fig. 2.10 shows representative model behavior for three different squish area fractions. Large squish area fractions, which correspond to a narrow and deep piston bowl, create greater squish velocity and increased turbulence intensity (u_t , m/s) in the cylinder.

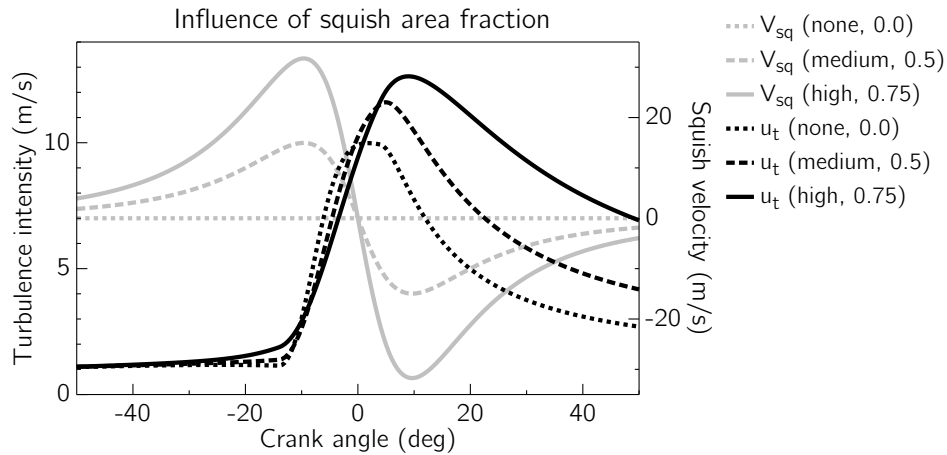


FIGURE 2.10. Turbulence intensity and squish velocity as a function of piston geometry.

2.8. ATOMIZATION AND EVAPORATION

Upon spray breakup, the liquid fuel atomizes into small droplets characterized by the droplet Sauter mean diameter. The Sauter mean diameter is the ratio of the total volume of the droplets to the total surface area, and is commonly denoted as d_{32} . A two equation model developed by Hiroyasu and colleagues accounts for observed differences in breakup mechanisms at different injection velocities [18]:

$$\begin{aligned}
 d_{32} &= d_n \max(d_{32}^L, d_{32}^H) \\
 d_{32}^L &= 4.12 \text{Re}^{0.12} \text{We}^{-0.75} \left(\frac{\mu_l}{\mu}\right)^{0.54} \left(\frac{\rho_l}{\rho}\right)^{0.18} \\
 d_{32}^H &= 0.38 \text{Re}^{0.25} \text{We}^{-0.32} \left(\frac{\mu_l}{\mu}\right)^{0.37} \left(\frac{\rho_l}{\rho}\right)^{-0.47} \\
 \text{Re} &= \frac{\rho_l u_i d_n}{\mu_l} \quad \text{and} \quad \text{We} = \frac{u_i^2 d_n \rho_l}{\sigma}
 \end{aligned}
 \tag{2.68}$$

Given a characteristic droplet Sauter mean diameter, the total liquid fuel mass is distributed among N_g droplet size bins according to a χ^2 distribution that was found to be appropriate for diesel injectors [51]. The cumulative volume distribution is:

$$V = 1 - \exp\left(-\frac{d}{\bar{d}}\right) \left(1 + \frac{d}{\bar{d}} + \frac{1}{2} \left(\frac{d}{\bar{d}}\right)^2 + \frac{1}{6} \left(\frac{d}{\bar{d}}\right)^3\right)
 \tag{2.69}$$

where $\bar{d} = d_{32}/3$. The volume distribution function, dV/dd , is shown in Fig. 2.11 for two Sauter mean diameters.

The smallest and largest droplet diameters considered in the model correspond to χ^2 volume fractions of 0.1 and 0.9, respectively. The diameter range is evenly divided among the N_g bins, and the mass fraction in each bin is readily determined from the volume fraction.

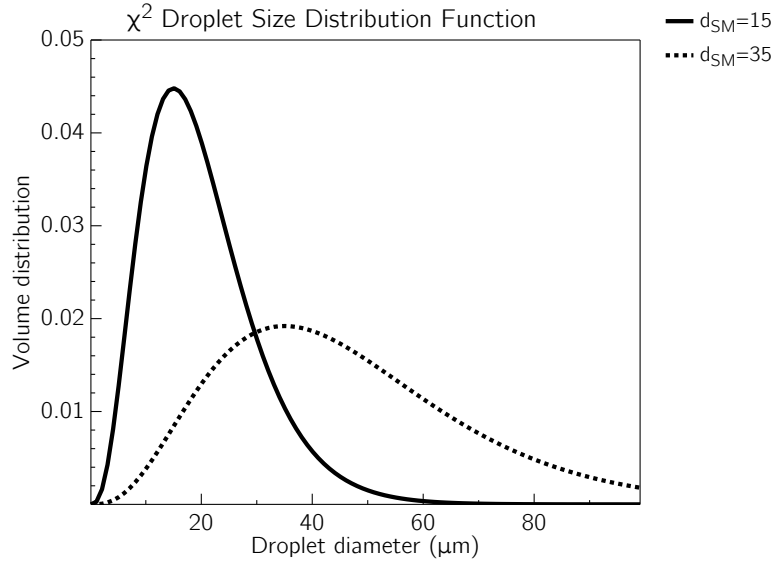


FIGURE 2.11. χ^2 volume distribution function for droplets.

Finally, the relation between the number of droplets N of a certain mass and diameter is:

$$(2.70) \quad N = \frac{6m}{\pi d^3 \rho_f}$$

The effect of modeling multiple droplet sizes can be observed in Fig. 2.12. In the case of two droplets, evaporation beings more quickly due to the presence of small droplets that heat rapidly, and subsequently slows down as the larger droplets take much longer to heat up. With three droplet size bins, the initial vaporization rate is relatively unchanged compared with two bins. It should be noted that the results shown in Fig. 2.12 are primarily representative of relatively low pressure injectors with large nozzles that produce larger droplets. With high pressure modern injectors whose atomization performance is superior, modeling multiple droplet sizes for correctly predicting initial vaporization rates is less important.

Once the initial droplet sizes, numbers, and masses in each spray zone are determined at breakup, the liquid fuel temperature and vaporized fuel mass are advanced forward in time

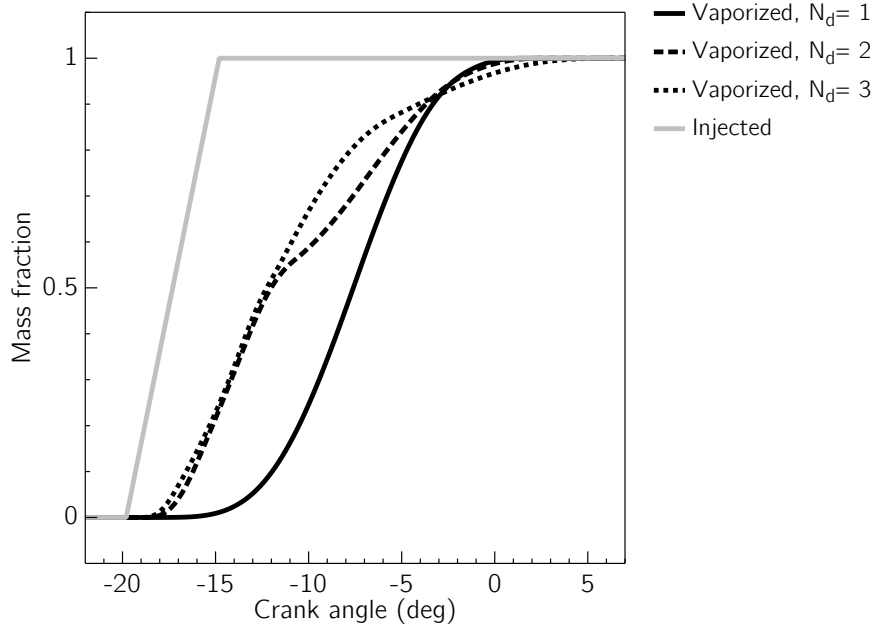


FIGURE 2.12. Effect of multiple droplet sizes on the fuel evaporation process.

using an analysis for a single droplet evaporating in an infinite gaseous medium [52]. The rate of fuel mass vaporization is:

$$(2.71) \quad \frac{dm_{fv}}{dt} = \pi d N \mathcal{D}_{ab} \text{Sh} \frac{P}{R_m T_m} \log(1 + B)$$

The Spalding transfer number B is:

$$(2.72) \quad B = \frac{x_f - x_{f,\infty}}{1 - x_f}$$

where the vapor fuel mass fraction far from the droplet $x_{f,\infty}$ is assumed to be zero, and the vapor mass fraction at the droplet surface is given by:

$$(2.73) \quad x_f = \left[1 + \frac{M_a}{M_v} \left(\frac{P}{P_{v,sat} - 1} \right) \right]^{-1}$$

where M_a and M_v are the molecular weights of air and fuel vapor, respectively. The saturation vapor pressure $P_{v,sat}$ is estimated with Antoine's equation:

$$(2.74) \quad \log_{10}(P_{v,sat}) = a - \frac{b}{T_l - c}$$

where a , b , and c are constants specific to the liquid fuel [7]. The convective heat transfer to the droplets from the surrounding air is:

$$(2.75) \quad q = \pi d N k_m (T - T_l) \text{Nu} \frac{z}{\exp(z) - 1}$$

where z is a parameter to account for boundary layer thickening around the droplet. It is given in [6] as:

$$(2.76) \quad z = \frac{c_{P,v}}{\pi d N k_m \text{Nu}} \cdot \frac{dm_{fv}}{dt}$$

The Sherwood and Nusselt numbers for heat and mass transfer in Eqns. 2.71 and 2.75 are provided by the correlations of Ranz and Marshall [13]:

$$(2.77) \quad \begin{aligned} \text{Nu} &= 2 + 0.6\text{Re}^{0.5}\text{Pr}^{0.33} \\ \text{Sh} &= 2 + 0.6\text{Re}^{0.5}\text{Sc}^{0.33} \end{aligned}$$

The Reynolds, Schmidt, and Prandtl numbers in Eqn. 2.78 are estimated at a mean temperature T_m using the typical "1/3 rule" between the droplet liquid temperature T_l and the ambient gas temperature T [52].

$$\begin{aligned}
(2.78) \quad \text{Re} &= \frac{\rho_m V_{rel} d}{\mu_m} \\
\text{Sc} &= \frac{\mu_m}{\rho_m \mathcal{D}_{ab}} \\
\text{Pr} &= \frac{c_{p,m} \mu_m}{k_m}
\end{aligned}$$

Mean properties for fuel vapor and air are given by correlations and are also estimated using a “1/3 rule,” but according to surface fuel mass fraction rather than temperature, as listed in Eqn. 2.79.

$$\begin{aligned}
(2.79) \quad M_m &= (1 - f)M_a + fM_v \\
\mu_m &= (1 - f)\mu_a + f\mu_v \\
c_{P,m} &= (1 - f)c_{P,a} + fc_{P,v} \\
k_m &= (1 - f)k_a + fk_v \\
\rho_m &= \frac{PM_m}{R_u T_m}
\end{aligned}$$

where f represents the “1/3 rule”:

$$(2.80) \quad f = x_f + \frac{x_{f,\infty} - x_f}{3}$$

The rate of droplet liquid temperature change is:

$$(2.81) \quad \frac{dT_l}{dt} = \frac{1}{m_l c_{P,l}} \left(q - h_{fg} \frac{dm_{fv}}{dt} \right)$$

where h_{fg} is the fuel vapor latent heat, estimated at the liquid fuel temperature. If the droplet temperature exceeds the critical temperature of the liquid fuel, the remaining liquid droplet mass of is directly transferred to the gas phase [55]. Each droplet size group tracks its own temperature and mass vaporization history.

The Reynolds number in the droplet evaporation model (Eqn. 2.79) requires an estimate for the relative velocity V_{rel} between droplets and surrounding gas. Absent a two phase multidimensional solution for the spray, an approximation is made assuming a critical droplet Weber number for secondary breakup. Borman [6] suggests that in high pressure fuel sprays in engines, droplets may reach critical Weber numbers of 100 or greater before breakup. In this work, a critical Weber number of 100 is used. Then, an estimate of the relative droplet-gas velocity may recovered, under the assumption that most droplets are on the verge of breaking up in the highly turbulent spray. The cylinder averaged isotropic turbulence is also assumed to contribute to a higher droplet evaporation rate, and so the turbulence intensity u_t augments the relative droplet-gas velocity estimate:

$$(2.82) \quad V_{rel} = \sqrt{\frac{\sigma We_{crit}}{\rho d}} + u_t$$

2.9. TURBULENT COMBUSTION

Kong, et al. [49] present a model for CFD simulations that adjusts the rate of combustion according to the level of local turbulence in the cylinder. The combustion rate is thought to be influenced by the turbulent eddy turn over time that represents the time required to mix fuel and air down to the atomic level, and that local inhomogeneities must be smoothed out by turbulence for the chemical reactions to proceed.

At each time step, the chemical kinetics solver returns updated mole and mass fractions for each species. The new species mass fractions, corresponding to the end of the current time step, are represented by the $(n + 1)$ notation in Eqn. 2.83. The linearized rate of mass fraction change for each k -th species in each zone is:

$$(2.83) \quad \frac{dm_k}{dt} = m \frac{x_k^{(n+1)} - x_k^{(n)}}{\Delta t} f_\tau$$

In Eqn. 2.83, f_τ is a modulating factor that accounts for turbulence impacts on combustion, and is given by

$$(2.84) \quad f_\tau = \frac{\tau_k}{\tau_k + f_{cp}\tau_T}$$

The small scale turbulent mixing time scale is equal to the eddy turn over time τ_T , which is given by

$$(2.85) \quad \tau_T = \frac{k}{\epsilon}$$

where k is the turbulent kinetic energy and ϵ is the turbulence dissipation rate. f_{cp} represents the combustion progress and goes from 0 to 1 from combustion start to finish [50]. This assumes that ignition of fuel air mixture in a zone is a purely kinetically controlled event, and only subsequently does turbulence become a limiting process for the completion of combustion:

$$(2.86) \quad f_{cp} = \frac{1 - \exp(-r)}{0.632} \quad r = \frac{y_{CO} + y_{H_2O} + y_{CO_2} + y_{H_2}}{1 - y_{N_2}}$$

The kinetic time scale τ_k is set equal to the simulation time step, since the detailed kinetics inherently represent the reaction rates.

The small scale eddy turn over time τ_T is estimated using a simple cylinder-averaged turbulence model following the approach of Assanis and Heywood [9]. They proposed a zero-dimensional energy cascade concept in which the mean flow kinetic energy K generated by the fuel spray and squish geometry degrades into turbulent kinetic energy k , which in turn is converted to heat by viscous dissipation. P is the rate of conversion of mean flow K to turbulent k . Rates of change of the mean flow and turbulent kinetic energies are given by:

$$(2.87) \quad \frac{dK}{dt} = \frac{1}{2} \frac{dm_f}{dt} u_i^2 + \frac{1}{2} (\rho A_{sq} V_{sq}) V_{sq}^2 - P \quad \text{and} \quad K = \frac{1}{2} m U^2$$

$$(2.88) \quad \frac{dk}{dt} = P - m\epsilon + A_T \quad \text{and} \quad k = \frac{3}{2} m u_t^2$$

where m is the mass in the cylinder, u_i is the spray velocity, dm_f/dt is the spray mass flow rate, A_{sq} is the squish flow area, U is the representative mean flow velocity in the cylinder, and A_T is term for amplification of turbulence.

The turbulence production P comes from an expression for turbulence production in a boundary layer over a flat plate:

$$(2.89) \quad P = 0.3307 C_\beta \frac{K}{L} \sqrt{\frac{k}{m}} \quad C_\beta \approx 1$$

Turbulence dissipation is assumed to all occur at the same length scale:

$$(2.90) \quad \epsilon = \frac{u_t^3}{L} = \frac{(2k/3m)^{3/2}}{L}$$

The turbulence length scale L corresponds to the size of the most energetic eddies, which are roughly 1/6 the size of the largest eddy [46]. The largest eddy is assumed to be equal to the piston to crown distance, but limited to a maximum of half the bore.

Amplification of turbulence due compression according to rapid distortion theory follows [46]. Ignoring gas density changes due to changing composition yields:

$$(2.91) \quad A_T = -\frac{2}{3}k \frac{dV}{V}$$

The cylinder average turbulence intensity is shown as a function of squish area in Fig 2.10. Turbulence intensity increases rapidly during fuel injection, and then decays throughout the expansion stroke. In addition, a larger squish area results in higher mean flow velocities near top center, and leads to greater peak turbulence intensity.

2.10. PARCEL MIXING

Diesel sprays are highly turbulent structures that involve a large amount of fluid motion and mixing within the spray itself. Quasidimensional models, to date, have assumed no interaction among parcels, with each one tracking its own species mass and temperature in time. However, when using a detailed chemical kinetic model for combustion that cannot be easily calibrated to experimental results, the internal spray fluid interactions can no longer be avoided.

In this work, a simple model for parcel mixing is proposed. Mixing is assumed to occur among adjacent parcels along the same axial trajectory, but for simplicity, not among parcels at different radial positions within the spray. This may be justified by considering the interaction of the spray tip parcel with one immediately behind it. Upon injection, the first parcel enters a relatively quiescent gas and slows down. The next parcel slows down less because the gas in front of it is already in motion, and may actually overtake the first parcel's position. This behavior occurs primarily near the front of the spray, and less so in the tail. Mixing is also assumed to be higher towards the spray edge due to greater shear forces along the envelope with the surrounding gas.

The implementation of the parcel mixing model is as follows. After each integration time step (see Section 2.15), the contents of adjacent parcels along the same axial direction are mixed. For two adjacent zones, a fraction of each zone's mass (both total mixture and individual species mass) are combined and then redistributed back to the zones. The temperature of each zone is updated on "mixed-mass-weighted" average basis. The fraction of mass of each zone taken for mixing is given by:

$$(2.92) \quad f_{mix} = \frac{1}{2} \zeta_m \left(\frac{(i_{max} - i)}{i_{max}} + \frac{j + 1}{N_r} \right)$$

where i is the axial parcel position (0=tip, $i_{max} - 1$ =tail) and j is the radial position (0=centerline, $N_r - 1$ =edge). The parcel mixing intensity factor ζ_m is set to 1 for the simulations in this work. After the mixing is completed for all adjacent parcels, the chemical kinetics, evaporation, and entrainment processes are advanced forward in time independently for each zone without any zone-to-zone interaction.

This rather simplistic parcel mixing scheme appears to approximate the fluid dynamics adequately to yield a much better differentiation of the premixed and diffusion burn processes. A comparison of apparent heat release rate with and without parcel interaction will be presented with the results.

2.11. EMISSIONS MODELS

To calculate NO_x emissions, the thermal NO_x reactions in the GRI-3.0 natural gas mechanism were added to the base PRF mechanism [61, 62]. This involved four additional species (N, NO, N₂O, NO₂) and nine reactions. The original GRI rate constant parameters are used without modification. At the end of combustion, the sum of cylinder NO and NO₂ mass provides an estimate of the total engine-out NO_x emissions. Prompt NO_x is not modeled in this work, although it could be included with a sufficiently detailed chemical kinetic mechanism that properly accounts for important transient species.

Soot modeling follows the commonly used two-equation semi-empirical approach [2]. The net soot mass production rate equals the difference between the formation and oxidation processes. Soot formation is modeled as an Arrhenius rate process assuming that vaporized fuel molecules are the precursors to soot formation (Eqn. 2.93). The effect on model behavior of changing the precursor molecule is briefly explored in §5.2. The preexponential factor A_{sf} is set to 150 s^{-1} , and the activation energy E_{sf} is 12500 cal/mol, with pressure in atmospheres.

$$(2.93) \quad \frac{dm_{sf}}{dt} = A_{sf} m_{prec} P^{0.5} \exp\left(-\frac{E_{sf}}{R_u T}\right)$$

The Nagle and Strickland-Constable (NSC) model estimates soot oxidation rates based on the interaction of oxidation mechanisms at highly reactive A sites and less reactive B sites.

The net surface oxidation rate w , in $\text{g cm}^{-2}\text{s}^{-1}$, is given by:

$$(2.94) \quad w = M_C \left(\frac{k_A P_{O_2}}{1 + k_Z P_{O_2}} X_i + k_B P_{O_2} (1 - X_i) \right)$$

where M_C is the molecular weight of carbon (12 g/mol), P_{O_2} is the partial pressure of oxygen in atmospheres, and X_i represents the fraction of the soot particle surface populated by A-type reaction sites:

$$(2.95) \quad X_i = \left(1 + \frac{k_T}{k_B P_{O_2}} \right)^{-1}$$

The rate constants are:

$$(2.96) \quad \begin{aligned} k_A &= 20 \exp(-15100/T) && \text{g cm}^{-2}\text{s}^{-1}\text{atm}^{-1} \\ k_B &= 4.46 \times 10^{-3} \exp(-7640/T) && \text{g cm}^{-2}\text{s}^{-1}\text{atm}^{-1} \\ k_T &= 1.51 \times 10^5 \exp(-48800/T) && \text{g cm}^{-2}\text{s}^{-1} \\ k_Z &= 21.3 \exp(2060/T) && \text{atm}^{-1} \end{aligned}$$

The soot oxidation rate, assuming a representative soot particle density ρ_s of 2 g cm^{-3} and soot particle diameter of $2.5 \times 10^{-6} \text{ cm}$, is:

$$(2.97) \quad \frac{dm_{so}}{dt} = \frac{w}{\rho_s d_s} m_s$$

The soot model, unlike the NO_x model, is not part of the chemical kinetic mechanism and so soot mass is not conserved in the gas phase solution. The soot mass is integrated in time separately and so may offer only a very cursory estimate of soot levels.

2.12. HEAT TRANSFER

Heat loss from the cylinder considers both convective and radiative heat transfer modes. Convective heat transfer is calculated using the model of Assanis [9]. The model estimates an instantaneous heat transfer coefficient from a Nusselt number correlation for turbulent flow in a pipe.

$$(2.98) \quad \text{Nu} = a\text{Re}^b \quad \text{and} \quad h = \text{Nu} \cdot k/L$$

Suggested values for a range from 0.05 to 0.13 depending on the engine [9], and for the purposes here, a value of 0.08 is arbitrarily selected. The exponent b has been reported in the range 0.7 to 0.8 [9], and so 0.75 is used. The Reynolds number $\text{Re} = \rho V L / \mu$ uses the average cylinder gas density and the cylinder-averaged turbulence length scale (see §2.9). The characteristic velocity scales with any increase among the turbulence intensity, instantaneous piston velocity, and mean flow kinetic energy in the cylinder:

$$(2.99) \quad V = \sqrt{u_t^2 + (U_p/2)^2 + U_k^2}$$

Representative values of transport properties k and μ are calculated for air at the average cylinder temperature.

The total convective wall heat transfer is:

$$(2.100) \quad Q_{wall} = -h(A_c + \pi Bz)(\bar{T} - T_{wall})$$

Heat loss from radiation assumes that soot particles are the primary sources of radiative heat transfer to the cylinder walls, and ignores radiation from other gas molecules. The

radiative heat transfer rate from each zone is:

$$(2.101) \quad Q_{r,z} = -\epsilon_z \epsilon_{wall} \sigma \cdot A_z (T_z^4 - T_{wall}^4)$$

The effective surface area A_z is estimated as the area of a sphere enclosing the volume of the zone through which the radiative flux emanates. This simplified approach ignores the actual surface area of the soot particles, among which there is a large variation in size complicated by coagulation and oxidation processes, and ignores the view factor of each “soot cloud” to the wall.

$$(2.102) \quad A_z = [\pi(6V_z)^2]^{1/3} \quad \text{and} \quad V_z = \frac{m_z R_z T_z}{P}$$

An estimate for the grey-body emissivity of a soot cloud is given in [54] as:

$$(2.103) \quad \epsilon_z = 1 - \exp(-1575 \cdot x_s L T_i \rho / \rho_s)$$

The characteristic length L represents an effective mean free path length of the radiative transfer, and is set to the cylinder bore B . x_s is soot mass fraction in the zone, T_i is local zone temperature, ρ is cylinder average density, and ρ_s the soot particle density. The wall emissivity ϵ_{wall} is set to 0.5 as an arbitrary compromise between a clean shiny metallic surface and a lubricant coated surface with some accumulated exhaust deposits.

The cylinder wall temperature is set to a constant 370 K, and \bar{T} is the mass-weighted cylinder average temperature. The total heat loss is distributed to the zones on a mass-temperature weighting basis, and is included in the zonal dQ term in Eqn. 2.2. The heat

loss term for the i -th zone is:

$$(2.104) \quad Q_z = \frac{m_z T_z}{\sum_i m_i T_i} (Q_{wall} + Q_{evap}) + Q_{r,z}$$

where Q_{evap} is the total heat transfer to all liquid droplets in the cylinder for evaporation.

2.13. FUEL PROPERTIES

Temperature-dependent physical property relations for both diesel and biodiesel fuels have been comprehensively reported by Ra and colleagues [66]. The data presented by Ra were fitted to equations and used directly in this work. Fig. 2.13 shows both diesel and biodiesel properties as a function of temperature. Table 2.1 lists the molecular weight, critical temperature, and heating value assumed for the two fuel types. The biodiesel is representative of a typical soy-based methyl ester.

TABLE 2.1. Fuel properties.

Fuel	MW (g/mol)	T _{crit} (K)	LHV (J/g)
Diesel	198	690	42,900
Biodiesel	292	775	37,700

Key differences in properties are evident in Fig. 2.13. Biodiesel has a much lower vapor pressure and higher surface tension that will result in longer evaporation times relative to diesel fuel. In addition, the 12 % lower heating value of biodiesel should reduce thermal efficiency and indicated pressure by a similar percentage under equivalent operating conditions, relative to conventional diesel.

2.14. EQUIVALENCE RATIOS

When oxygen is present as part of a fuel molecule, conventional equivalence ratio calculations must be revised to account for the extra oxidizing agent within the fuel. The derivation

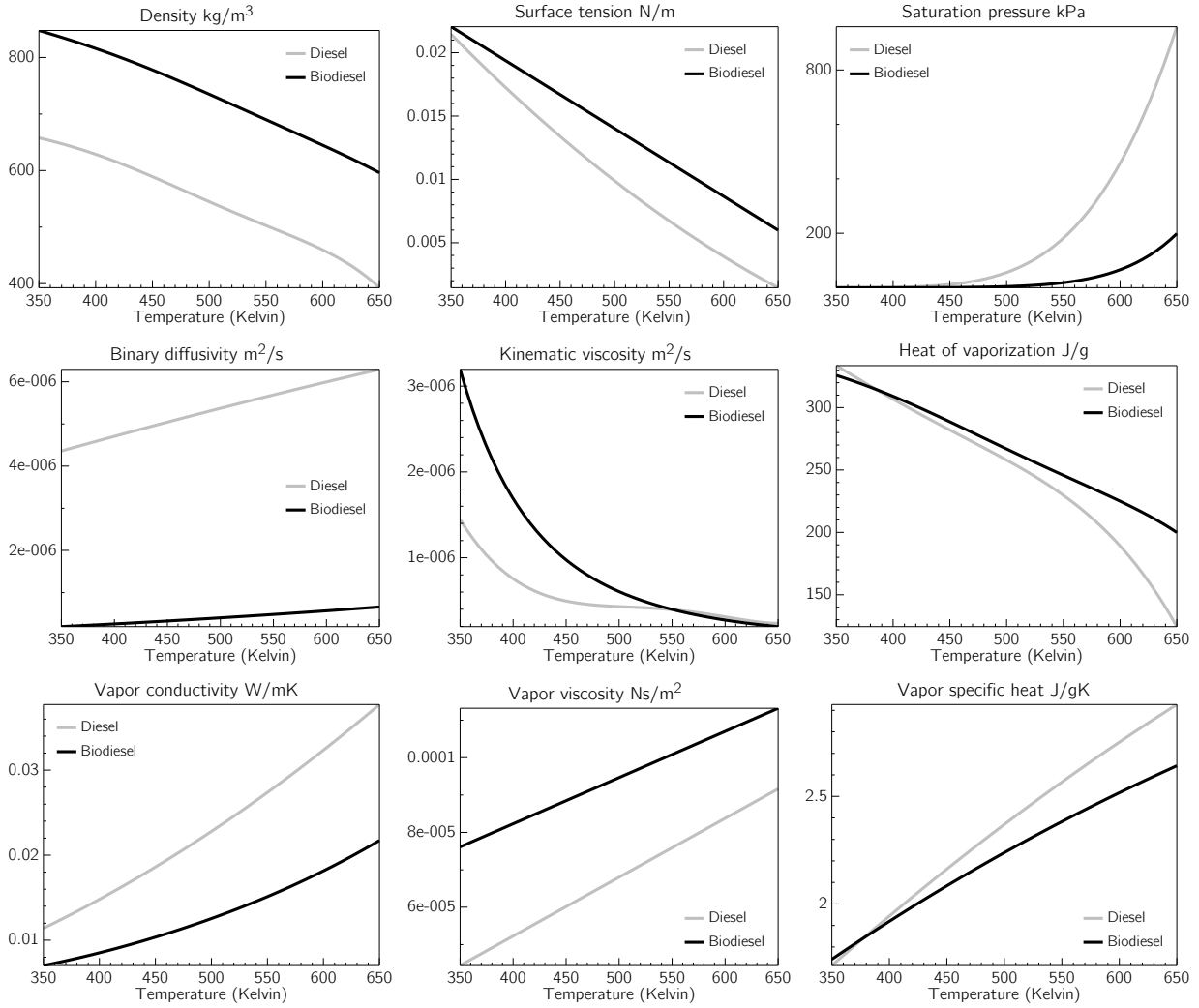
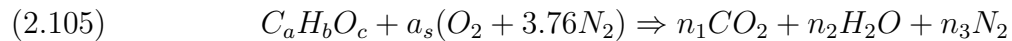


FIGURE 2.13. Fuel properties for diesel and biodiesel as a function of temperature.

follows [7]. Complete combustion of an oxygenated hydrocarbon fuel can be written as



The stoichiometric molar air-fuel ratio a_s is determined from balancing atoms:

$$(2.106) \quad a_s = a + \frac{b}{4} - \frac{c}{2}$$

Then, the stoichiometric mass air-fuel ratio is:

$$(2.107) \quad (AF)_s = \left(\frac{m_a}{m_f} \right)_s = \frac{28.85 \cdot 4.76 \cdot a_s}{12.01a + 1.008b + 15.99c}$$

For a gaseous mixture of multiple fuel species and air, the overall instantaneous equivalence ratio can be computed from calculating the total mass of air at stoichiometric conditions needed to completely burn the mass of each fuel species present. Then, the mass of air required at stoichiometric conditions divided by the available air in the mixture gives the equivalence ratio ϕ :

$$(2.108) \quad \phi = \frac{m_{air}(\phi = 1)}{m_{air}} = \frac{1}{m_{air}} \sum_k m_{f,k} \cdot (AF)_{s,k}$$

The instantaneous gas phase air mass is calculated from the available mass of oxygen and nitrogen, assuming an air composition of 21 % oxygen and 79 % nitrogen by volume.

The stoichiometric mass air-fuel ratios for each of the three surrogate fuel species used for biodiesel are listed in Table 2.2.

TABLE 2.2. Stoichiometric air-fuel ratios for biodiesel surrogate species.

Surrogate	Formula	MW (g/mol)	$(AF)_s$
n-heptane	C_7H_{16}	100.2	15.07
methyl decanoate	$C_{11}H_{22}O_2$	186.3	11.42
methyl-9-decenoate	$C_{11}H_{20}O_2$	184.3	11.17

2.15. SOLUTION PROCEDURE

The procedure used to advance the simulation forward in time is illustrated in Fig. 2.14. The method involves three phases: 1) evolving species concentrations in time due to chemical kinetics, 2) calculating spray, droplet behavior, and evaporation to determine the rates

of temperature and pressure change, and 3) resolving numerical issues and applying the phenomenological parcel mixing model. The chemistry phase for each zone is computed independently in parallel using all available computer CPUs, while the energy and transport equations are solved sequentially. The details of the procedure are outlined next.

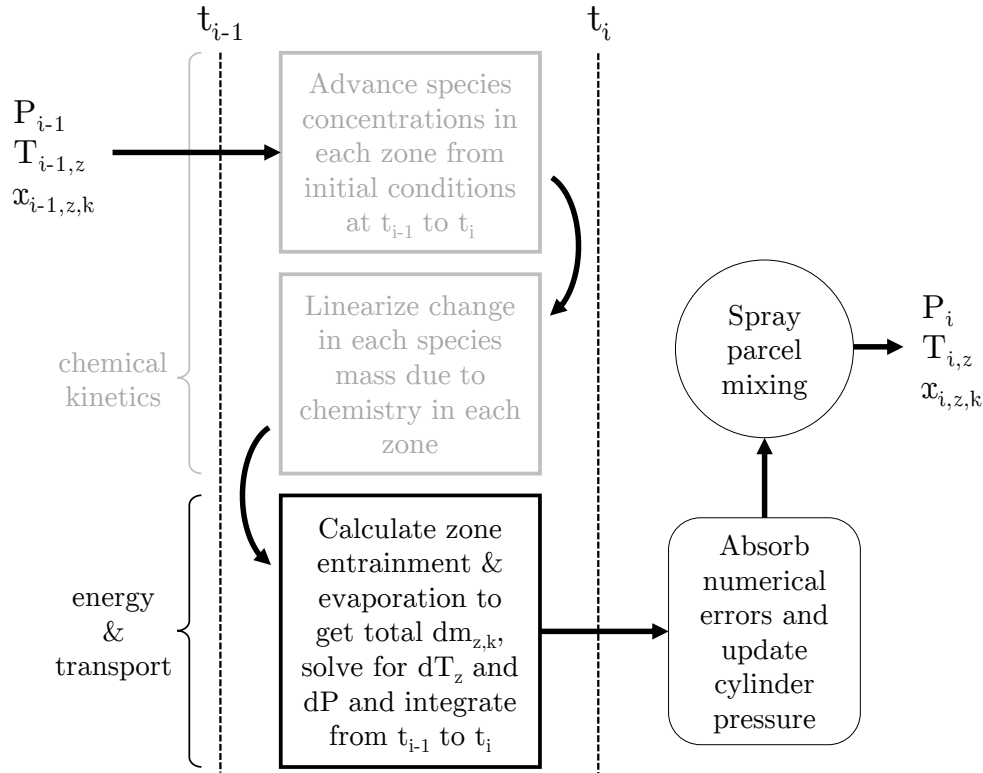


FIGURE 2.14. Block diagram of solution procedure to advance one time step.

- (1) Using the current cylinder pressure and zone temperatures, the chemical kinetics of each zone are independently advanced in time through the current time step. This is parallelized using multiple threads to fully utilize modern CPUs.
- (2) The change in species mass fraction from kinetics is linearized over the time step, accounting for turbulence effects on combustion (see Eqn. 2.83).
- (3) From the linearized mass fraction rates of change, the absolute mass rate of change of each species is calculated given the zonal mixture mass and provided as a source

term in the energy equation. The rates of mole fraction change dy_k are also updated (see §2.16).

- (4) The spray penetration, entrainment, evaporation, temperature, and pressure change equations are advanced forward in crank angle (or time) for all zones.
- (5) Numerical errors from integration are absorbed into nitrogen species in each zone so that the zone mixture mass equals the sum of zone species masses.
- (6) Numerical errors from integration in the cylinder pressure are compensated by recalculating the cylinder pressure based on the new zone masses and temperatures:

$$(2.109) \quad P = \frac{1}{V_c} \sum_z m_z R_z T_z$$

- (7) Mixing among spray parcels is applied according to the procedure in §2.10.
- (8) The process repeats with the new cylinder pressure and zonal temperatures.

The energy and transport equations are integrated using a standard 4th-order Runge-Kutta scheme. The decoupled chemical kinetics use the implicit backwards differentiation formulae (BDF) solver from the CVODE package [45].

2.16. CALCULATION OF SPECIES MOLE FRACTION CHANGE

The energy equation for a zone is written in a form to calculate rate of temperature change (see Eqn. 2.10):

$$(2.110) \quad dT = \frac{1}{mc_p} \left(dQ - u dm - m \sum_k^N u_k dy_k - m T dR - R T dm + \sum m_i h_i \right) + \frac{RT}{P c_p} dP$$

The term $m \sum_k u_k dy_k$ is more complicated than it appears at first glance. The mole fraction rates of change dy_k are driven by a mix of chemical kinetics, entrainment of air, and fuel evaporation. Internally, the model tracks the mass and mass rates of change of each species, and so the mole fractions and rate of mole fraction changes must be determined from the mass variables. Denoting mass fraction of species k as x_k , and m as the total mass in a zone:

$$(2.111) \quad dx_k = d(m_k/m) = -\frac{m_k}{m^2} dm + \frac{1}{m} dm_k$$

$$(2.112) \quad \bar{M} = \sum_k y_k M_k \quad \text{and} \quad y_k = \frac{x_k \bar{M}}{M_k}$$

$$(2.113) \quad dy_k = \frac{1}{M_k} \left(x_k \sum_j dy_j M_j + \bar{M} dx_k \right)$$

Rewriting gives an equation for dy_k , but it clearly depends on all the other dy_j also, and so must be solved in matrix form or other method.

$$(2.114) \quad dy_k (1 - x_k) - \frac{x_k}{M_k} \sum_{j \neq k} dy_j M_j = \frac{\bar{M}}{M_k} dx_k$$

(2.115)

$$\begin{bmatrix} 1 - x_0 & -x_0M_1/M_0 & -x_0M_2/M_0 & \cdots & -x_0M_j/M_0 \\ -x_1M_0/M_1 & 1 - x_1 & -x_1M_2/M_1 & \cdots & -x_1M_j/M_1 \\ -x_2M_0/M_2 & -x_2M_1/M_2 & 1 - x_2 & \cdots & -x_2M_j/M_2 \\ \vdots & & & \ddots & 0 \\ -x_kM_0/M_k & -x_kM_1/M_k & -x_kM_2/M_k & \cdots & 1 - x_k \end{bmatrix} \begin{bmatrix} dy_0 \\ dy_1 \\ dy_2 \\ \vdots \\ dy_k \end{bmatrix} = \begin{bmatrix} \bar{M}dx_0/M_0 \\ \bar{M}dx_1/M_1 \\ \bar{M}dx_2/M_2 \\ \vdots \\ \bar{M}dx_k/M_k \end{bmatrix}$$

This matrix equation may be solved by Gaussian elimination for the dy_k . In practice however, the matrix is full of many very small numbers, and division by these values results in problems with numerical accuracy, even when using a maximum column pivoting algorithm.

Thus, Eqn. 2.114 is solved iteratively using successive substitution until the maximum difference between iterations of any dy_k is below a tolerance of 1 %. The iterative solution is started with initial guesses $dy_k = dx_k\bar{M}/M_k$. This “brute force” method works, but is slow and is worthy of improvement in the future, possibly with a Newton’s method-type algorithm, provided that the numerical accuracy issues can be avoided.

2.17. SUMMARY

This chapter presented the details of the quasidimensional spray model’s mathematical modeling and solution procedure. Subsequent chapters will evaluate the model’s predictions compared to published experimental data, and test the computational robustness and efficiency of the new approach.

CHAPTER 3

VALIDATION WITH DIESEL ENGINE EXPERIMENTS

3.1. OVERVIEW

In this chapter, model predictions are presented alongside published experimental heat release rate and pressure data for three engines. Engine specifications and model parameters are listed in Table 3.1. Because intake and exhaust processes are not modeled, the bottom dead center pressure and temperature were adjusted in each case to match the experimental pressure data prior to the onset of combustion. The start of injection is also retarded, by inspection, up to 1 degree relative to reported timings to account for injector dynamics that are not explicitly modeled. Running the model at 0.25 degree crank angle steps from -180 to 180 degrees with 10 radial spray zones, 5 droplet size bins per zone, and 18 degrees of fuel injection takes roughly 25 minutes on a 3.3 GHz i7-5820k six core processor.

3.2. BASELINE SCENARIO

Engine 1 is a heavy duty multi-cylinder diesel engine described in [25]. The baseline scenario is defined as 50 % load at 1800 rpm. A comparison of predicted versus experimental heat release rate and pressure are shown in Fig. 3.1.

Overall, there is good agreement with respect to the timing of ignition, peak pressure, peak pressure timing, and overall heat release shape and magnitude. This is an encouraging result given that there are no empirical combustion rate calibration constants in the model. However, the model appears to underpredict the peak premixed heat release rate, as well as its duration relative to the diffusion burn. Although this may be partially accounted for by the noise in the experimental heat release rate data, further work to improve the

TABLE 3.1. Engine and model parameters.

Parameter	Engine 1	Engine 2	Engine 3	Units
Bore	130	137	139	mm
Stroke	160	165	152	mm
Compression ratio	15	15	10	
Engine speed	1800	1600	1200	rpm
Squish area fraction	0.6	0.5	0.7	
Swirl ratio at BDC	1	1	1	
Temperature at BDC	330	309	433	K
Pressure at BDC	1.5	1.65	2.06	bar
Injector pressure	900	900	680	bar
Discharge coefficient	0.64	0.46	0.42	
Nozzle diameter	0.2	0.259	0.194	mm
Nozzle L/D ratio	3	3	4	
Number of nozzles	6	6	8	
Injection start	-13	-9	-11.5	deg
Injection duration	18	18	11	deg

phenomenological treatment of the spray fluid mechanics may yield improved results in this aspect.

A second comparison with experimental data is made at a slower engine speed. The parameters in Table 3.1 are retained but for the modifications indicated in Fig. 3.2. At the slower speed, more time is available for evaporation before ignition, and so the premixed burn phase accounts for nearly all of the total heat release. Again, good agreement is observed, particular when considering the lack of combustion model calibration to the data.

3.3. EVALUATION OF SUBMODELS

Next, the detailed behavior of several submodels is presented. Collectively, these indicate proper functioning of all the models representing the injection, evaporation, combustion, and emissions formation processes.

The mass of fuel injected, vaporized, burned, and total hydrocarbons burned is shown in Fig. 3.3 for the baseline condition. At the onset of premixed combustion, at about -7 crank

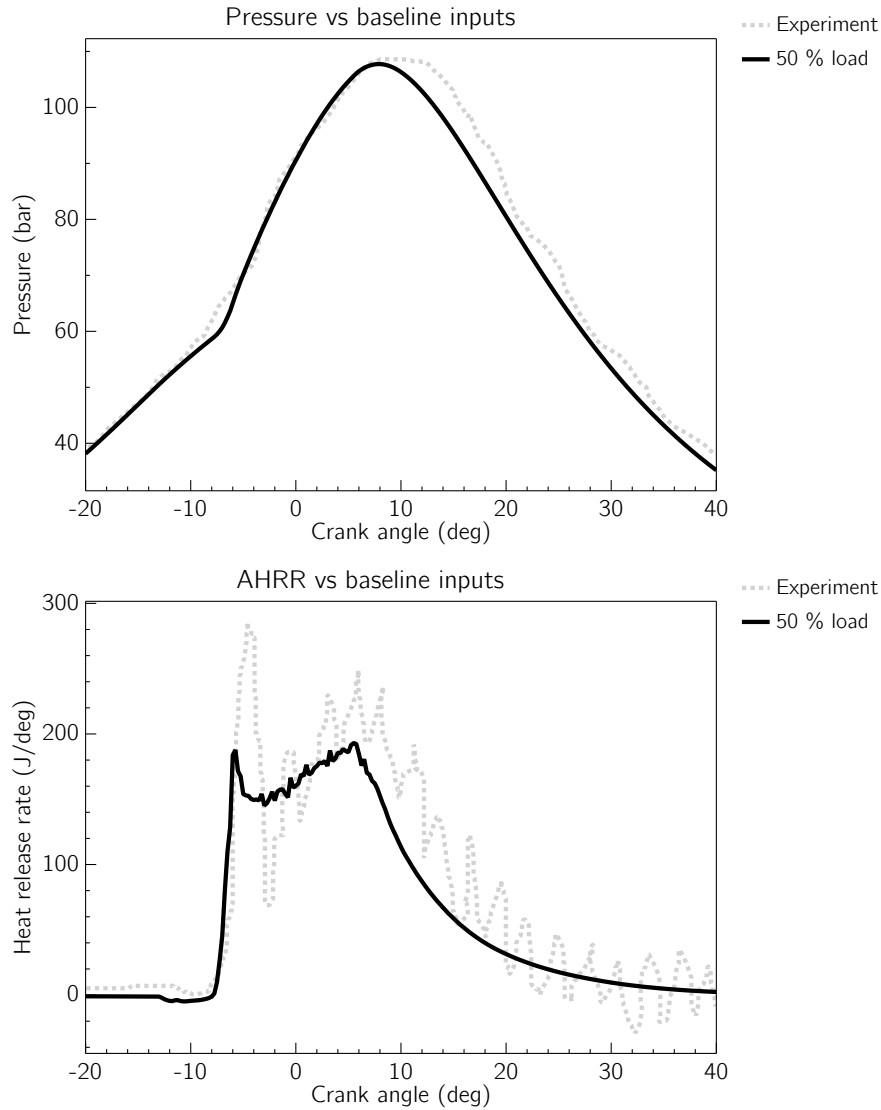


FIGURE 3.1. Engine 1, 50 % load @ 1800 rpm, pressure and AHRR.

angle degrees (CAD), nearly 50 % of the fuel injected up to that point has been vaporized. The reasonable progression from injected to burned fuel suggests that these submodels are working correctly. Fig. 3.4 shows the instantaneous mass fractions at each crank angle of injected, vaporized, and burned fuel in the cylinder.

Fig. 3.5 shows temperatures of various portions of the spray. The spray tip burns first and hottest under increasing pressure conditions, while the tail of the spray, after an initial spike, cools more quickly during the expansion stroke. The local peak combustion temperatures

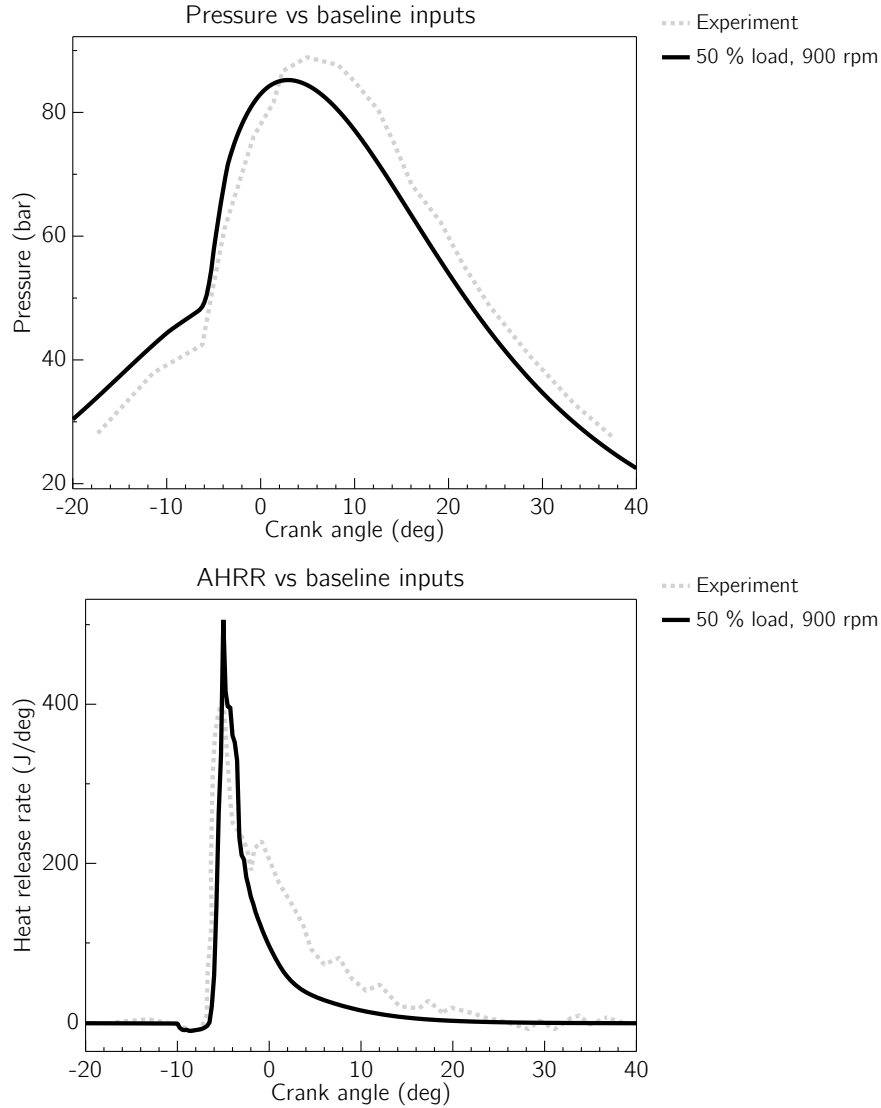


FIGURE 3.2. Engine 1, 900 rpm, pressure and AHRR. $\theta_i = -11$, $\theta_d = 5$, $P_{BDC} = 1.2$ bar

at both ends of the spray are quite hot, nearly reaching 3000 K. Artifacts of the two stage ignition process modeled by the detailed chemical kinetics are observable for the spray tip temperature, where an initial short rise is followed by a much greater and more rapid increase in temperature.

Fig. 3.6 shows overall heat transfer to the cylinder wall. Peak radiative heat transfer from hot soot particles reaches roughly 25 % of the total heat transfer rate after top center.

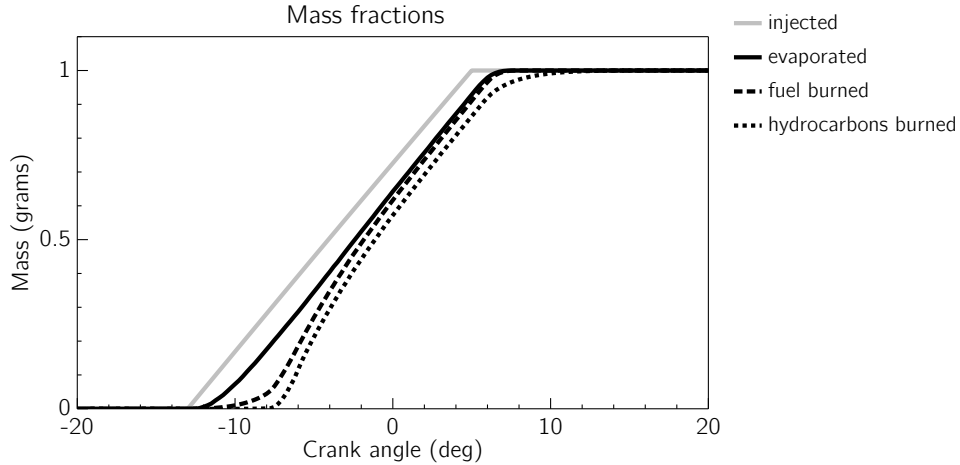


FIGURE 3.3. Injected, vaporized, fuel burned, and hydrocarbon burned mass fractions for the baseline case.

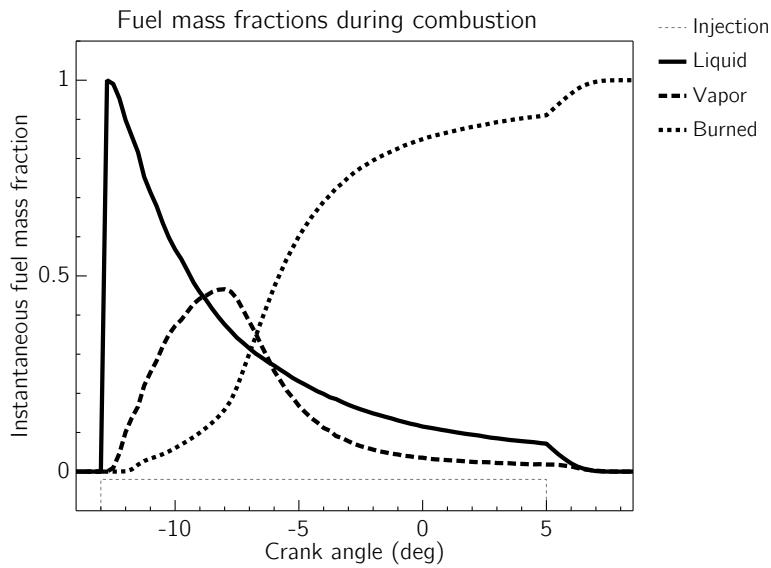


FIGURE 3.4. Instantaneous fractions of injected, vaporized, and burned fuel mass.

Peak flux of around 15 MW/m^2 seems reasonable for an engine operating at 50 % load. Instantaneous levels of soot and NO_x in the cylinder are shown Fig. 3.7. Soot production starts first, shortly after the onset of premixed combustion. NO_x follows, with the primary NO_x producing period occurring during the diffusion flame period. The spatial distribution of emissions products will be explored in more detail subsequently.

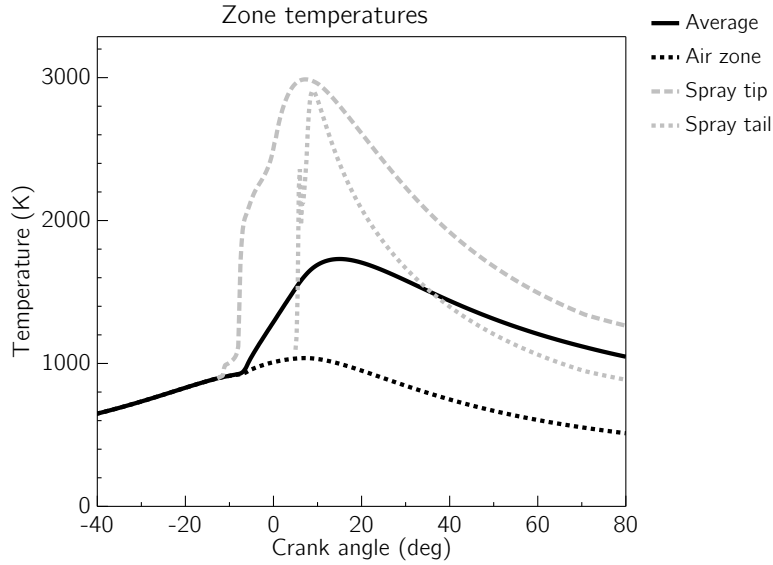


FIGURE 3.5. Predicted zone temperatures for engine 1, baseline.

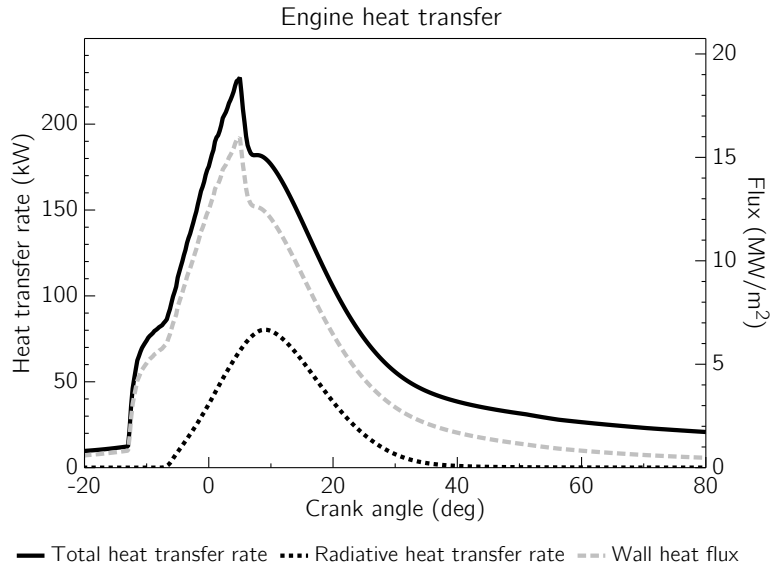


FIGURE 3.6. Predicted total and radiative heat transfer for engine 1, baseline.

3.4. EVALUATION OF SPRAY STRUCTURE

Figs. 3.8 and 3.9 show the spatial evolution of structures within the reacting fuel spray at several intervals after the start of injection. Consistent with detailed observations and modeling in [8] and [56], the maximum liquid phase fuel penetration (“liquid length”) appears

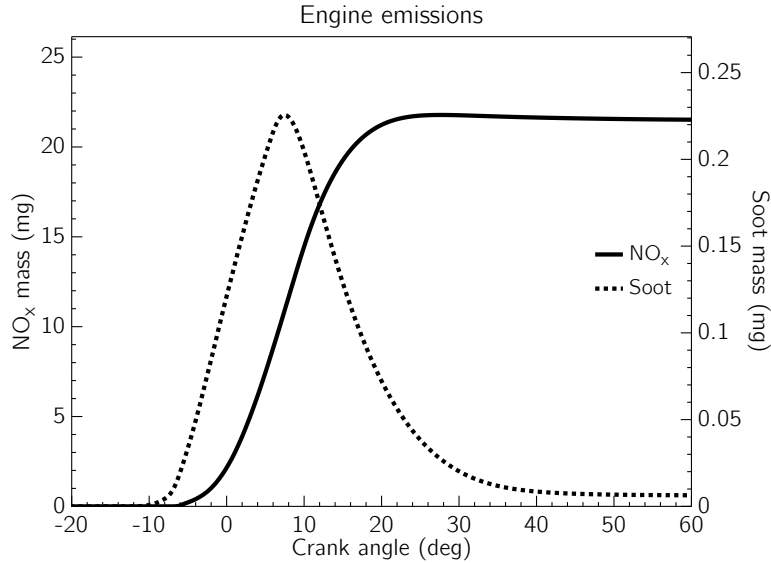


FIGURE 3.7. Predicted NO_x and soot emissions for engine 1, baseline case.

to stabilize downstream of the nozzle at a point notably shorter than the overall spray tip penetration length. It is also clear from the adjacent temperature distribution that vaporization occurs primarily upstream of combustion. As combustion proceeds, the liquid length is observed to shorten due to increasing cylinder temperatures and more rapid vaporization.

Although the absolute magnitude of engine-out emissions levels for engine 1 baseline conditions cannot be confirmed due to an absence of reported experimental measurements, Fig. 3.9 shows that the locations of soot and NO_x in the spray are generally consistent with current understanding of diesel spray behavior. NO_x is produced primarily at the boundary of the diffusion flame, where there is simultaneous availability of both oxygen and nitrogen at high temperatures. Soot production occurs primarily towards the inside of the spray envelope at more moderate temperatures in the range of 1500-2000 K, which are consistent with the initial higher equivalence ratio premixed burning process. As [58] observes, the premixed burn phase may be considered as more of a continuous process near the lift-off location in the reacting spray rather than an initial transient that gives way to the diffusion

flame. The observed soot production in Fig. 3.9 seems consistent with this conceptualization, as the sooting region appears to stabilize near the apparent flame lift-off length and elongate into the interior of the spray structure.

Due to the simplified phenomenological approach to the fluid mechanics, no traveling turbulent head vortex structure is observed in the spray [34]. Flame lift-off [57, 55], however, is clearly visible in the temperature distribution. Overall, the model appears to do a decent job of capturing the interplay among key physical processes in an atomizing chemically reactive liquid fuel spray.

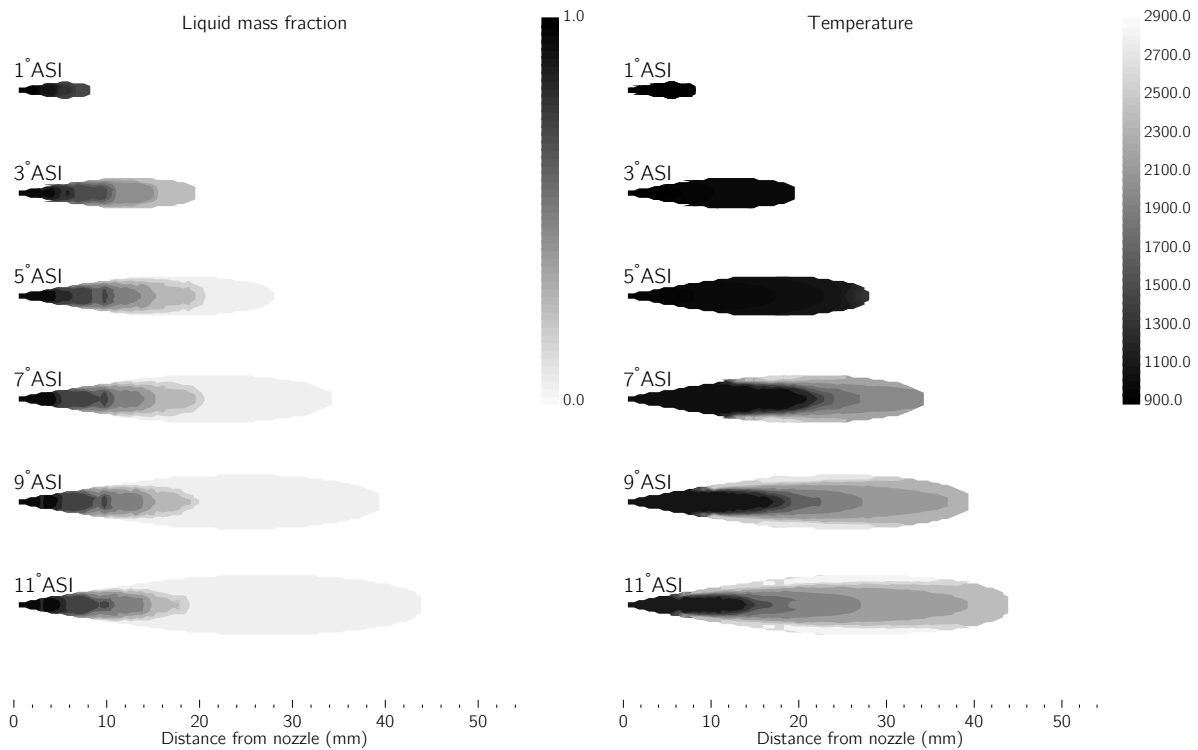


FIGURE 3.8. Engine 1, spray liquid mass fraction and temperature distribution.

Another useful visualization of the combustion process is the $\phi - T$ map. Fig. 3.10 shows the progression of parcels in temperature and equivalence ratio at various crank angle degrees after start of injection. At higher loads, a greater fraction of the parcels are at high temperatures that are within the NO_x producing contours leading to higher engine-out NO_x .

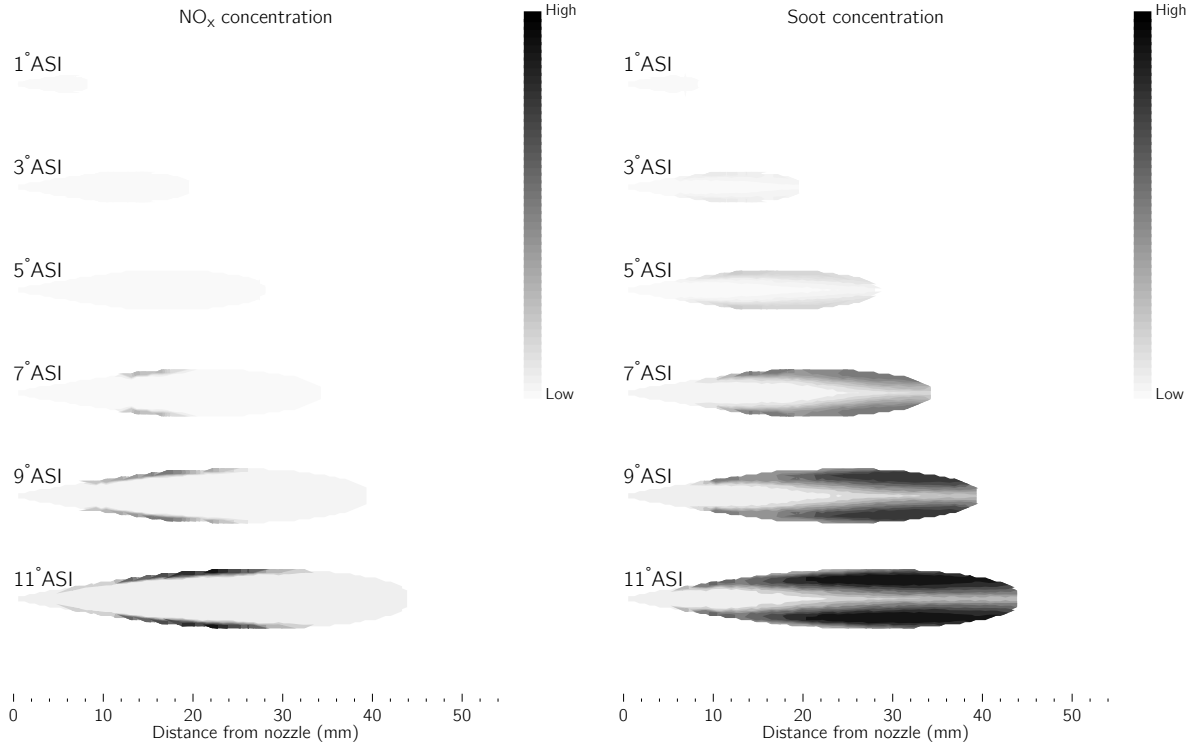


FIGURE 3.9. Engine 1, NO_x and soot locations.

3.5. SENSITIVITY TO KEY SUBMODELS

In this section, the sensitivity of the apparent heat release rate to a selection of submodels is considered. The impact of the parcel interaction scheme described in §2.10 is investigated first. As evident in Fig. 3.11, disabling the parcel mixing sub-model results in no apparent premixed burn phase at all, with all of the heat release occurring in a diffusion flame. Enabling parcel mixing increases species homogeneity particularly towards the spray tip, meaning that more of the premixed fuel and air burns at the same time, after the ignition delay, but before the diffusion flame is fully developed around the envelope. Despite the fairly simplistic nature of the mixing model, it provides good evidence that the characteristic premixed burn process in diesel combustion is largely a result of a high degree of turbulent mixing within the spray envelope itself.

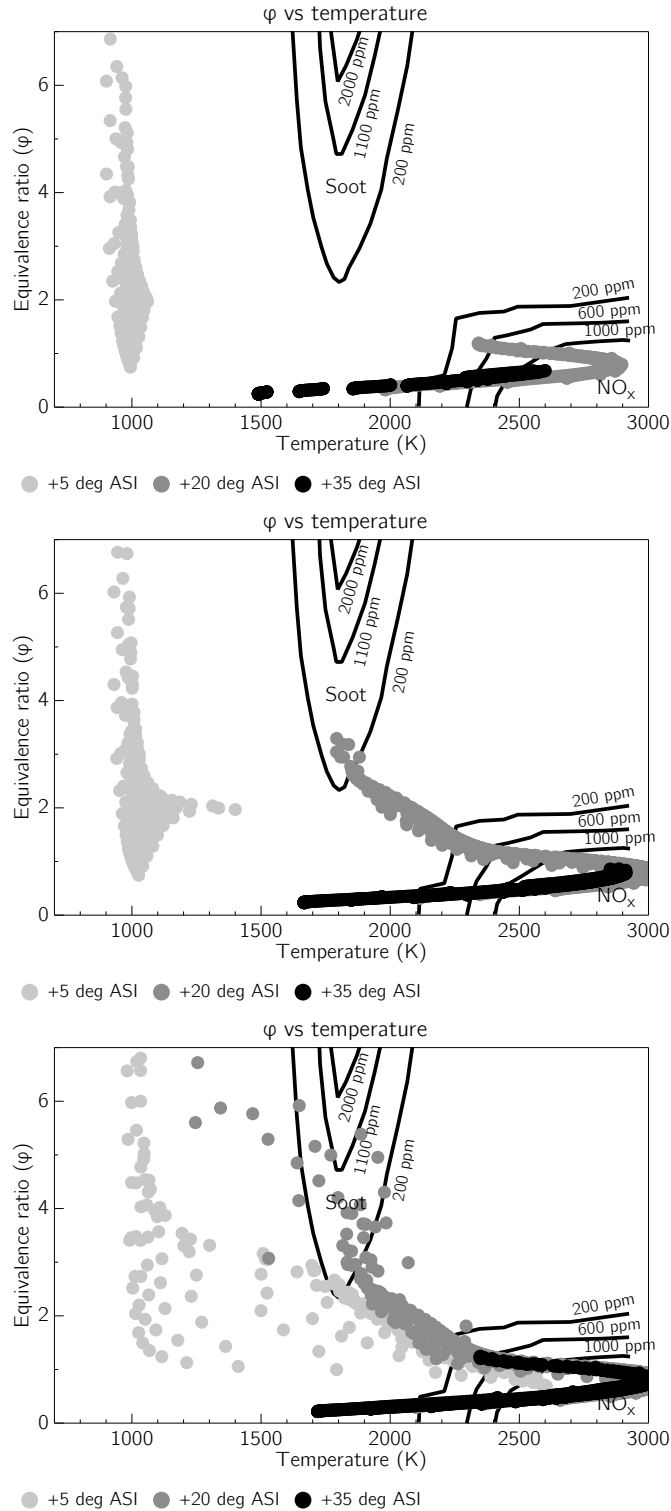


FIGURE 3.10. Engine 1, ϕ vs. temperature @ 1800 rpm (a) 25 % load, (b) 50 % load, (c) 75 % load

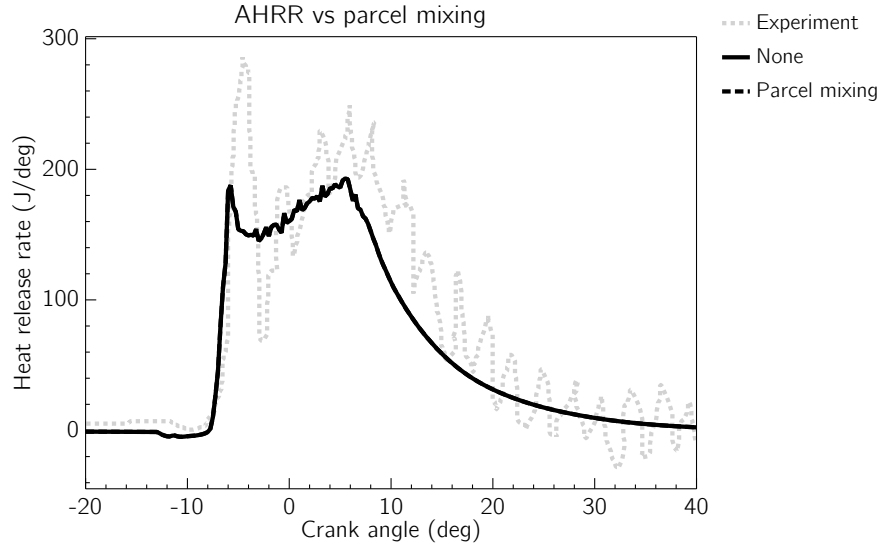


FIGURE 3.11. Engine 1, AHRR with and without parcel mixing model.

Next, heat release rate predictions of the Ra 2008 [66] primary reference fuel kinetic mechanism are compared with those of the more detailed mechanism of Wang 2013 [44]. The Ra mechanism has 41 species and 130 reactions, compared with 73 species and 296 reactions for the Wang mechanism. Heat release rates are shown in Fig. 3.12 for both. While the overall magnitudes and timing are quite similar, the smaller mechanism appears to predict a more pronounced premixed burn peak, while the more detailed mechanism shows a earlier ignition and a smaller premixed phase.

Some ambiguity remains as to how to interpret the sensitivity to one’s choice of primary reference fuel mechanism. While presumably the more detailed mechanism would be preferred in most situations, it may be possible that due to the inherent limitations of the spray parcel concept compared with a full multidimensional CFD model, the smaller mechanism may present a more compatible level of complexity. At any rate, it does not appear that a more detailed mechanism affords much greater insight into model behavior despite the significantly larger computational burden.

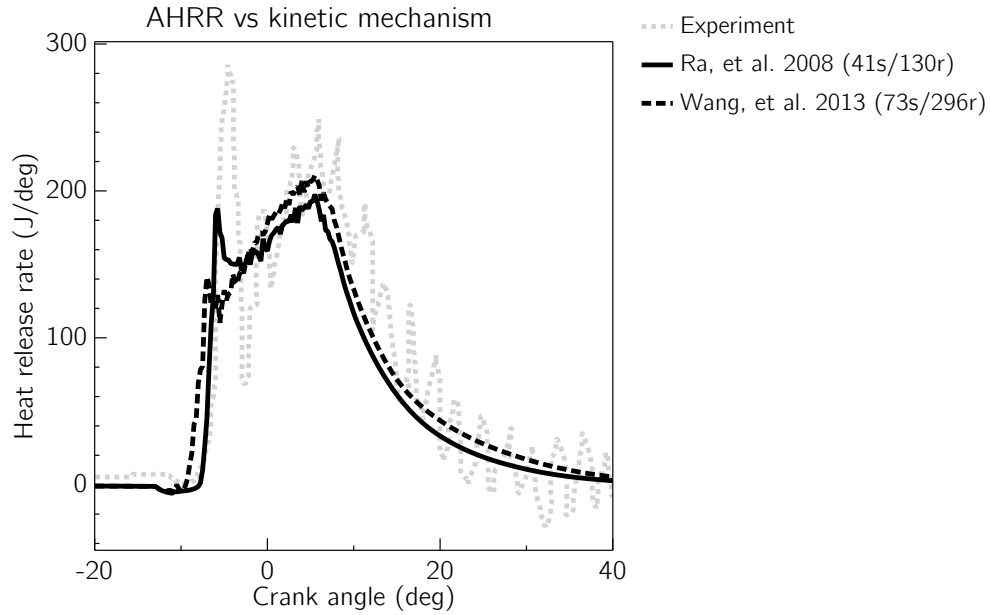


FIGURE 3.12. Engine 1, sensitivity to chemical kinetic mechanism, baseline conditions.

Finally, the model’s sensitivity to flow behavior parameters is assessed. Figs. 3.13 and 3.14 show the impact of initial BDC swirl ratio $R_{S,0}$ and piston bowl shape.

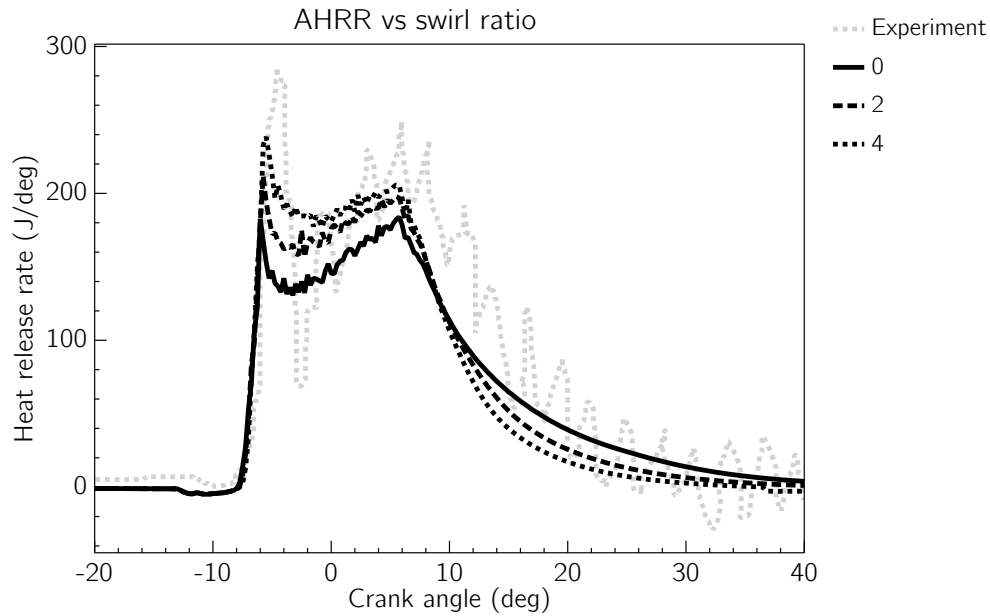


FIGURE 3.13. Engine 1, swirl ratio sensitivity.

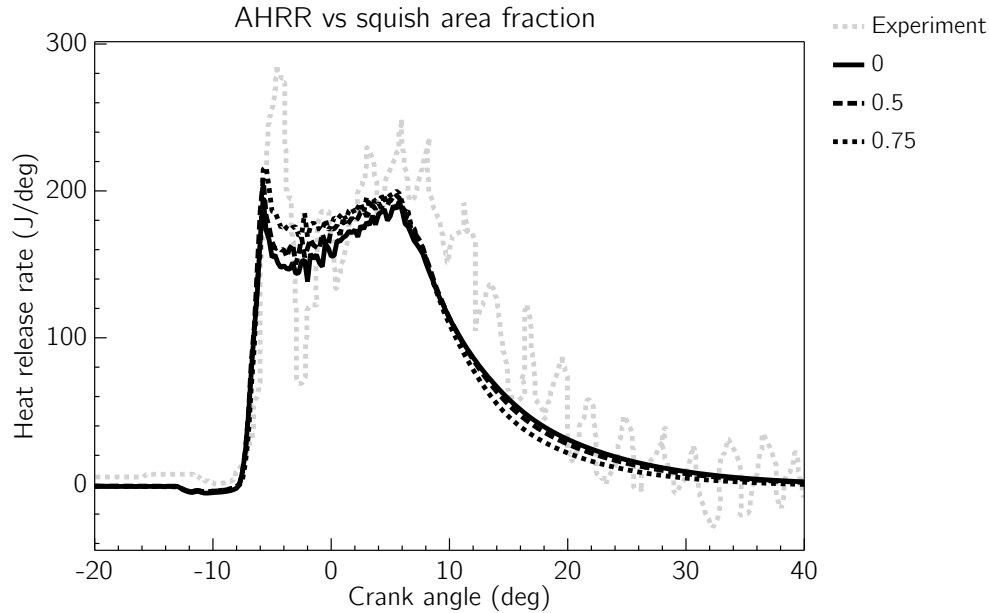


FIGURE 3.14. Engine 1, piston bowl size sensitivity for swirl ratio of 2.

The model responds reasonably to changes in the fuel-air mixing process. Starting with a higher swirl ratio at bottom dead center has a pronounced impact on the heat release rate shape. More vigorous fuel-air mixing due to amplified swirl and faster vaporization from higher turbulence results in a greater fraction of mixture within flammability limits upon ignition and the higher peak premixed heat release. The overall heat release is shifted earlier in the cycle, with a faster drop off towards the tail of the diffusion burn. Larger squish area fractions, which correspond to deeper and narrower piston bowls, result in more intense rotational motion and yield similar trends. Overall, these results suggest that the interplay among various modeled flow behaviors are working properly.

3.6. PREDICTION OF POLLUTANT EMISSIONS

Engine 2 is a single cylinder version of a Caterpillar 3406 diesel engine at the University of Wisconsin Engine Research Center that has been extensively evaluated [60, 59]. Specifications and other model parameters are listed in Table 3.1. For this model, an injection

start timing of -9 degrees is used, instead of the -11 degrees reported. The experimental -11 degrees corresponds to the needle lift signal, but the injector flow does not fully develop for nearly two degrees (see Fig. 2 in [59]). Since this model does not consider injector dynamics, a value of -9 degrees is chosen. Fig. 3.15 shows very good agreement between predicted and measured cylinder pressure. The heat release rate shape compares well, even though premixed burn phase is underpredicted both in terms of duration and peak heat release. Again, just as observed in heat release rates for engine 1, improvements to the simplified spray fluid dynamics may result in better characterization of the premixed burn phase.

Extensive data for the test engine NO_x and soot emissions are reported in [59]. Engine out emissions normalized to brake horsepower at the baseline conditions are reported in Table 3.2. Modeled soot is about 2/3 of measured, and modeled NO_x is nearly 4 times too high at the baseline conditions. A possible explanation for this discrepancy is likely to be found once again in the limitations of the spray fluid dynamics modeling. Even slightly too high local temperatures may result in greatly increased rates of NO_x formation. Thus, using the detailed thermal NO_x mechanism from GRI-3.0 imposes a much greater burden on the phenomenological model since it cannot be readily calibrated to each particular situation.

TABLE 3.2. Predicted vs measured engine-out emissions.

Engine 2, baseline	Soot (g/bhp-hr)	NO_x (g/bhp-hr)
Experiment	0.104	3.90
Modeled	0.068	15.4

Despite the differences in total NO_x levels, the typical soot versus NO_x tradeoff curve is readily obtained from the model (Fig. 3.16). Advanced injection timings push the combustion process to occur at high pressures near top center and thus higher temperature, resulting in greater rates of NO_x formation. As injection is retarded, combustion temperatures are

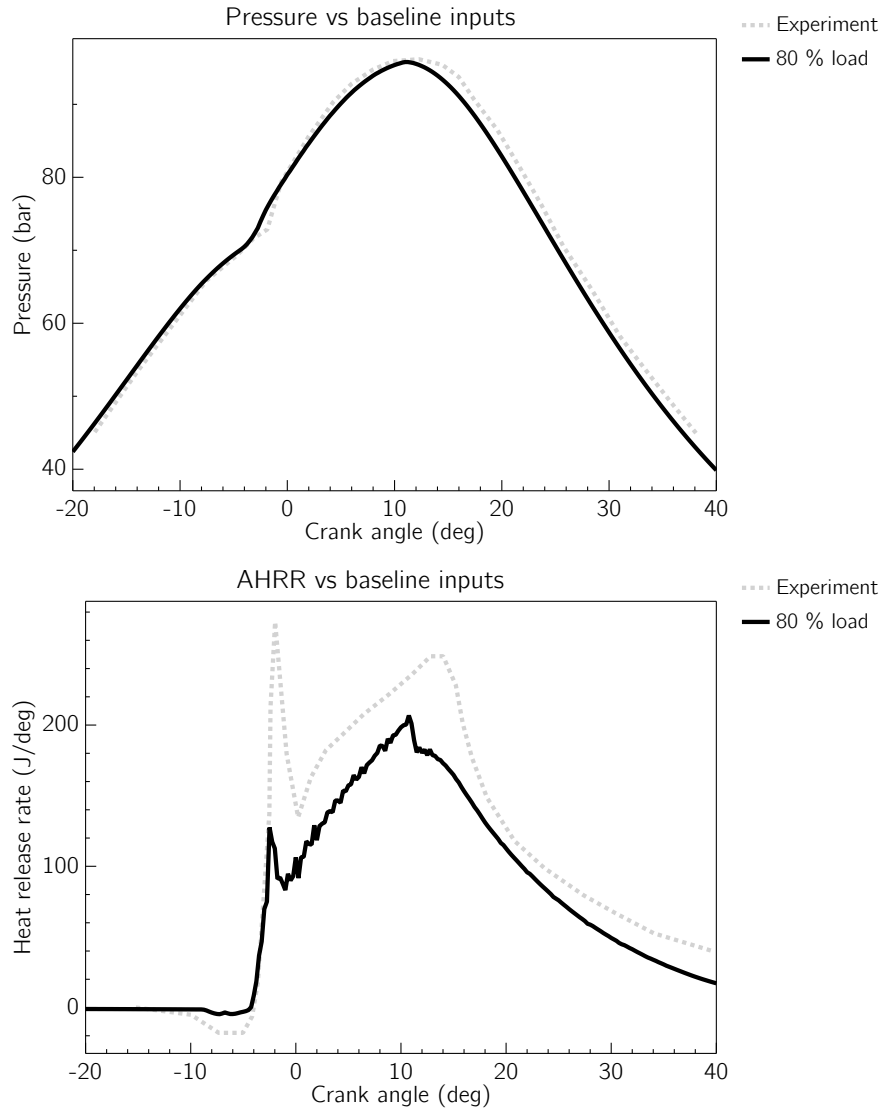


FIGURE 3.15. Engine 2, 80 % load, 1600 rpm, pressure and AHRR.

lowered, and tend to move combustion into regimes favoring soot production in the 1500-2000 K range. Additionally, cooling effects due to increased radiative heat transfer from soot lowers temperatures and thus NO_x .

3.7. OPTICAL TEST ENGINE EVALUATION

Finally, predicted pressure, heat release, and spray structure are compared with experimental results from an optically accessible engine used for the combustion imaging studies

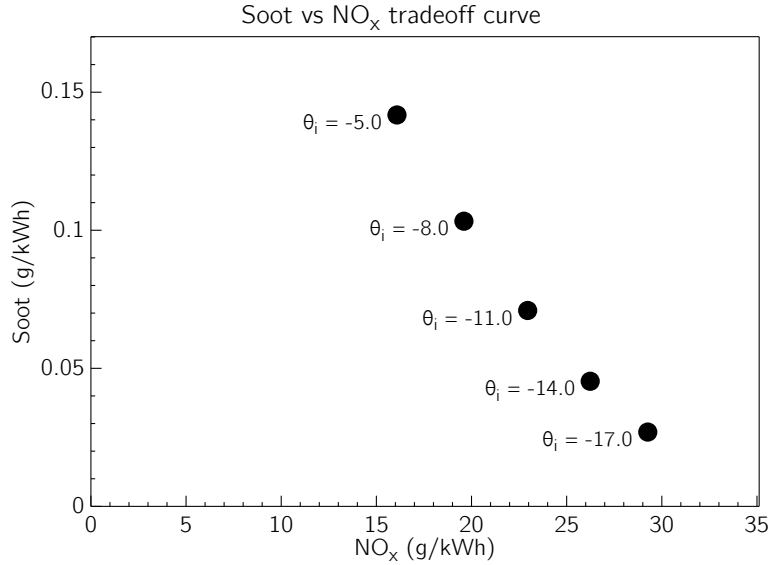


FIGURE 3.16. Engine 2, modeled soot versus NO_x tradeoff curve.

in [8]. The single cylinder engine is based on a Cummins N-series heavy duty diesel. Similar to the results for engine 2 in the previous section, Fig. 3.17 shows good overall agreement in cylinder pressure but some notable differences in heat release rate. The small premixed burn phase is quickly dominated by the onset of a diffusion flame, and the overall heat release is shifted later accounting for the higher modeled down-slope cylinder pressure.

Fig. 3.18 shows 2-D visualizations of the modeled spray processes. The maximum liquid length is somewhat shorter at roughly 15 mm than the conceptual representation of Dec (Fig. 17 in [8]) that shows liquid length of about 20 mm. From Fig. 3.17, combustion starts approximately 4-5 degrees after start of injection, which corresponds to the rapid drop in observed local equivalence ratio in the forward parts of the spray as the fuel molecules are consumed in this region. Also, the total equivalence ratio, including any remaining liquid fuel, just prior to combustion in this phase is in the range of 2-4 in accordance with Dec's conceptual model.

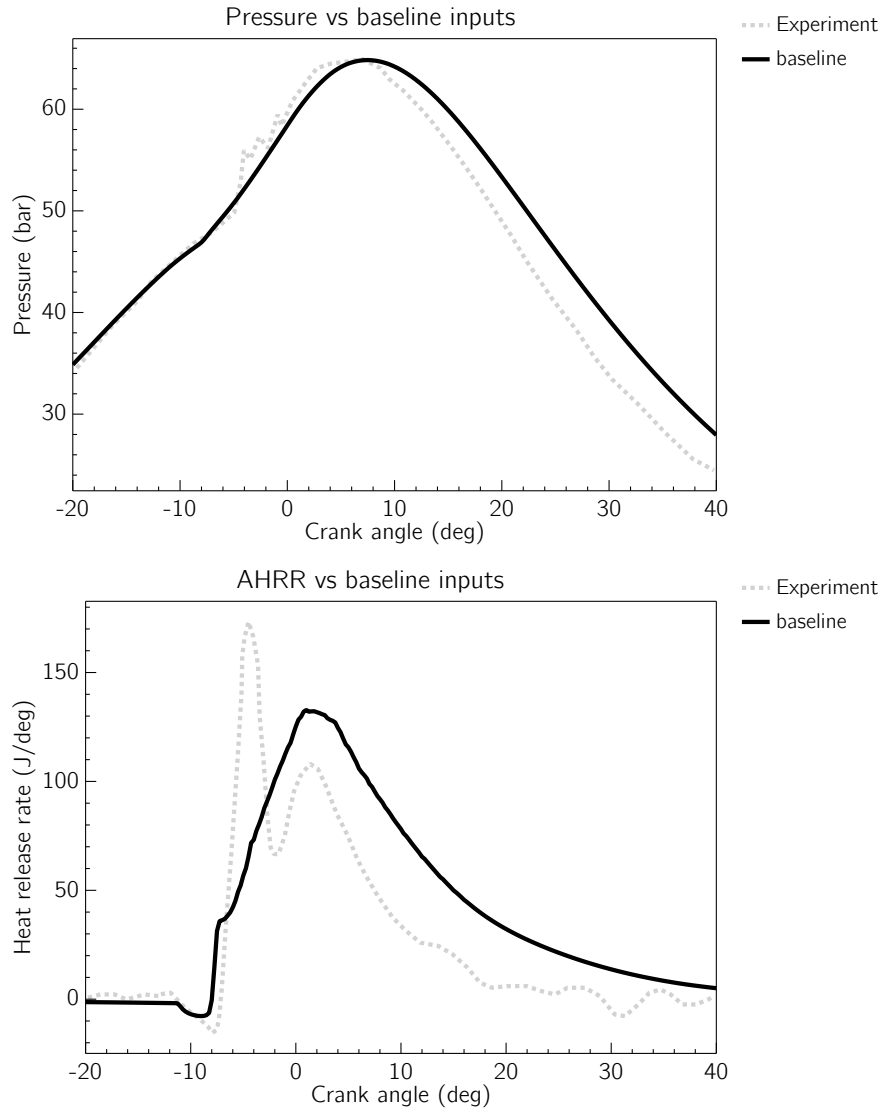


FIGURE 3.17. Engine 3, pressure and heat release rate comparison

3.8. SUMMARY

This chapter presented a detailed evaluation of model behavior and comparison with experiment for several diesel engines. Good agreement with data was obtained overall, particularly given that the model did not require calibration to data. In the next chapter, the predictive capability of the model is leveraged to compare diesel and biodiesel combustion behavior and better understand biodiesel NO_x emissions formation processes.

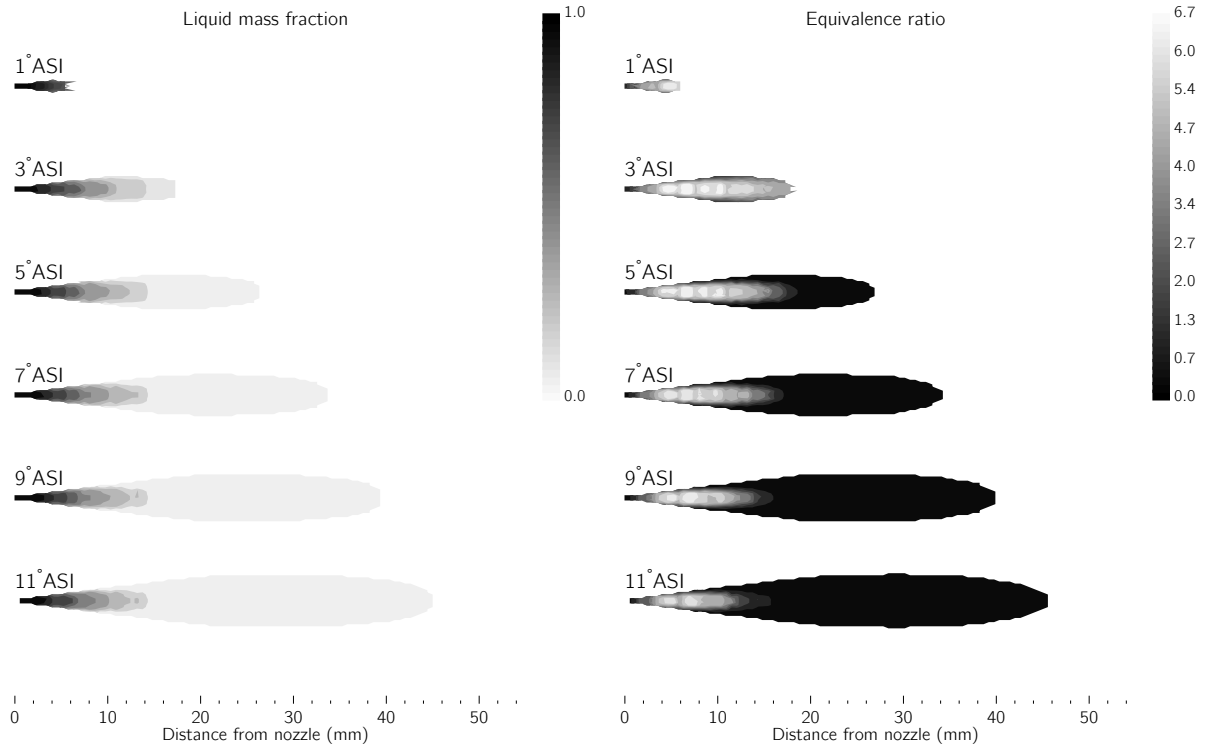


FIGURE 3.18. Engine 3, liquid mass fraction and instantaneous gas phase equivalence ratio inside reacting fuel spray.

CHAPTER 4

INVESTIGATION OF BIODIESEL SPRAYS

4.1. OVERVIEW

This chapter is arranged as follows. First, a comparison is made of diesel and biodiesel combustion under identical engine operational parameters. Next, a detailed assessment of mixture stoichiometry near the flame lift-off length and its potential relation to emissions formation is pursued. The evaluation continues with a comparison of emissions behavior under normalized indicated mean effective pressure (IMEP) and start of combustion (SOC) timing conditions. Finally, fuel molecule structure effects on NO_x and heat release are considered.

The engine considered in this chapter is Engine 2, a single cylinder version of a Caterpillar 3406 diesel engine at the University of Wisconsin Engine Research Center [59, 60]. Engine specifications are given in Table 3.1, and the baseline scenario is defined as 80 % load at 1600 rpm.

4.2. BASELINE IDENTICAL OPERATING CONDITIONS

In this section, the overall effects of fueling with biodiesel on heat release rate, pressure, evaporation, entrainment, and spray characteristics are evaluated. The only modifications relative to the diesel inputs are to select the biodiesel physical properties relations and the biodiesel surrogate species introduced into the gas phase as a result of droplet evaporation. For conventional diesel, droplets evaporate entirely into n-heptane molecules in the gas phase to represent the chemical kinetics, while for biodiesel, a 50/25/25 percent blend of n-heptane, methyl decanoate, and methyl-9-decenoate is used [74].

Table 4.1 shows a comparison of key metrics of overall engine performance. As expected, the lower heating value of biodiesel (~ 37700 J/g) compared with diesel (~ 42900 J/g) results in about an 11 % reduction in both IMEP and thermal efficiency for biodiesel.

The experimental apparent heat release rate (AHRR) data shown in Fig. 4.1 is extracted from the pressure trace using Eqn. 4.1 using a ratio of specific heats γ given by a simple correlation as a function of temperature (Eqn. 4.2) [25]. The model-predicted AHRR is also calculated in the same way for the purposes of comparing heat release predictions.

$$(4.1) \quad \frac{dQ}{d\theta} = \frac{\gamma}{\gamma - 1} P \frac{dV}{d\theta} + \frac{1}{\gamma - 1} V \frac{dP}{d\theta}$$

$$(4.2) \quad \gamma = 1.338 - 6.0 \times 10^{-5}T + 1.0 \times 10^{-8}T^2$$

Although the model appears to underpredict peak heat release in the premixed burn phase, the shape, timing, and diffusion burn magnitude match well between experimental and modeled heat release rate for conventional diesel fuel (Fig. 4.1). Injecting biodiesel delays ignition and leads to a slightly higher peak heat release rate in the premixed burn phase. This is consistent with longer evaporation times for biodiesel due to the significantly lower vapor pressure. The slope of the diffusion burn phase heat release rate is lower for biodiesel, and the overall combustion time for both phases appears to be slightly shorter. This is consistent with other works that report shorter overall combustion times due to generally faster kinetics of biodiesel [92].

Fig. 4.3 shows instantaneous cylinder mass fractions of liquid, vapor, and combustion products, and the longer evaporation time for biodiesel is clearly evident. This delays the

onset of combustion, and so more of the biodiesel burns later in the cycle after TDC resulting in slightly lower pressures (Fig. 4.2) and temperatures (Fig. 4.4).

TABLE 4.1. Cycle simulation metrics for diesel and biodiesel.

Metric	Diesel	Biodiesel	Units
IMEP	11.1	9.9	bar
P_{\max}	96.0	91.8	bar
T_{\max} (average)	1494	1427	Kelvin
T_{\max} (local)	2961	2864	Kelvin
Injected fuel	92.1	104.7	mg
Q_{evap}	-108.5	-145.7	Joules
isfc	122.5	156.6	g/kWh
NO_x	28.0	20.3	g/kWh
Soot	0.0091	0.0125	g/kWh
Efficiency	68.5	61.2	%

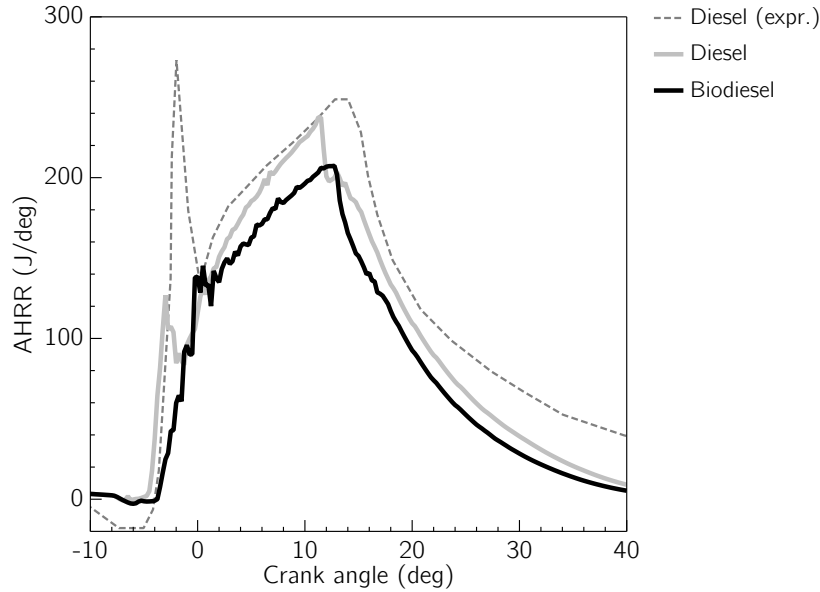


FIGURE 4.1. Comparison of diesel and biodiesel apparent heat release rates.

Lower pressures and temperatures for biodiesel also lead to lower NO_x and slightly higher soot levels relative to diesel when normalized by indicated work. The simple two-equation soot model, however, is likely inadequate to accurately predict soot formation for oxygenated fuels because it is primarily thermally driven and does not consider multiple precursor species

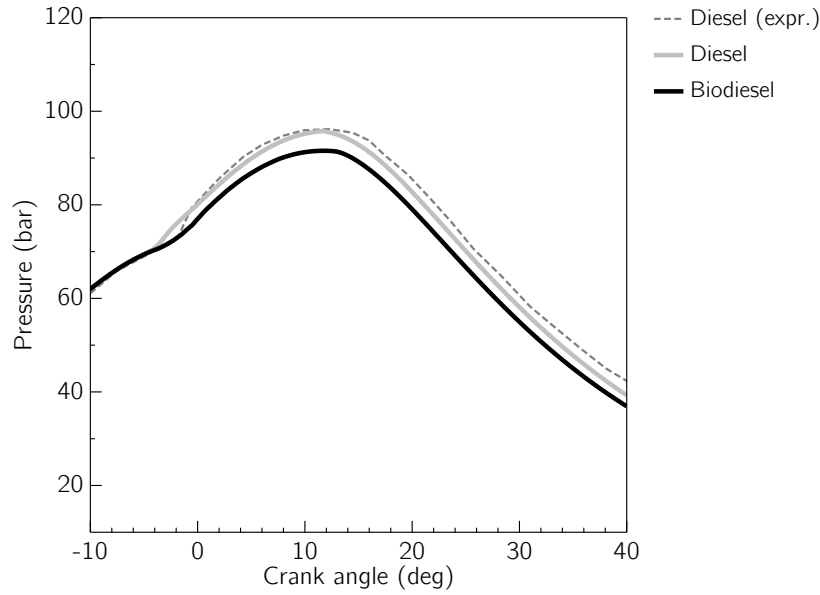


FIGURE 4.2. Comparison of diesel and biodiesel pressure traces.

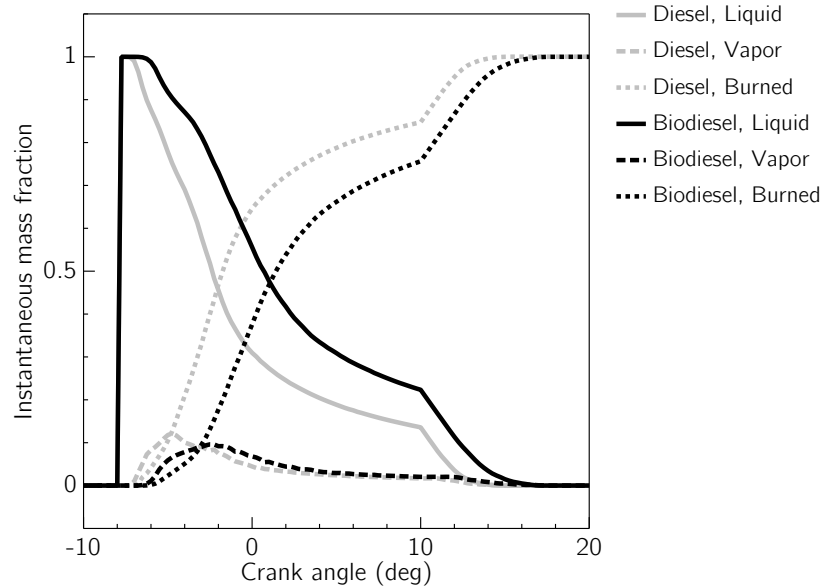


FIGURE 4.3. Comparison of diesel and biodiesel mass fractions of liquid, vapor, and burned fuel.

and different particulate nucleation pathways that may be different biodiesel. A more sophisticated soot model is probably necessary for predictive modeling of soot. Despite such deficiencies, soot modeling is still necessary to estimate local radiative heat transfer from

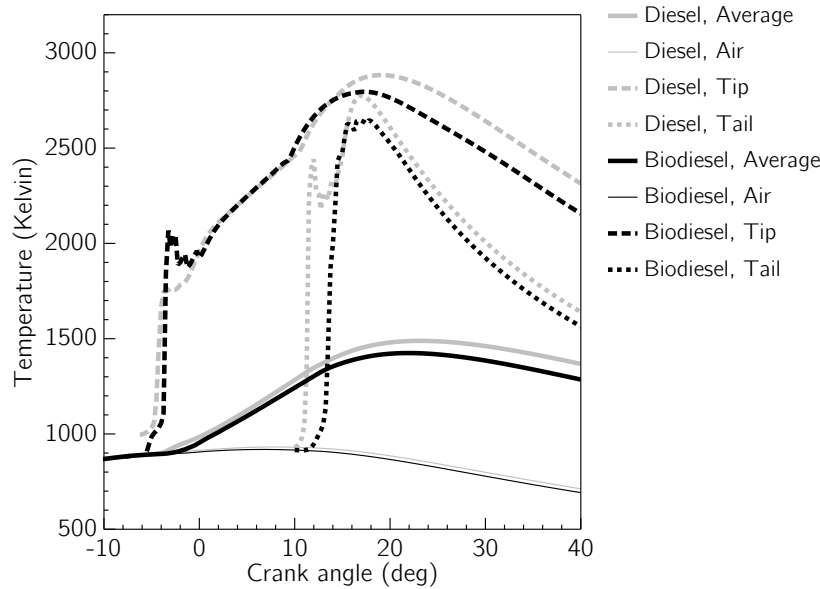


FIGURE 4.4. Comparison of diesel and biodiesel temperatures.

particulates due to the possible connection to NO_x formation. Several works have suggested that lower soot formation from oxygenated biodiesel fuels could be a contributing factor to increased NO_x by raising local temperatures [63, 80], even though other research has called into question this hypothesis as a primary cause [92].

Fig. 4.5 shows the evolution of NO_x and soot in the cylinder. Biodiesel shows lower absolute levels of soot formation throughout the cycle, even though the final value at the end of the cycle is slightly higher than diesel when normalized against indicated work (Table 4.1). Absolute levels of NO_x mass are also lower for biodiesel throughout the cycle, and remain about 27 % lower when normalized by indicated cycle work. Although this would appear to contradict the prevailing sentiment in the literature that suggests slight to moderate increases in NO_x with biodiesel, the baseline results here probably cannot be extrapolated to other operational conditions. Both experimental [79] and CFD modeling with biodiesel [74] have also shown reductions in NO_x for biodiesel under specific conditions.

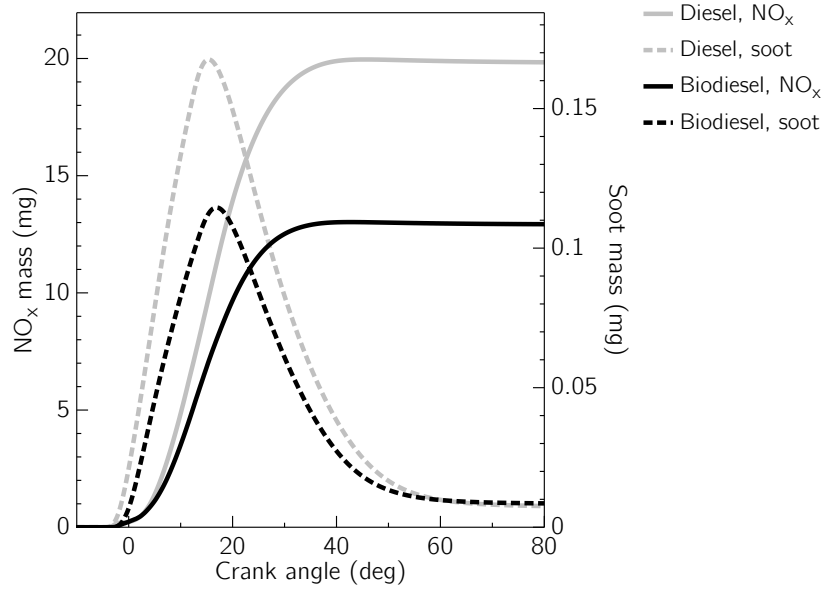


FIGURE 4.5. Comparison of diesel and biodiesel pollutant emissions.

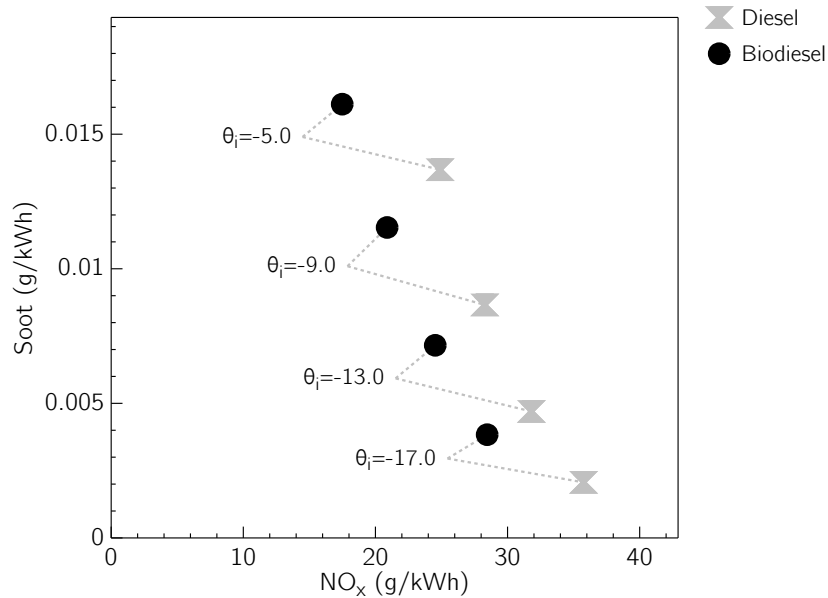


FIGURE 4.6. Comparison of diesel and biodiesel soot-NO_x tradeoff curve with varying start of injection timing.

Soot and NO_x predictions at various injection timings are shown in Fig. 4.6 for both fuel types. The classic soot-NO_x trade-off is evident, with the biodiesel exhibiting consistently lower NO_x and slightly higher soot relative to diesel in this scenario.

4.3. BIODIESEL SPRAY STRUCTURE

In this section, differences in spray structure are evaluated at the baseline condition, retaining identical operational parameters for the engine. Fig. 4.7 compares the liquid fuel mass fractions within the spray. Conventional diesel evaporates more quickly resulting in a shorter liquid length. Observed next to the temperature distribution (Fig. 4.8), it appears that for biodiesel, the hottest portions of the spray are immediately downstream of the last remaining liquid and distributed about the periphery of the spray that has entrained the most air. This indicates that the gas phase residence time of fuel molecules prior to combustion is shorter, and corresponds to the faster kinetics of long chain methyl esters in biodiesel.

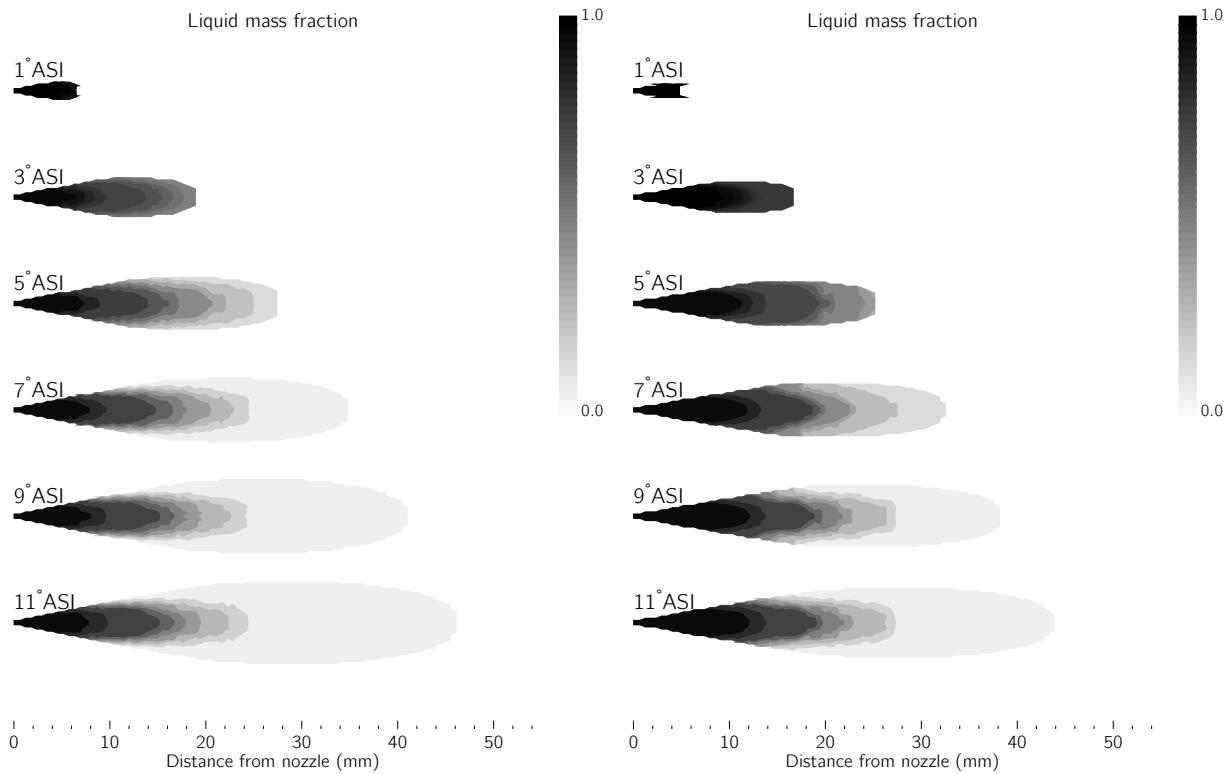


FIGURE 4.7. Comparison of diesel (left) and biodiesel (right) spray liquid lengths.

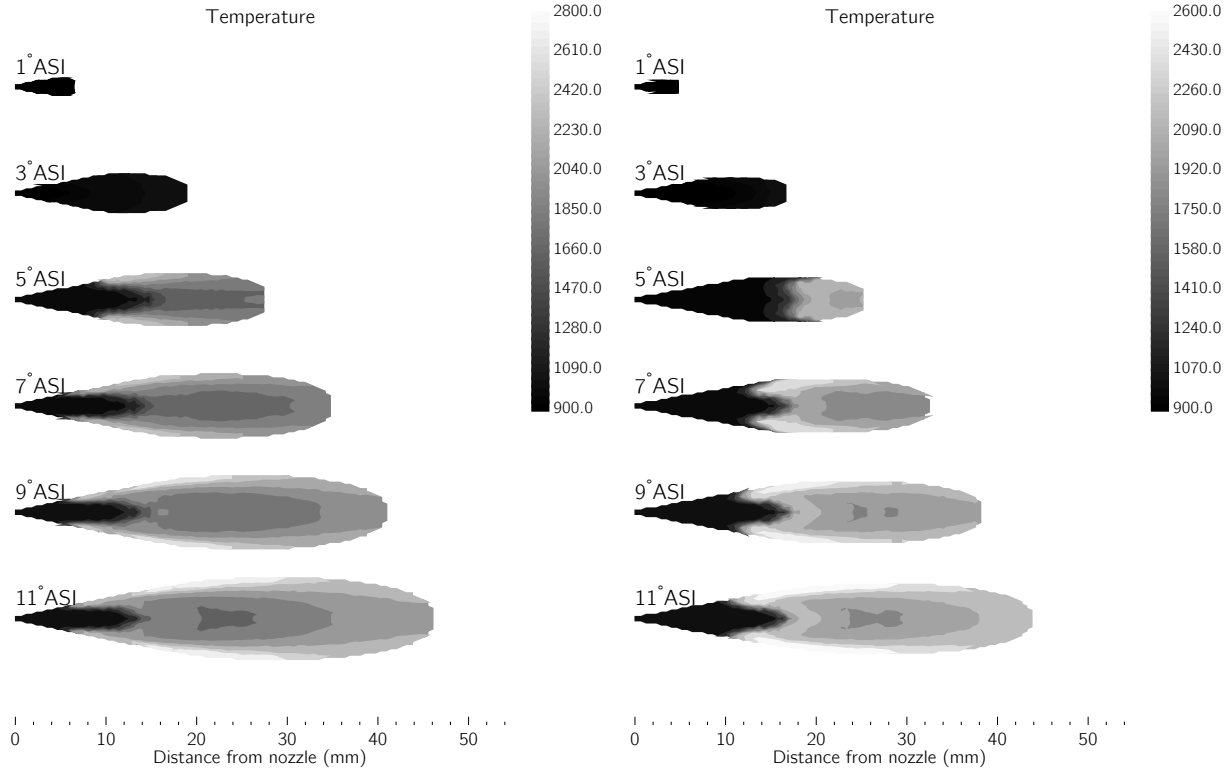


FIGURE 4.8. Comparison of diesel (left) and biodiesel (right) temperature distributions.

Normalized soot and NO_x mass distributions are shown in Figs. 4.9-4.10. For both diesel and biodiesel, NO_x formation occurs primarily about the periphery of the spray envelope at the hot diffusion flame boundary. Consistent with the temperature data and lift-off length, biodiesel NO_x formation appears further downstream and occupies a wider band around the spray edge compared with conventional diesel. Soot formation occurs in the interior of the spray, where temperatures are more moderate (1000-2000 K), and appears earlier and further upstream in the diesel spray. However, these observations should be taken as rough indications due to the inherent limitations of the soot model, as discussed previously. Nonetheless, the 2D visualizations offer useful confirmation that the general behavior of modeled emissions processes are consistent with the differences between the two fuels.

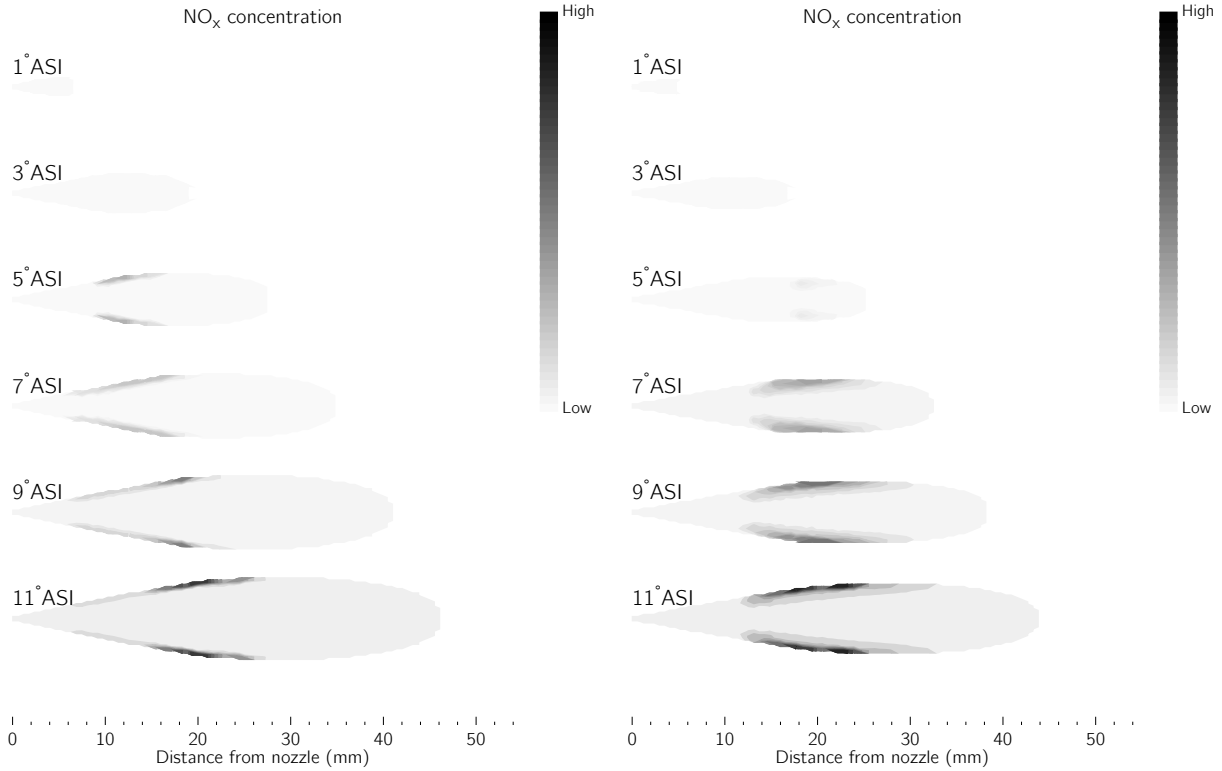


FIGURE 4.9. Comparison of diesel (left) and biodiesel (right) normalized NO_x distributions.

Fig. 4.11 shows the estimated liquid lengths of diesel and biodiesel as a function of crank angle. The plotted value is the furthest distance from the injector nozzle at which the liquid mass fraction is 0.1 or less. The liquid length of biodiesel is about 25 % longer than diesel, but both experience a slight shortening as combustion starts due to the higher cylinder temperatures and more rapid vaporization.

4.4. STOICHIOMETRY AT THE LIFT-OFF LENGTH

A comparison of flame lift-off lengths as a function of crank angle is shown in Fig. 4.12. The lift-off length is calculated as the nearest position to the injector nozzle at which the mass fraction of the hydroxyl (OH) radical is greater than 0.1 %. This method is generally consistent with the experimental OH-chemiluminescence imaging approach used in [92] to determine the flame lift-off length, as the presence of OH indicates strong combustion activity.

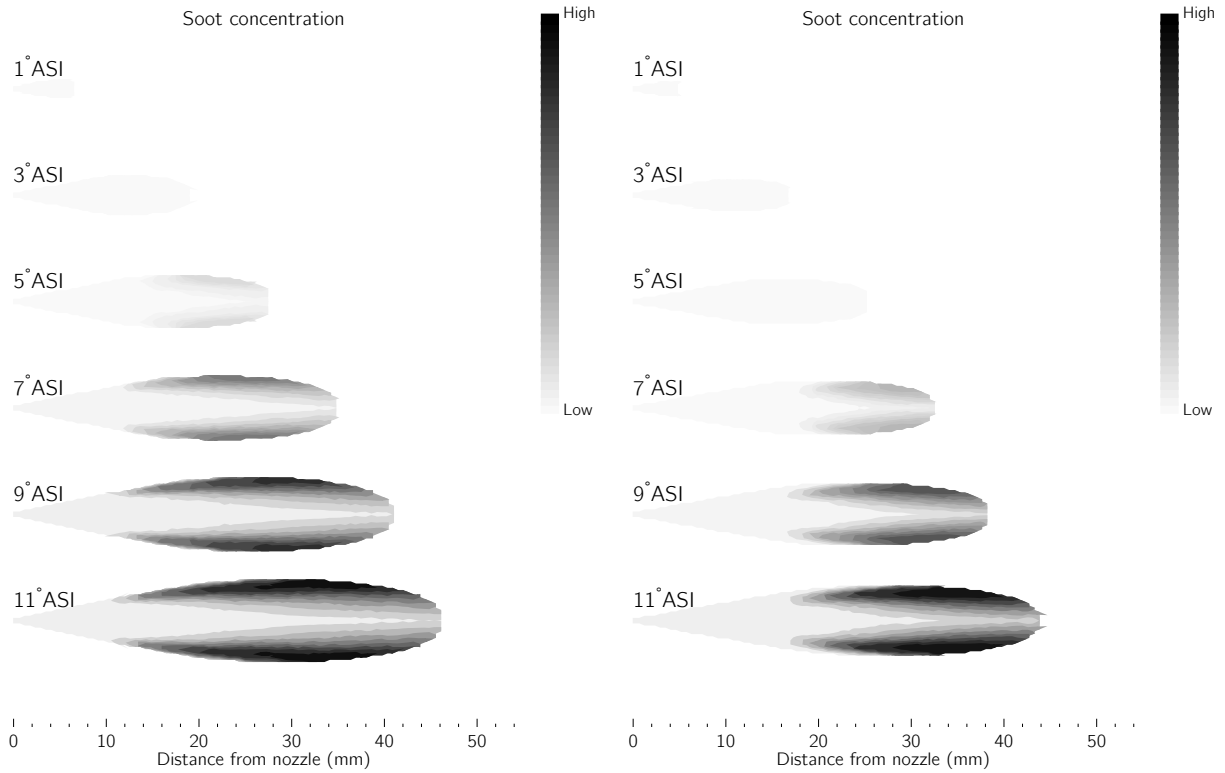


FIGURE 4.10. Comparison of diesel (left) and biodiesel (right) normalized soot distributions.

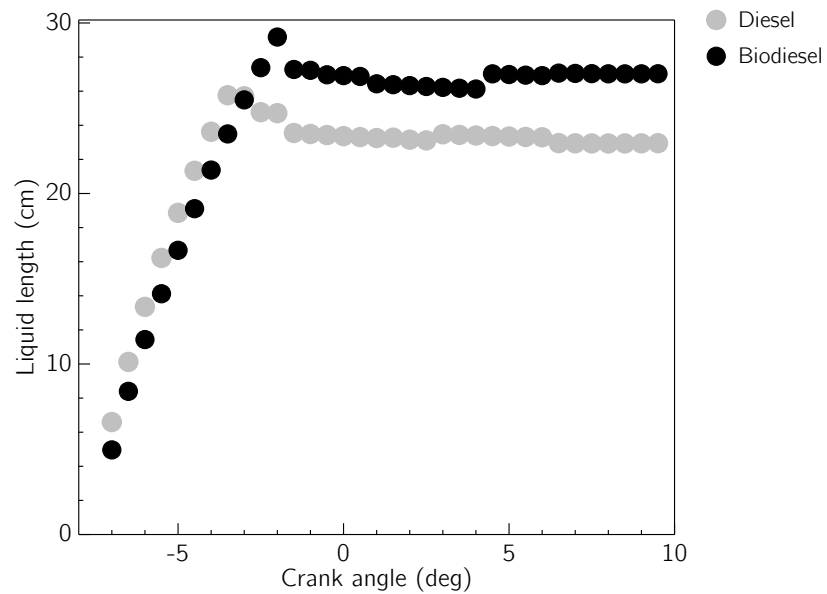


FIGURE 4.11. Comparison of diesel and biodiesel liquid lengths.

The flame lift-off for biodiesel is about 55 % further from the injector after the initial transient during which the ignition onset location shortens considerably and then stabilizes [93, 57].

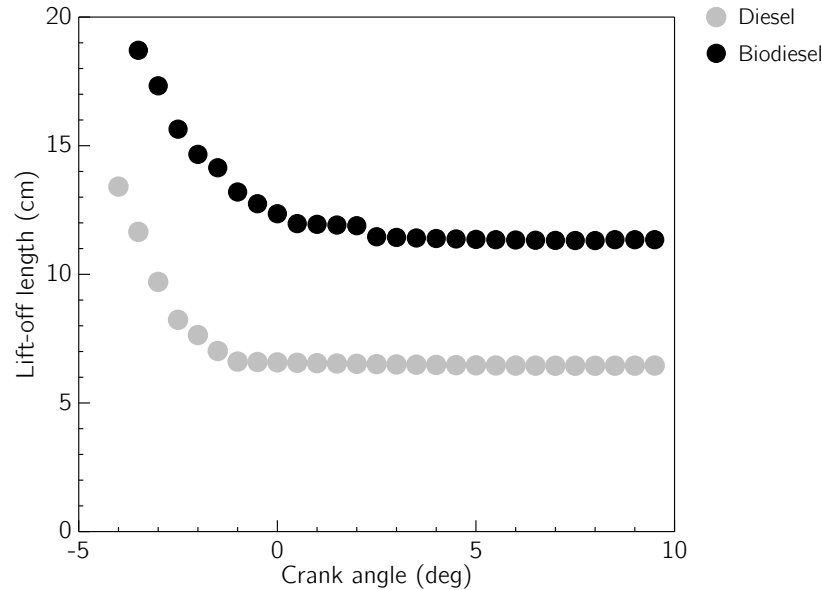


FIGURE 4.12. Comparison of diesel and biodiesel flame lift-off lengths.

Mueller and colleagues investigated mixture stoichiometry near the lift-off length in the course of their experimental investigation of the causes of biodiesel NO_x increases [92]. They found from a combination of 1-D jet modeling and experimental observations that increases in NO_x emissions were strongly correlated with mixtures closer to stoichiometric in the flame onset region. Stoichiometric mixtures burn hotter than lean or rich mixtures, and the convection of these high temperature combustion products downstream into the spray could be responsible for promoting thermal NO_x formation. Normalizing for start of combustion and IMEP, and choosing a relatively slow engine speed of 800 rpm, they found through a combination of 1-D jet modeling and experimental observations that biodiesel fuel-air mixtures were closer to stoichiometric (accounting for fuel-bound oxygen) near the lift-off length and were consistent with observed higher levels of NO_x .

In Fig. 4.13, the spray cross-sectional mass-weighted average equivalence ratio at the lift-off length is shown for diesel and biodiesel. Both gas phase instantaneous and total values are shown. The instantaneous equivalence ratio includes only vapor phase fuel molecules that are available for combustion, while the total value also includes liquid fuel that has yet to evaporate. Unlike Mueller’s findings, the instantaneous gas phase equivalence ratio for diesel appears to be closer to stoichiometric compared with biodiesel. If one looks at the total equivalence ratio, on the other hand, the biodiesel case is indeed closer to stoichiometric at the liftoff length, as reported by Mueller. However, it seems that the instantaneous equivalence ratio is the proper one to evaluate because it represents the state of the combustible gas mixture. The leaner biodiesel mixture would result in lower flame temperatures and thus lower NO_x initiated from the flame onset region.

Thus, the modeling results here are in line with the concept of flame lift-off length stoichiometry being correlated with NO_x emissions, but for these engine conditions, diesel results in closer to stoichiometric gas phase conditions and thus higher NO_x . Clearly, this is a complex thicket of interactions and not one single reason can explain the emissions behaviors of biodiesel in all cases. In the next sections, flame lift-off stoichiometry and NO_x emissions will be evaluated at both normalized operational conditions and different engine speeds.

4.5. COMPARISONS UNDER NORMALIZED OPERATING CONDITIONS

In §4.2-§4.4, comparisons of diesel and biodiesel fueling occurred under identical operational parameters. However, it is difficult to compare key metrics and emissions processes “apples-to-apples” due inherent differences in total fuel injected, combustion phasing, and indicated engine work. This section attempts to normalize conditions to the same start of combustion timing and IMEP.

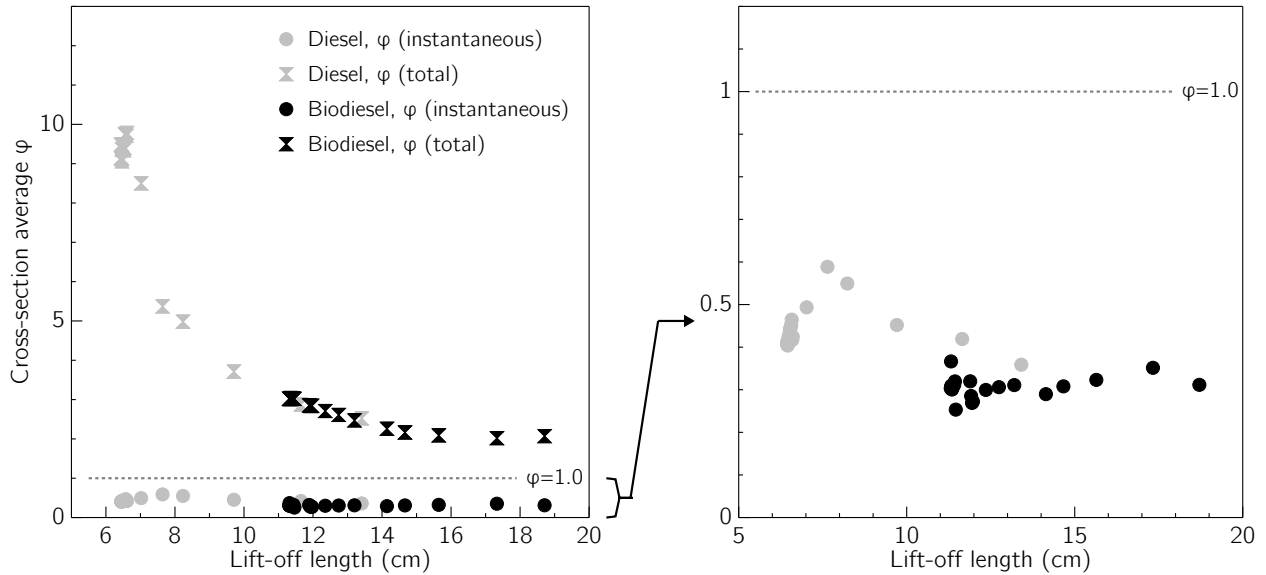


FIGURE 4.13. Instantaneous equivalence ratio at the flame lift-off length, mass-weighted cross-sectional average.

Starting with the baseline engine parameters, the injection timing was manually varied for diesel and biodiesel to achieve the same start of combustion (SOC), here defined as the crank angle at which $+10$ J/deg apparent heat release rate is reached. With a nominal injection timing of -8° , $+10$ J/deg AHRR occurred at -4.5° with diesel fuel. For biodiesel, the injection was retarded to -9.25° for the same SOC. For both cases, injection durations of 3, 6, and 9 degrees were evaluated, each at engine speeds of 700, 1100, and 1500 rpm. Fig. 4.14 shows relative NO_x emissions compared to diesel at various mean pressures and engine speeds. In all cases, the biodiesel fuel yields lower NO_x , but at slow engine speeds, the reduction is smaller. This is consistent with other research that shows a higher NO_x penalty at low engine speeds [90], even though in the scenarios considered in that work, biodiesel did in fact produce lower NO_x .

The lower NO_x observed for biodiesel correlates with slightly lower peak in-cylinder temperatures (Fig. 4.15). It is also supported by the flame lift-off length stoichiometry hypothesis

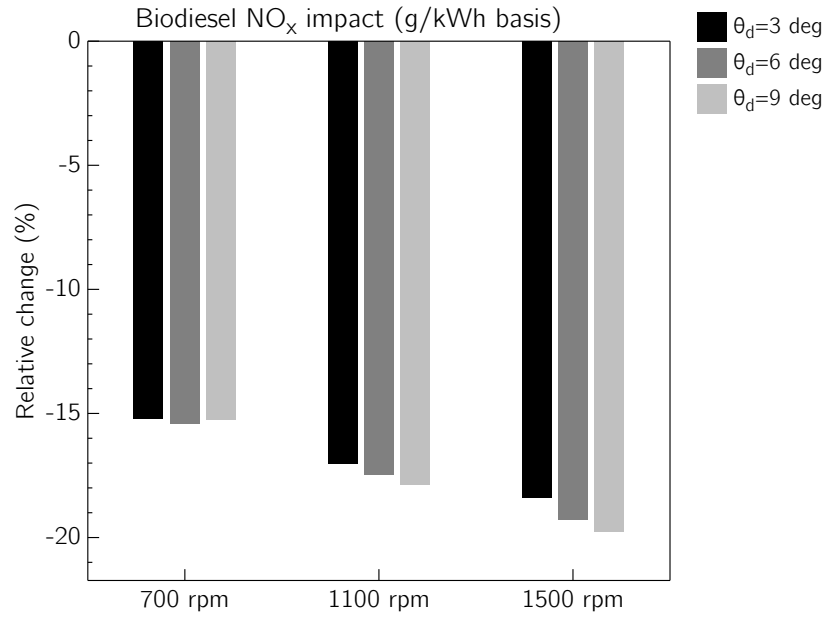


FIGURE 4.14. Relative NO_x emissions change of biodiesel compared to diesel at various IMEPs and engine speeds.

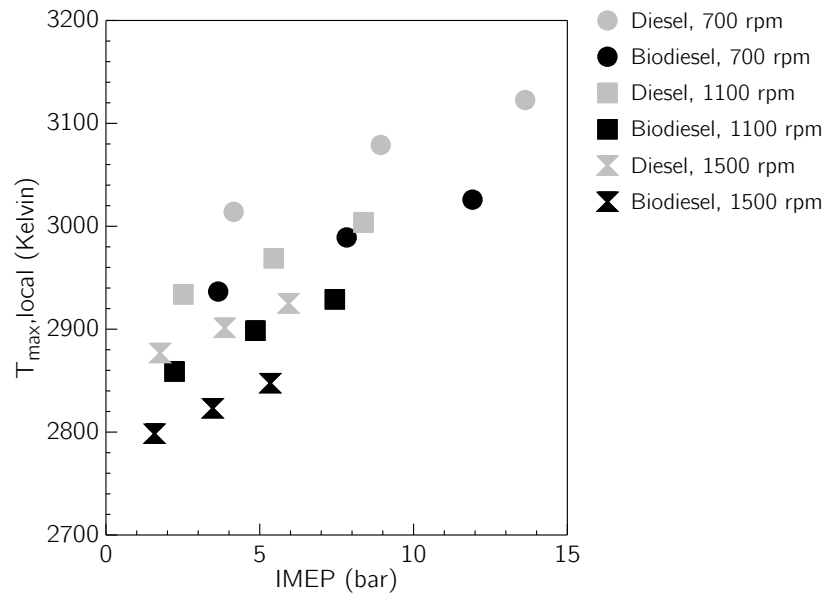


FIGURE 4.15. Local peak temperatures at various IMEPs and engine speeds.

described in the previous section. Fig. 4.16 shows the mass-weighted cross-sectional average

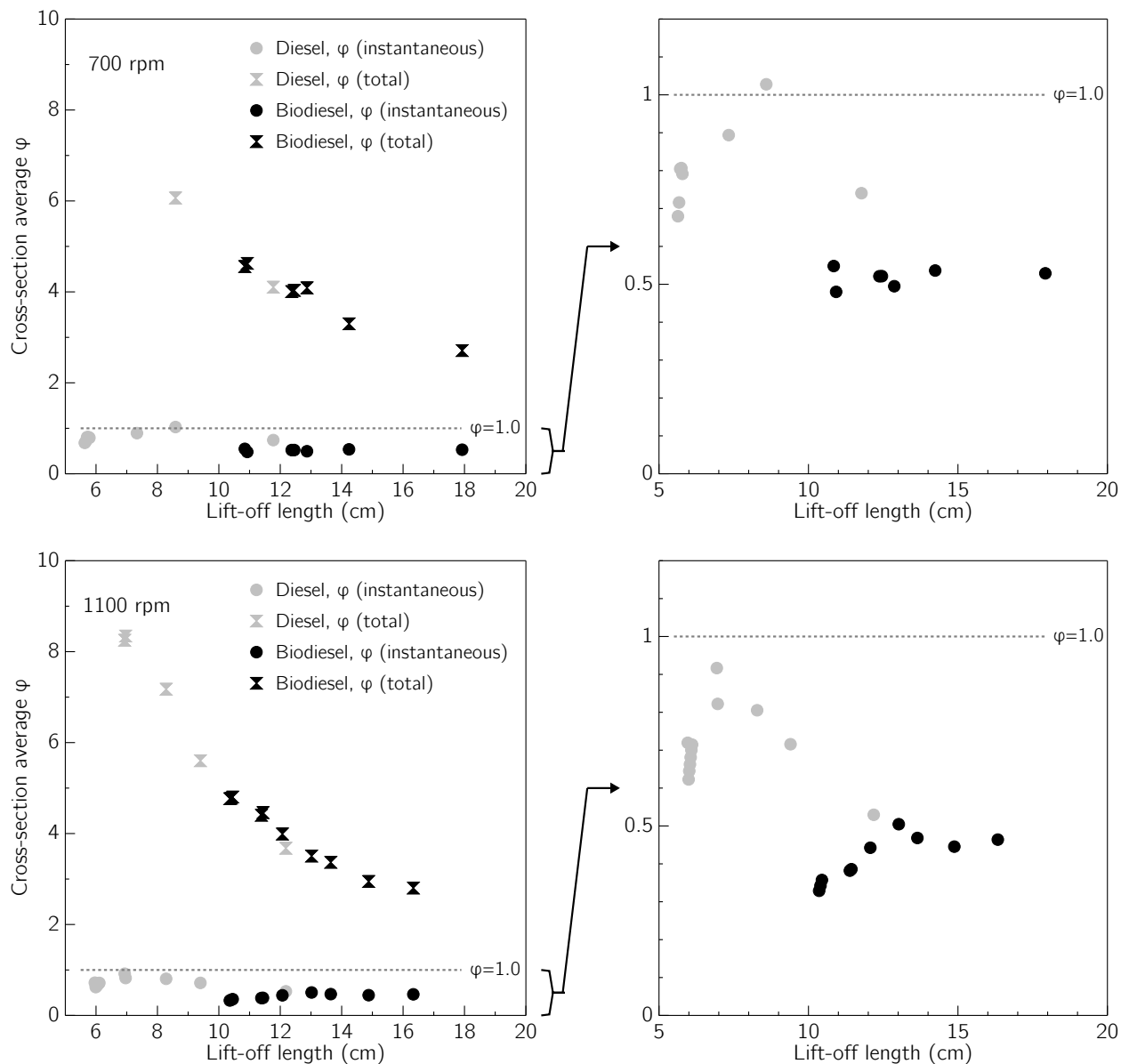


FIGURE 4.16. Stoichiometry at the lift-off length at (a) 700 rpm, and (b) 1100 rpm. Both at IMEP \approx 8 bar.

equivalence ratio at both 700 and 1100 rpm engine speeds. Again, the gas phase instantaneous equivalence ratios are closer to stoichiometric at the lift-off length for conventional diesel which would elevate local temperatures and lead to higher NO_x .

Although temperatures and stoichiometry are consistent with NO_x trends, relative changes in particulates (Fig. 4.17) do not show a clear pattern. If it were the case that NO_x formation

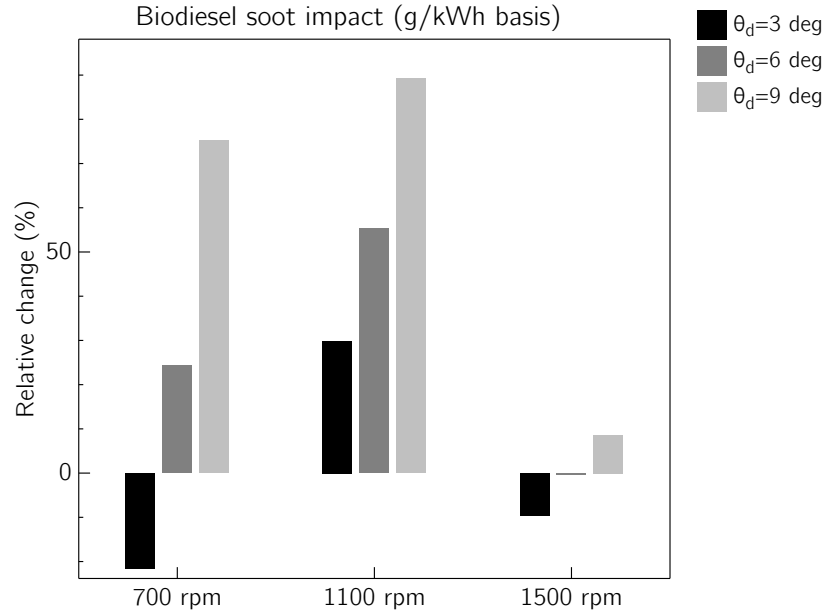


FIGURE 4.17. Relative soot emissions change of biodiesel compared to diesel at various IMEPs and engine speeds.

in biodiesel-fueled engines was only driven by thermal effects, one would expect the classical soot- NO_x tradeoff to be apparent in these results. That is, consistently lower NO_x ought to be paralleled by consistently higher soot (and vice versa) at various loads and engine speeds. With that not being in evidence here, and the limitations of the soot model notwithstanding, other factors such as fuel molecular structure and the particulars of combustion pathways may be at play, and will be explored next.

4.6. FUEL MOLECULAR STRUCTURE EFFECTS

To gain further insight into the effects of biodiesel fuel molecule structure on emissions formation, the blending of n-heptane, methyl decanoate (md), and methyl-9-decenoate (md9d) surrogates in the chemical kinetic mechanism was varied. McCormick and colleagues reported experimental results in [94] showing greater NO_x formation correlated with increasing iodine number for various methyl ester fuels. Iodine number is a measure of unsaturation in

hydrocarbon molecules, with higher iodine numbers indicating more carbon-carbon double bonds in the chain. Biodiesel cetane number has also been shown to negatively correlate with iodine number, with saturated fuels (low iodine number) exhibiting shorter ignition delays (high cetane number) [94]. Depending on fuel injection timing and engine speed, these aspects of fuel molecular structure may either increase or decrease NO_x emissions. In general, McCormick concluded that the molecular structure is a key contributor to the NO_x behavior of various biodiesels, although subsequent work by the same authors indicated that increased cetane number alone did not produce higher NO_x [95].

To explore molecular structure effects in this model, the fuel unsaturation was modified by mixing various blends of methyl decanoate and methyl-9-decenoate. Predicted NO_x is shown in Fig. 4.18, at both 1000 and 2000 rpm. Injection timing was fixed in all cases to -5° BTC, and a relatively short 5° injection duration was selected. The low loads of roughly 3.5 and 1.2 bar IMEP help establish more controlled conditions to evaluate fuel chemistry than higher loads at which other factors affecting combustion progress, such as fuel mixing and wall impingement, may come into play.

Blends representing fuels with a higher degree of unsaturation tends to increase NO_x , corroborating the experimental data of [94] and [96]. At 2000 rpm, fueling with pure methyl-9-decenoate leads to a roughly 25 % increase in NO_x over pure methyl decanoate. For the slower engine speed, NO_x seems to peak at a 50 % blend, although the reason for this is not immediately evident. The fact that the local peak and cylinder average temperatures do not track with the increase in NO_x with greater unsaturation seems to suggest the important role of molecular structure on influencing different chemical combustion pathways that could yield different levels of NO_x .

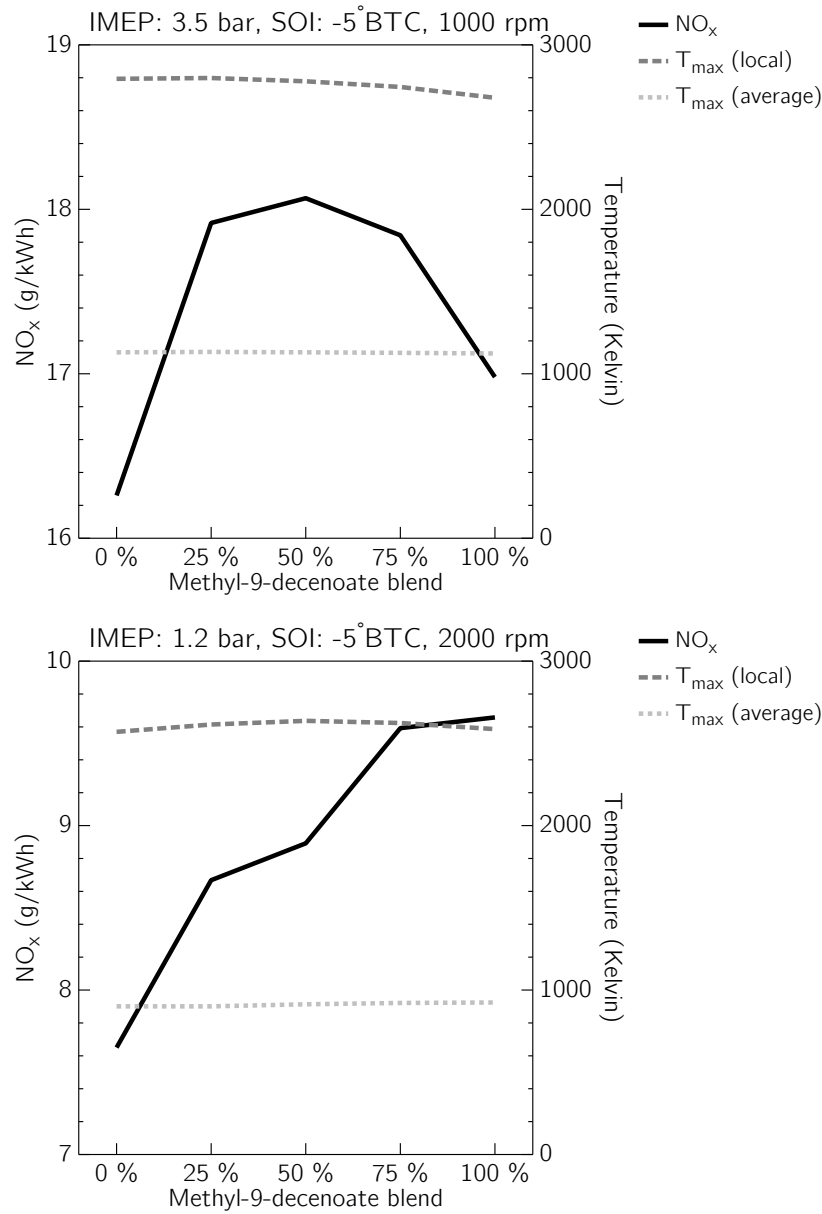


FIGURE 4.18. Impact of fuel molecular structure on NO_x and peak temperatures at different engine speeds.

Plotting the apparent heat release rate for 0 %, 50 %, and 100 % blends at both speeds (Fig. 4.19) offers some more information. At 1000 rpm, the peak heat release rate is much higher and much more of the fuel appears to burn in the premixed phase. The fully saturated methyl decanoate exhibits the longest ignition delay, pushing combustion later into the cycle thereby lowering temperatures and NO_x, even though the peak temperatures achieved remain

relatively unchanged. There is not much qualitative difference between the 50 % and 100 % blends as it appears that the mere presence of unsaturated fuel molecules dominates the overall ignition delay. Unfortunately, this also does not really help explain the peaking of NO_x at the 50 % blend level, and the existence of alternative chemical pathways due to the fuel structure could be a possible explanation.

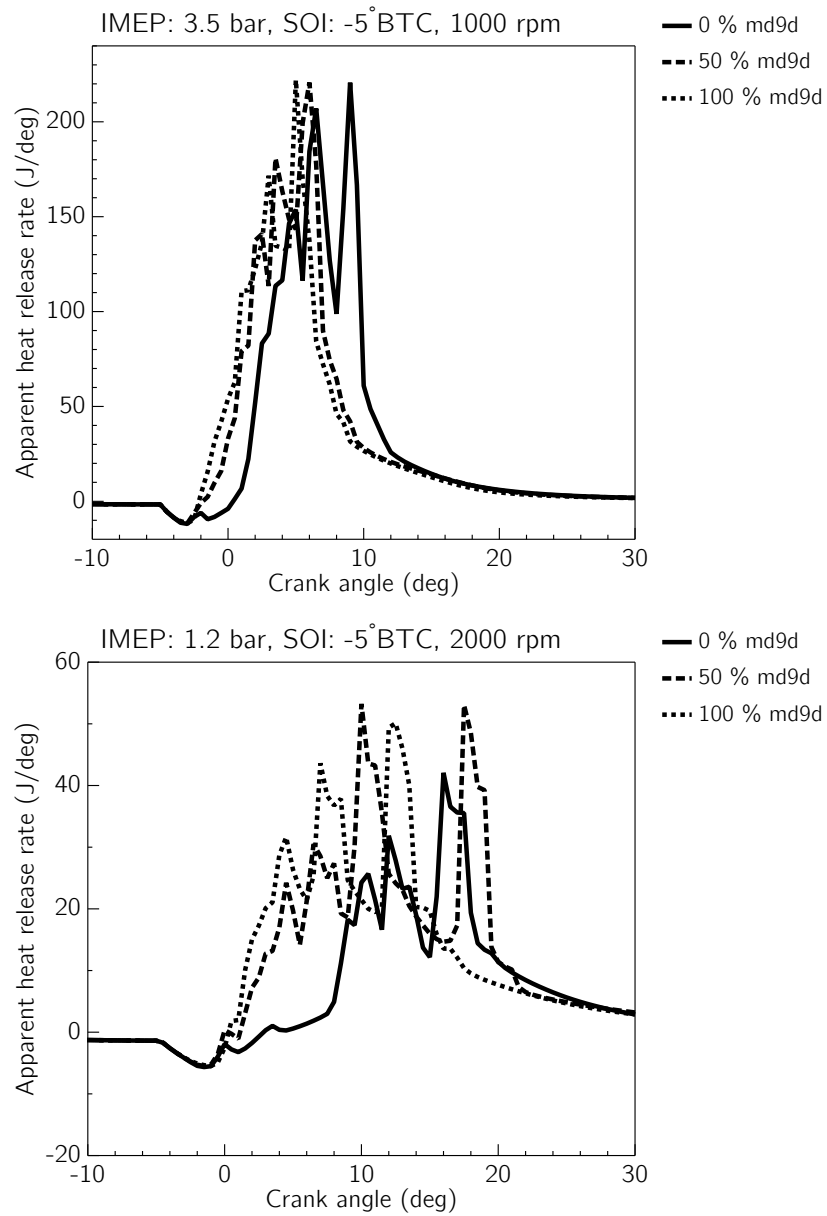


FIGURE 4.19. Impact of fuel molecular structure on apparent heat release rate shape at different engine speeds.

The trend in ignition delay at 2000 rpm among the fuels is essentially the same, with unsaturated fuels igniting more quickly and combustion occurring closer to TDC at higher temperatures. The higher engine speed results in combustion occurring primarily in a diffusion flame later in the cycle, and so the increasing NO_x trend with iodine number can be generally accounted for from the heat release rate shape.

This analysis, however, seems to expose a few problems. First, the quality of combustion observed in Fig. 4.19 seems quite poor, and there is no good explanation for the irregular peaking of the heat release curve. Having demonstrated “good” heat release rate shapes in previous sections, one must conclude that the reduced biodiesel chemical kinetic mechanism is probably not adequate for predicting combustion behavior of pure methyl decanoate and methyl-9-decenoate blends, and that the inclusion of n-heptane for modeling soy biodiesels is a key ingredient for the overall combustion process. The irregularities in heat release might be explained by a loss of fidelity in kinetic modeling of intermediate species pathways from long chain molecules due to the highly reduced size of the chemical mechanism. Second, the modeled ignition delays for different blends appear to conflict with experimentally observed increases in cetane number for saturated fuels [94, 96]. That is, saturated methyl decanoate should ignite most quickly, but the opposite is predicted here, suggesting the need for more accurate kinetic mechanisms for biodiesel modeling. Third, the possible shortcomings of the reduced biodiesel kinetic mechanism would appear to undermine the accuracy of an attempt to include prompt NO_x chemistry to more holistically account for NO_x formation processes.

Finally, generalizations about NO_x behavior as a function of fuel molecular structure are very sensitive to engine operating conditions, particularly injection timing and speed. For example, suppose that fuel injection is advanced significantly. Then, the fuel with

longer ignition delay will burn closest to top center with the highest temperatures and NO_x production. Conversely, retarding fuel injection significantly would push combustion for the fuel with the longest ignition delay furthest into the cooler part of the cycle, resulting in lower temperatures and presumably NO_x . It could be that general observations about biodiesel NO_x penalties in the literature are more a result of commonly used engine operating conditions rather than a general rule about NO_x increasing as a sole consequence of using biodiesel. This could also help explain the variety of results reported from both experiment and modeling studies that show both increases and decreases in NO_x from biodiesels.

4.7. SUMMARY

This chapter applied the new quasidimensional spray model with detailed kinetics to investigate differences between diesel and biodiesel sprays. In general, biodiesel takes longer to evaporate and results in longer ignition delays. However, although multiple possible reasons for changes in NO_x emissions from biodiesel relative to diesel are difficult to disentangle, engine operating conditions, rather than one specific characteristic or difference in fuel chemistry, appear to be a primary cause.

CHAPTER 5

COMPUTATIONAL ROBUSTNESS AND EFFICIENCY

5.1. OVERVIEW

In this chapter, the model is evaluated to assess its sensitivity to discretization and spray mixing parameters. The aim is to better understand the consistency of predicted metrics under various numerical and modeling conditions. Baseline conditions for Engine 1 (Table 3.1) are used, with the primary reference fuel kinetic mechanism of Ra et al [66]. Computational scalability is also examined.

5.2. SENSITIVITY TO DISCRETIZATIONS

First, the behavior of the model as a function of simulation step size is evaluated. Fig. 5.1 shows NO_x , IMEP, local peak temperature, and thermal efficiency as a function of running the model with step sizes of 0.1, 0.25, and 0.5 crank angle degrees (CAD). In general, these key metrics do not change much as a function of step size. Of course, the simulation time is greatly increased for 0.1 CAD step case, since not only is the simulation step 5 times smaller than the largest, but there are also 5 times the number of thermodynamic zones since the model creates a new set for the spray at each step. Overall, the stability of key performance metrics is an encouraging result and shows that the model is fairly robust in its solution procedure.

The impact of simulation step on soot predictions is more complicated. As shown in Fig. 5.2, soot predictions are quite sensitive to the step size used, particularly when acetylene (C_2H_2) is used as the soot precursor molecule. With acetylene as the precursor, there is a nearly 400 % jump in predicted engine-out soot as the simulation step size is reduced

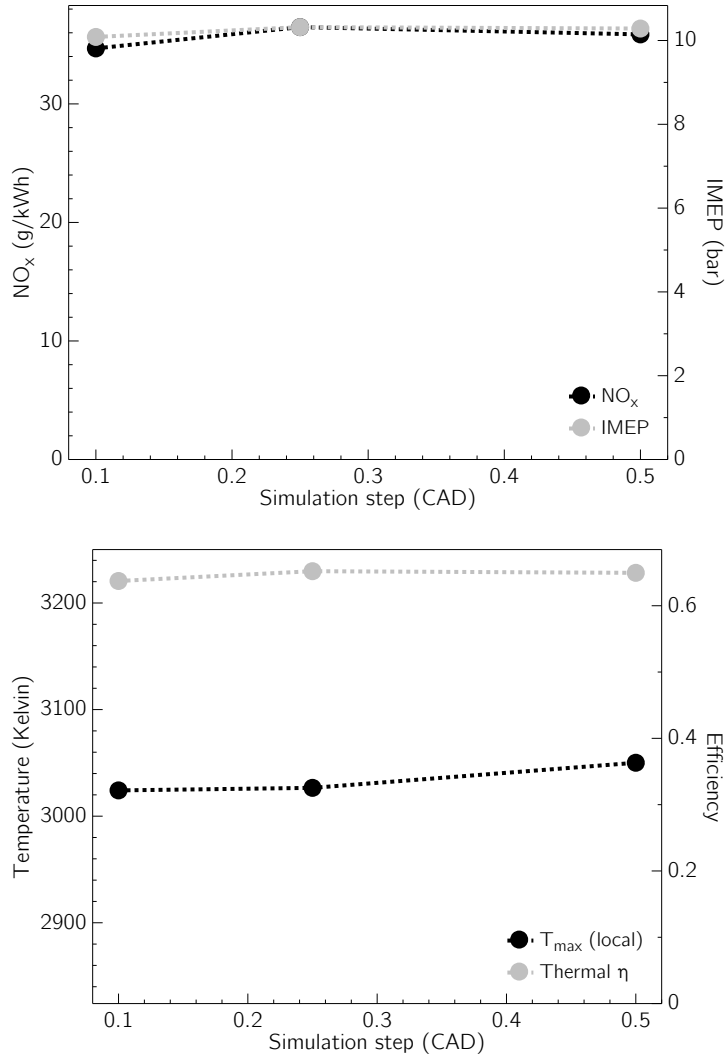


FIGURE 5.1. Effect of simulation step on key metrics.

from 0.5° to 0.1° . With all hydrocarbon molecules as possible precursors, the soot predictions are more stable, with the highest and lowest predictions across different step sizes begin only roughly 40 % different. The soot formation rate is directly dependent on the gas phase concentrations of the precursor species that are linearized source terms into the energy/transport equations from the chemistry solver (§2.15). If the precursor molecule is selected to be a highly transient intermediate such as acetylene (a common approach in other detailed models [61]), at large step sizes the concentration of acetylene is smeared out and

appears quite small, thereby reducing the soot formation rate. If all gas phase hydrocarbon species are possible soot precursors, then the aggregate concentration is less transient and so the soot predictions appear more stable. This result exposes the several weaknesses of the soot model and indicates a need for more sophisticated models to be developed and incorporated, ideally, directly into the gas phase chemical kinetic mechanism. That being as it may, best practice for using the two equation soot model is to use all gas phase hydrocarbons as precursors, and calibrate the leading coefficient of the soot formation equation (see Eqn. 2.93) to match experimental data. Then, even this simplistic model may offer some preliminary insights into trends and tradeoffs for soot, even if the absolute values must be calibrated.

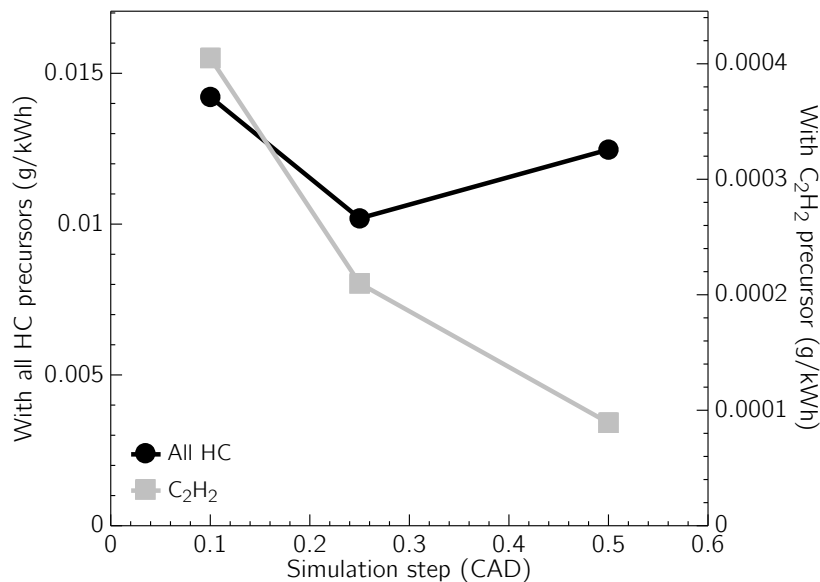


FIGURE 5.2. Sensitivity of soot predictions to step size and choice of precursor molecule.

Next, the sensitivity of outputs to the number of radial spray zones is shown in Fig. 5.3. NO_x shows a slight decrease as the number of zones increases from 5 to 15, but then largely stabilizes. Other metrics appear stable too. This result suggests that 10-15 radial zones are

likely sufficient to predict engine behavior reliably. The increase in simulation time is linear with the number of radial zones.

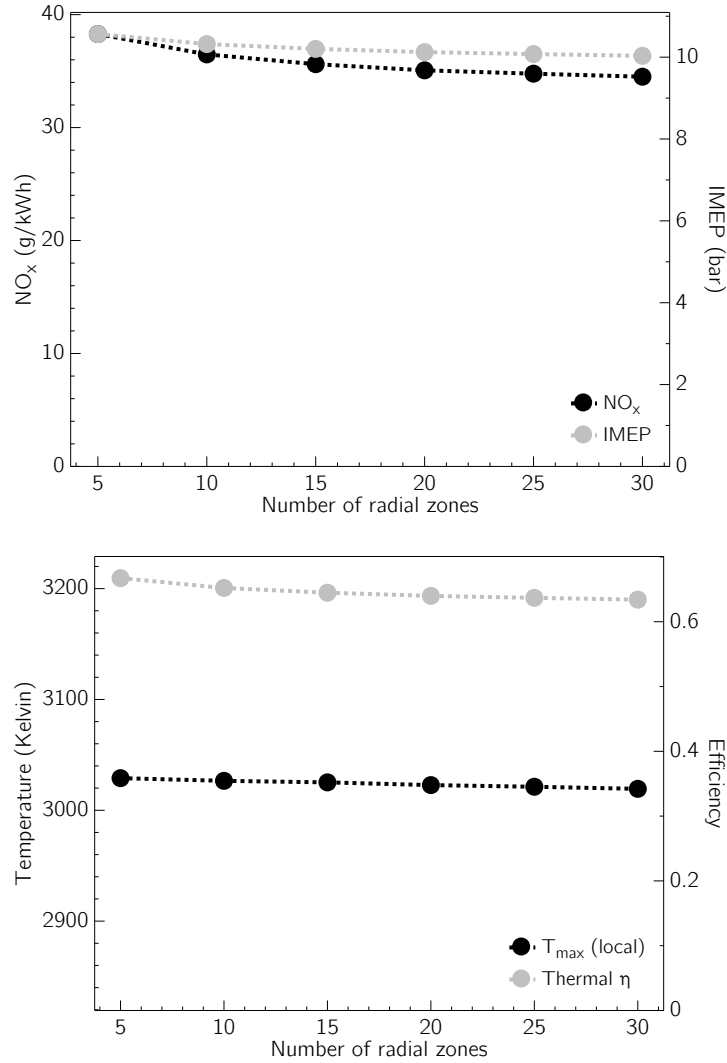


FIGURE 5.3. Effect of number of radial spray zones on key metrics.

5.3. SENSITIVITY TO MIXING AND ENTRAINMENT PARAMETERS

This section evaluates model predictions as a function of parcel mixing and spray entrainment parameters. First, the impact of the phenomenological parcel mixing model intensity

factor ζ_m described in §2.10 on NO_x , IMEP, temperature, and thermal efficiency is considered. Overall, good consistency among all metrics is observed, particularly when some parcel mixing is enabled. There is little impact of increasing the parcel mixing intensity beyond the default ζ_m parameter value of 1.0 on these four metrics.

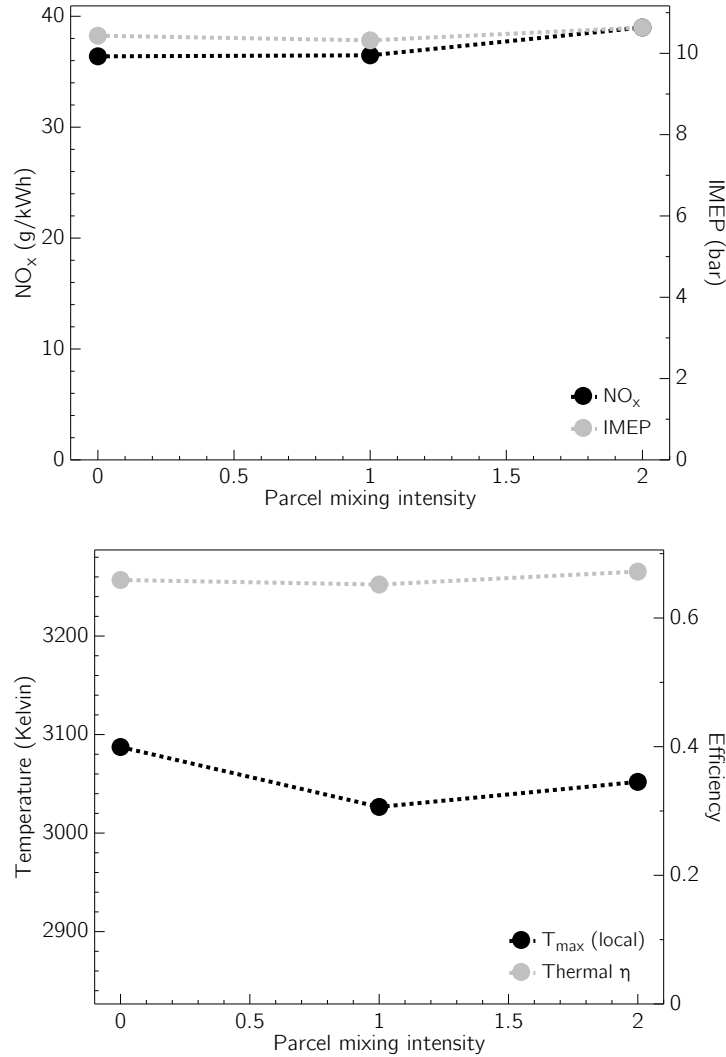


FIGURE 5.4. NO_x , IMEP, peak temperature, and thermal efficiency as a function of parcel mixing intensity factor.

As indicated previously in §3.5, disabling parcel mixing eliminates any apparent premixed burn phase in the heat release rate shape (Fig. 5.5). Intensifying parcel mixing beyond the

default level amplifies the peak premixed burn heat release slightly, but does not significantly alter the overall shape.

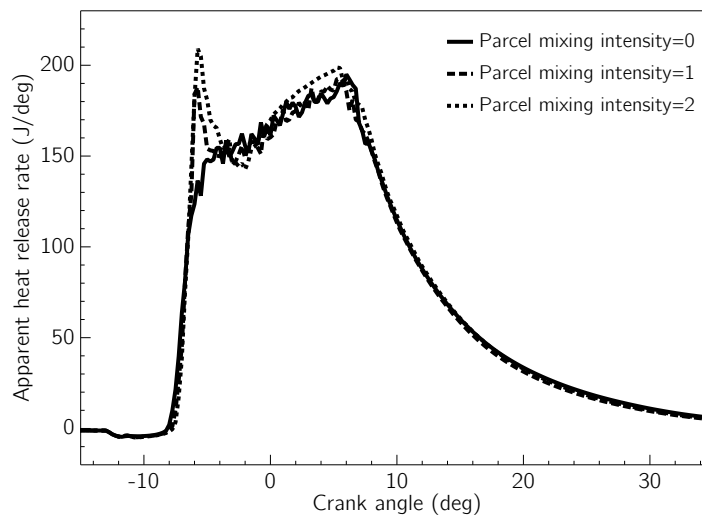


FIGURE 5.5. Comparison of heat release rate with different parcel mixing intensity factors.

Next, the effect of adjusting the the spray tip to parcel velocity constant K_u is assessed. A value of 1.0 is used by default in the simulations, although the gas jet analysis in §2.5 suggested that a value slightly greater than 1.0 might be appropriate. A value greater than one increases local parcel velocities and reduces the rate of entrainment, while a value less than 1 has the effect to increase entrainment rates into parcels.

In general, changing K_u has minimal impact on NO_x and IMEP predictions, and a small, but noticeable impact on peak temperature and thermal efficiency (Fig. 5.6). However, Fig. 5.7 shows that K_u has a pronounced impact on shape of the apparent heat release rate. Increasing K_u , and thereby slowing entrainment, reduces the peak premixed heat release, but largely preserves the distinction between premixed and diffusion burn phases. Also, the diffusion burn tail is more gradual. Further work is likely necessary to definitively say

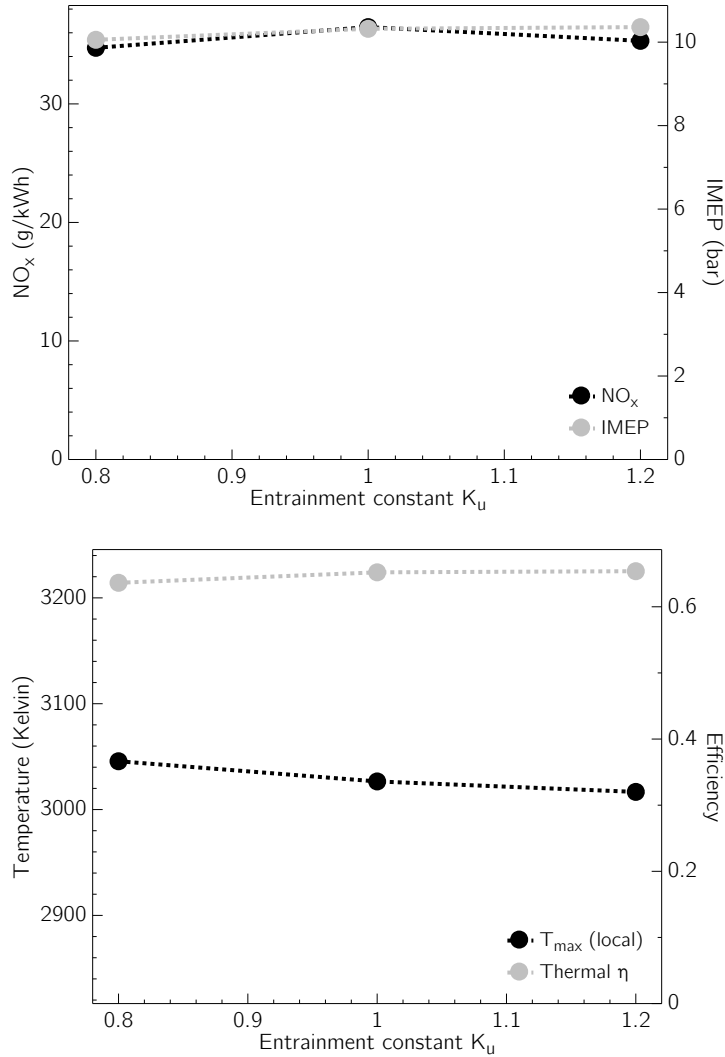


FIGURE 5.6. Effect of changing the entrainment constant K_u on key metrics.

what the proper value of K_u should be, although something in the 1-1.2 range appears fairly defensible both from an analytical and observed model behavior standpoint.

5.4. COMPUTATIONAL SCALABILITY

The scalability of the parallelized C++ implementation of the model is also briefly explored. Due to the decoupling between the chemical kinetics solver and the thermodynamic zone models (see §2.15), each zone's chemical kinetics can be advanced in time independently

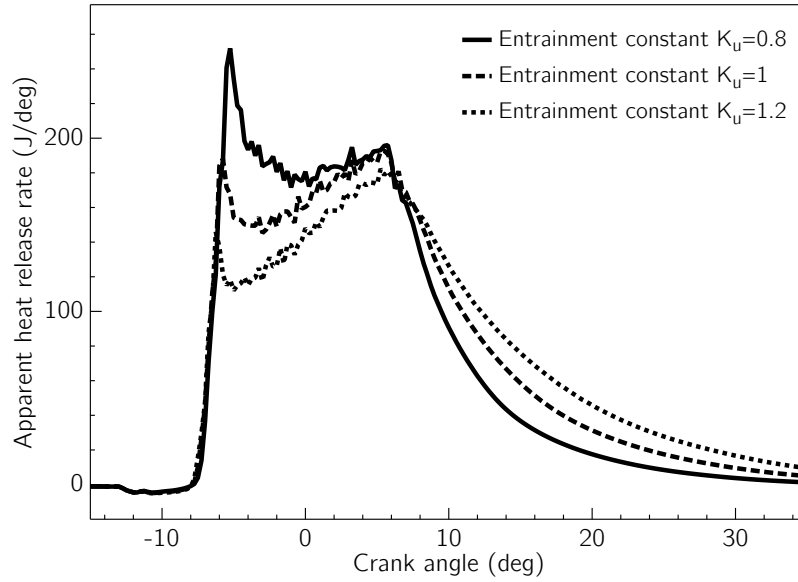


FIGURE 5.7. Effect of changing the entrainment constant K_u on heat release rate shape.

of one another within a single model step. This permits the chemical kinetic calculations to be done in parallel and more fully utilize available processor cores. The sequential portion of the code includes integration of the continuity, energy, spray, and droplet equations in time, which occurs in between the parallelized chemistry calculations.

The simulations in this work were conducted on an Intel i7-5820k 3.3 GHz 6-core processor. This high performance yet fairly affordable processor (\sim \\$400 USD in 2015) includes “hyperthreading” technology that essentially allows two computational threads to be channeled through a single core to maximize utilization of computational units within the core. As a result, the processor reports having 12 effective cores to the software environment. The effect of this hardware architecture is evident in Fig. 5.8. Significant speedups are observed up to 6 cores, after which increases in model performance largely plateau. In addition, the decrease in calculation time from 1 to 6 cores is not linear, as the overhead associated with

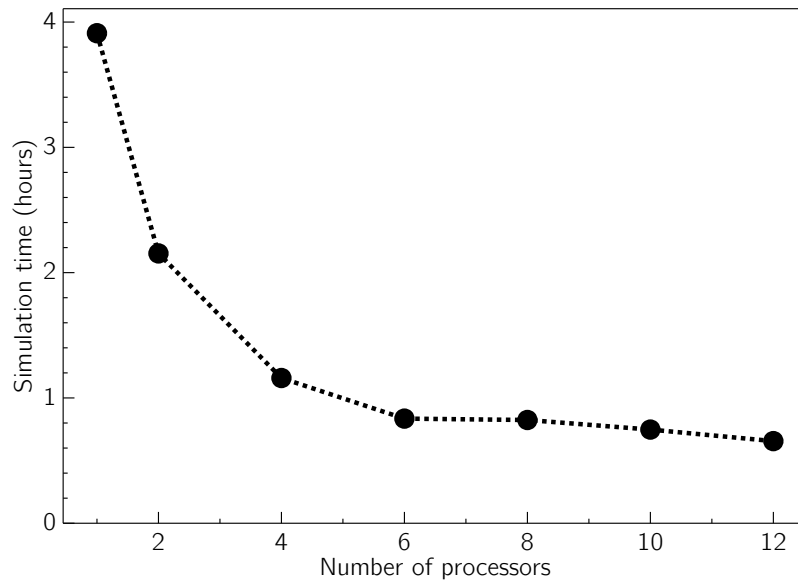


FIGURE 5.8. Scalability of decoupled parallel simulation procedure on an i7-5820k 6-core processor.

spawning parallel threads increases and the fraction of time spent in the sequential model code increases relative to total computation time.

The model achieves high average utilization ($\sim 95-99\%$) of the processor and is well suited for running on this type of commonly available desktop hardware. As a result, the overall computational cost, from both a time and capital expenditure perspective, seems very reasonable.

CHAPTER 6

CONCLUSIONS

The integration of detailed chemical kinetics into a quasidimensional diesel spray model framework shows promise for a computationally expedient and sufficiently predictive tool that can improve understanding of compression ignition engine combustion phenomena. Good prediction of cylinder pressure was obtained in all cases, as well as reasonable agreement in heat release rate. Since the model does not rely on empirical constants to calibrate burning rate to experimental data, a much greater burden is placed on the phenomenological spray parcel model to accurately predict local air entrainment, equivalence ratio, ignition, and temperature.

A detailed assessment of differences in combusting spray structure and emissions between diesel and biodiesel fuels was also presented. Reacting biodiesel sprays exhibit longer liquid lengths and flame lift-off lengths relative to conventional diesel, and slower evaporation under equivalent engine operating conditions can result in longer effective ignition delays, even if the fuel chemical kinetics are generally faster. For the specific engine and operational conditions considered, the quasidimensional spray model using appropriate fuel property data and a detailed chemical kinetic mechanism for biodiesel always showed lower NO_x across the range of engine speeds and loads considered. This outcome is in line with some experiments and modeling in the literature, but goes against an tepid consensus regarding the biodiesel NO_x penalty. Consequently, it seems that the biodiesel NO_x effect is not easily accounted for by a handful of key fuel properties or chemical kinetic behavior, but must be inextricably tied to the combination of fuel characteristics and engine operating parameters. The variety of results reported in the literature, this work included, would appear to support this conjecture.

Current shortcomings notwithstanding, the modeling approach provides a viable platform for considering a number of complex combustion processes. The model could be generalized to multiple injections, adapted to different kinetic mechanisms for alternative fuels, and used to consider dual fuel strategies with a premixed port injected charge ignited by micropilot sprays. Finally, the relatively low computational burden relative to full multidimensional spray combustion modeling, while sacrificing some accuracy, is a great advantage for quickly exploring and making sense of a large number of scenarios in a tractable manner.

Several avenues of further investigation are warranted:

- (1) Improvement of the phenomenological parcel mixing model to better predict peak premixed burn heat release,
- (2) Inclusion of injector dynamics to more accurately predict actual fuel injector nozzle mass flow rate profiles,
- (3) Improved models of soot formation and oxidation for both diesel and biodiesel fuels that are ideally incorporated into the chemical kinetic mechanism,
- (4) Improved reduced chemical kinetic models for biodiesel blends that include both thermal and prompt NO_x chemistries and can reliably model fuels with a range of iodine numbers,
- (5) Appropriate correlations for biodiesel droplet breakup and size distributions,
- (6) Inclusion of multicomponent droplet evaporation models that offer preferential evaporation to certain species along the distillation curve that may have different chemical kinetic impacts,
- (7) Analytical or experimental determination of proper gas jet model constants K and K_u that are appropriate for high pressure liquid fuel sprays,

- (8) Comparison of pressure and heat release rate predictions with multidimensional CFD models of the same engines,
- (9) Addition of intake and exhaust stroke modeling to compute the residual fraction and cylinder pressure at the start of injection.

Numerical modeling along these lines may offer clues and further data points to better understand the particulars of diesel and biodiesel combustion and emissions formation processes. As a practical tool for engine designers, the new model presented in this work offers a predictive and efficient method to better inform engine designs in the highly regulated emissions and efficiency environment of today and the near future.

REFERENCES

- [1] U.S. Energy Information Administration. *Annual Energy Outlook 2014 with Projections to 2040*. DOE/EIA-0383(2014), 2014.
- [2] Shi, Y.; Ge, H.; Reitz, R.; *Computational Optimization of Internal Combustion Engines*. Springer-Verlag, London, 2010.
- [3] Los Alamos National Laboratory. *KIVA-4 CFD Code*. <http://www.lanl.gov/orgs/t/t3/codes/kiva.shtml>. 2014.
- [4] Convergent Science, Inc.; *CONVERGE CFD Software with Automatic Meshing and Adaptive Mesh Refinement*. <http://www.convergecf.com/products/converge/>. 2014.
- [5] Heywood, J. B. *Internal Combustion Engine Fundamentals*. McGraw-Hill, Inc. New York, 1988.
- [6] Borman, G. L.; Ragland, K. W. *Combustion Engineering*. McGraw-Hill, Inc. New York, 1998.
- [7] Ferguson, C. R.; Kirkpatrick, A. T.; *Internal Combustion Engines: Applied Thermosciences*. John Wiley & Sons, Ltd., 3rd ed., 2016.
- [8] Dec, J. E.; *A Conceptual Model of DI Diesel Combustion Based on Laser Sheet Imaging*. SAE Technical Paper 970873, 1997.
- [9] Assanis, D. N.; Heywood, J. B.; *Development and Use of a Computer Simulation of the Turbocompounded Diesel System for Engine Performance and Component Heat Transfer Studies*. SAE Technical Paper 860329, 1986.
- [10] Hiroyasu, H.; Kadota, T.; *Models for Combustion and Formation of Nitric Oxide and Soot in Direct Injection Diesel Engines*. SAE Technical Paper 760129, 1976.

- [11] Hiroyasu, H.; Kadota, T.; Arai, M.; *Development and Use of a Spray Combustion Modeling to Predict Diesel Engine Efficiency and Pollutant Emissions: Part 1, Combustion Modeling*. Bulletin of the JSME, vol.26, no.214-12, pp.569-575, 1983.
- [12] Hiroyasu, H.; Kadota, T.; *Development and Use of a Spray Combustion Modeling to Predict Diesel Engine Efficiency and Pollutant Emissions: Part 2, Computational Procedure and Parametric Study*. Bulletin of the JSME, vol.26, no.214-13, pp.576-583. 1983.
- [13] Ranz, W.E.; Marshall, W.R.; *Evaporation from Drops*. Chemical Engineering Progress, vol.48, no.3, pp.141-146, 1952.
- [14] Borman, G.L.; Johnson, J.H.; *Unsteady Vaporization Histories and Trajectories of Fuel Drops Injected into Swirling Air*. SAE Technical Paper 620271, 1962.
- [15] Elkotb, M.M. *Fuel Atomization for Spray Modelling*. Prog. Energy Combust. Sci., vol.8, pp.61-91, 1982.
- [16] Arai, M.; Tabata, M.; Hiroyasu, H.; Shimizu, M.; *Disintegrating Process and Spray Characterisation of Fuel Jet Injected by a Diesel Nozzle*. SAE Technical Paper 840275, 1984.
- [17] Hiroyasu, H.; Kadota, T.; *Fuel Droplet Size Distribution in Diesel Combustion Chamber*. SAE Technical Paper 740715, 1974.
- [18] Hiroyasu, H.; Arai, M.; Tabata, M.; *Empirical Equations for the Sauter Mean Diameter for a Diesel Spray*. SAE Technical Paper 890464, 1989.
- [19] Hiroyasu, H.; Nishida, H.; *Fuel Spray Trajectory and Dispersion in a D.I. Diesel Combustion Chamber*. SAE Technical Paper 890462, 1989.
- [20] Nishida, K.; Hiroyasu, H.; *Simplified Three-Dimensional Modeling of Mixture Formation and Combustion in a D.I. Diesel Engine*. SAE Technical Paper 890269, 1989.

- [21] Bazari, L.; *A DI Diesel Combustion and Emission Predictive Capability for Use in Cycle Simulation*. SAE Technical Paper 920462, 1992.
- [22] Rakopoulos, C.D.; Hountalas, D.T.; Taklis, G.N.; Tzanos, E.I.; *Analysis of Combustion and Pollutants Formation in a Direct Injection Diesel Engine Using a Multi-zone Model*. Intl. J. Energy Res., vol.19, pp.63-88, 1995.
- [23] Kouremenos, D.A.; Rakopoulos, C.D.; Karvounis, E.; *Thermodynamic Analysis of Direct Injection Diesel Engines by Multi-zone Modeling*. ASME Energy Systems Conference, vol.3, pp.67-77, 1987.
- [24] Kouremenos, D.A.; Rakopoulos, C.D.; Hountalas, D.T.; *Multi-zone Combustion Modeling for the Prediction of Pollutants Emissions and Performance of DI Diesel Engines*. SAE Technical Paper 970635, 1997.
- [25] Jung, D.; Assanis, D.; *Multi-zone DI Diesel Spray Combustion Model for Cycle Simulation Studies of Engine Performance and Emissions*. SAE Technical Paper 2001-01-1246, 2001.
- [26] Jung, D.; Assanis, D.; *Quasidimensional Modeling of Direct Injection Diesel Engine Nitric Oxide, Soot, and Unburned Hydrocarbon Emissions*. ASME J. Gas Turbines & Power, vol.128, 2006.
- [27] Rezaei, R.; Eckert, P.; Seebode, J.; Behnk, K.; *Zero-dimensional Modeling of Combustion and Heat Release in DI Diesel Engines*. SAE Technical Paper 2012-01-1065, 2012.
- [28] Rajkumar, S.; Bakshi, S.; Mehta, P. S. *Multizone Phenomenological Modeling of Combustion and Emissions for Multiple-Injection Common Rail Direct Injection Diesel Engines*. ASME J. Gas Turb. & Power, vol.138, 2016.

- [29] Ricou, F.; Spalding, D.; *Measurements of entrainment by axisymmetrical turbulent jets*. J. Fluid Mech., vol.11, pp.21-32, 1961.
- [30] Abramovich, G.; *Effect of Solid-Particle or Droplet Admixture on the Structure of a Turbulent Gas Jet*. Int. J. Heat Mass Transfer, vol.13, pp.1039-1045, 1969.
- [31] Rife, J.; Heywood, J.; *Photographic and Performance Studies of Combustion with a Rapid Compression Machine*. SAE Technical Paper 740948, 1974.
- [32] Abraham, J.; Magi, V.; Macinnes, J.; Bracco, F.; *Gas Versus Spray Injection: Which Mixes Faster?* SAE Technical Paper 940895, 1994.
- [33] Post, S.; Iyer, V.; Abraham, J.; *A Study of Near-Field Entrainment in Gas Jets and Sprays Under Diesel Conditions*. ASME J. Fluids Engr., vol.122, 2000.
- [34] Hill, P.; Ouellette, P.; *Transient Turbulent Gaseous Fuel Jets for Diesel Engines*. J. Fluids Engr., vol.121, 1999.
- [35] Ouellette, P.; Hill, P.; *Turbulent Transient Gas Injections*. ASME J. Fluids Engr., vol.122, 2000.
- [36] Malmstrom, T.; Kirkpatrick, A.; Christensen, B.; Knappmiller, K.; *Centreline velocity decay measurements in low-velocity axisymmetric jets*. J. Fluid Mech., vol.246, pp.363-377, 1997.
- [37] Desantes, J.; Payri, R.; Salvador, F.; Gil, A.; *Development and validation of a theoretical model for diesel spray penetration*. Fuel, vol.85, pp.910-917, 2005.
- [38] Sazhin, S.; Feng, G.; Heikal, M.; *A model for fuel spray penetration*. Fuel, vol.80, 2001.
- [39] Kirkpatrick, A.; Ferguson, C.; *Internal Combustion Engines: Applied Thermosciences*. John Wiley & Sons, forthcoming 4th ed., est. 2019.

- [40] Dent, J. C.; Derham, J. A.; *Air Motion in a Four-stroke Direct Injection Diesel Engine*. Proc Instn Mech Engrs vol.188, 1974.
- [41] Kee, R. J.; Rupley, F. M.; Miller, J.A.; *Chemkin-II: A Fortran Chemical Kinetics Package for the Analysis of Gas-Phase Chemical Kinetics*. Sandia National Laboratories Report SAND89-8009, 1989.
- [42] Goodwin, D.; *Cantera: an object-oriented software toolkit for chemical kinetics, thermodynamics, and transport processes*, Caltech, Pasadena, CA, 2009.
- [43] Ra, Y.; Reitz, R.; 2008. *A reduced chemical kinetic model for IC engine combustion simulations with primary reference fuels*. Combustion & Flame, v.155, pp.713-738.
- [44] Wang, H.; Yao, M.; Reitz, R. D.; *Development of a Reduced Primary Reference Fuel Mechanism for Internal Combustion Engine Combustion Simulations*, Energy & Fuels, vol.27, 2013.
- [45] Hindmarsh, A. C.; Brown, P. N.; Grant, K. E.; Lee, S. L.; Serban, R.; Shumaker, D. E.; Woodward, C. S.; *SUNDIALS: Suite of Nonlinear and Differential/Algebraic Equation Solvers*, ACM Transactions on Mathematical Software, 31(3), pp. 363-396, 2005.
- [46] Lumley, J.L. *Engines: An Introduction*. Cambridge University Press, 1999.
- [47] Woschni, G.; *A Universally Applicable Equation for the Instantaneous Heat Transfer Coefficient in the Internal Combustion Engine*. SAE Technical Paper 670931, 1967.
- [48] Mansouri, S.; Heywood, J.; *Correlations for the Viscosity and Prandtl Number of Hydrocarbon-Air Combustion Products*. Comb. Sci. & Tech, vol.23, pp.251-256, 1980.
- [49] Kong, S.C.; Marriott, C. D.; Reitz, R. D.; *Modeling and Experiments of HCCI Engine Combustion Using Detailed Chemical Kinetics with Multidimensional CFD*. SAE Technical Paper 2001-01-1026, 2001.

- [50] Kong, S.C.; Han, Z.; Reitz, R.D.; *The Development and Application of a Diesel Ignition and Combustion Model for Multidimensional Engine Simulation*. SAE Technical Paper 950278, 1995.
- [51] Han, Z.; Parrish, S.; Farrell, P.; Reitz, R. *Modeling Atomization Processes of Pressure Swirl Hollow-Cone Fuel Sprays*. *Atomization and Sprays*, vol.7, pp.663-684, 1997.
- [52] Han, Z.; Reitz, R.; Claybaker, P.; Rutland, C.; Yang, J.; Anderson, R.; *Modeling the Effects of Intake Flow Structures on Fuel/Air Mixing in a Direct-Injected Spark-Ignition Engine*. SAE Technical Paper 961192, 1996.
- [53] Hiroyasu, H.; Kadota, T.; *Development and Use of a Spray Combustion Modeling to Predict Diesel Engine Efficiency and Pollutant Emissions - Part I, Combustion Modeling*. *Bulletin of the JSME*, Vol.26, No.214, April, 1983.
- [54] Borman, G. L.; *Internal Combustion Engine Heat Transfer*. *Prog. Energy Combust. Sci.* vol.13, pp.1-46, 1987.
- [55] Chomiak, J.; Karlsson, A.; *Flame Liftoff in Diesel Sprays*. Twenty-Sixth Symposium (International) on Combustion, the Combustion Institute, pp.2557-2564, 1996.
- [56] Siebers, D.; *Scaling Liquid-Phase Fuel Penetration in Diesel Sprays Based on Mixing-Limited Vaporization*. SAE Technical Paper 1999-01-0528, 1999.
- [57] Siebers, D.; Higgins, B.; *Flame Lift-Off on Direct-Injection Diesel Sprays Under Quiescent Conditions*. SAE Technical Paper 2001-01-0530, 2001.
- [58] Campbell, J.; Gosman, A.; Hardy, G.; *Analysis of Premix Flame and Lift-Off in Diesel Spray Combustion using Multi-Dimensional CFD*. SAE Technical Paper 2008-01-0968, 2008.

- [59] Nehmer, D. A.; Reitz, R. D.; *Measurement of the Effect of Injection Rate and Split Injections on Diesel Engine Soot and NO_x Emissions*. SAE Technical Paper 940668, 1994.
- [60] Patterson, M. A.; Kong, S. C.; Hampson, G. J.; Reitz, R. D.; *Modeling the Effects of Fuel Injection Characteristics on Diesel Engine Soot and NO_x Emissions*. SAE Technical Paper 940523, 1994.
- [61] Kong, S. C.; Sun, Y.; Reitz, R. D.; *Modeling Diesel Spray Flame Liftoff, Sooting Tendency, and NO_x Emissions Using Detailed Chemistry With Phenomenological Soot Model*. ASME J. Gas Turbines & Power, vol.129, pp.245-251, 2007.
- [62] Smith, G. P.; Golden, D. M.; Frenklach, M.; Moriarty, N.; Eiteneer, B.; Goldenberg, M.; Bowman, C.; Hanson, R.; Song, S.; Gardiner, W.; Lissianski, V.; Qin, Z.; *GRI-Mech 3.0*, http://www.me.berkeley.edu/gri_mech/, accessed June 2016.
- [63] Graboski, M.; McCormick, R.; *Combustion of Fat and Vegetable Oil Derived Fuels in Diesel Engines*. Prog. Energy Combust. Sci. vol.24, pp.125-164, 1998.
- [64] McCormick, R.; Alvarez, J.; Graboski, M.; *NO_x Solutions for Biodiesel*. NREL Technical Report SR-510-31465, 2003.
- [65] Chakravarthy, K.; McFarlane, J.; Daw, S.; Ra, R.; Reitz, R.; Griffin, J.; *Physical Properties of Biodiesel and Implications for use of Biodiesel in Diesel Engines*. SAE Technical Paper 2007-01-4030, 2007.
- [66] Ra, Y.; Reitz, R.; McFarlane, J.; Daw, S.; *Effects of Fuel Physical Properties on Diesel Engine Combustion using Diesel and Biodiesel Fuels*. SAE Technical Paper 2008-01-1379, 2008.

- [67] Fisher, E.; Pitz, W.; Curran, H.; Westbrook, C.; *Detailed Chemical Kinetic Mechanisms for Combustion of Oxygenated Fuels*. Proceedings of The Combustion Institute, vol.28, pp.1579-1586, 2000.
- [68] Vaughn, T.; Hammill, M.; Harris, M.; Marchese, A.; *Ignition Delay of Bio-Ester Fuel Droplets*, SAE Technical Paper 2006-01-3302, 2006.
- [69] Gail, S.; Thomson, M.; Sarathy, S., Syed, S., Dagaut, P., Dievart, P., Marchese, A.; Dryer, F.; *A Wide-Ranging Kinetic Modeling Study of Methyl Butanoate Combustion* Proc. Combust. Inst., vol.31, no.1, pp.305-311, 2007.
- [70] Herbinet, O.; Pitz, W.; Westbrook, C.; *Detailed Chemical Kinetic Oxidation Mechanism for a Biodiesel Surrogate* Combust. Flame, vol.154, no.3, pp.507-528, 2008.
- [71] Sarathy, S.; Thomson, M.; Pitz, W.; Lu, T.; *An Experimental and Kinetic Modeling Study of Methyl Decanoate Combustion*. Lawrence Livermore National Laboratory, LLNL-CONF-424403, 2010.
- [72] Herbinet, O.; Pitz, W.; Westbrook, C.; *Detailed Chemical Kinetic Mechanism for the Oxidation of Biodiesel Fuels Blend Surrogate* Combust. Flame, vol.157, no.5, pp.893-908, 2010.
- [73] Brakora, J.; *A Comprehensive Combustion Model for Biodiesel-fueled Engine Simulations*. PhD Thesis, University of Wisconsin-Madison, 2012.
- [74] Brakora, J.; Reitz, R.; *A Comprehensive Combustion Model for Biodiesel-fueled Engine Simulations*. SAE Technical Paper 2013-01-1099, 2013.
- [75] Fenimore, C.; *Formation of Nitric Oxide in Premixed Hydrocarbon Flames*. 13th Intl. Symposium on Combustion, The Combustion Institute, Pittsburgh, pp.373-379, 1971.

- [76] Lapuerta, M.; Armas, O.; Rodriguez-Fernandez, J.; *Effect of biodiesel fuels on diesel engine emissions*. Prog. Energy & Combust. Sci., vol.34, pp.198-223, 2008.
- [77] Cheng, A.; Upatnieks, A.; Mueller, C.; *Investigation of the Impact of Biodiesel Fuelling on NO_x Emissions Using and Optical Direct Injection Diesel Engine*, Int. J. Engine Res., vol.7, pp.297-318, 2006.
- [78] Lai, J.; Lin, K.; Violi, A.; *Biodiesel combustion: Advances in chemical kinetic modeling*. Prog. Energy and Combustion Sci., vol.37, pp.1-14, 2011.
- [79] Moscherosch, B.; Polonowski, C.; Miers, S.; Naber, J.; *Combustion and Emissions Characterisation of Soy Methyl Ester Biodiesel Blends in an Automotive Turbocharged Diesel Engine*. ASME J. Engr. Gas Turbines & Power, vol.132, 2010.
- [80] Osborne, D.; Fritz, S.; Glenn, D.; *The Effects of Biodiesel Fuel Blends on Exhaust Emissions from a General Electric Tier 2 Line-Haul Locomotive*. ASME J. Engr. Gas Turbines & Power, vol.133, 2011.
- [81] Senatore, A.; Cardone, M.; Rocco, V.; Prati, M.; *A Comparative Analysis of Combustion Process in DI Diesel Engine Fueled with Biodiesel and Diesel Fuel*. SAE Technical Paper 2000-01-0691, 2000.
- [82] Brakora, J.; Reitz, R.; *Investigation of NO_x Predictions from Biodiesel-fueled HCCI Engine Simulations Using a Reduced Kinetic Mechanism*. SAE Technical Paper 2010-01-0577, 2010.
- [83] Rakopoulos, C.; Hountalas, D.; Zannis, T.; *Theoretical Study Concerning the Effect of Oxygenated Fuels on DI Diesel Engine Performance and Emissions*. SAE Technical Paper 2004-01-1838, 2004.

- [84] Zheng, J.; *Use of an Engine Cycle Simulation to Study a Biodiesel Fueled Engine*. Master's Thesis, Texas A&M University, 2009.
- [85] Gogoi, T.; Baruah, D.; *A cycle simulation model for predicting the performance of a diesel engine fueled by diesel and biodiesel blends*. Energy, vol.35, pp.1317-1323, 2010.
- [86] Abbe, C.; Nzungwa, R.; Danwe, R.; Ayissi, Z.; Obonou, M.; *A study on the 0D phenomenological model for diesel engine simulation: Application to combustion of Neem methyl ester biodiesel*. Energy Conv. & Mgmt., vol.89, pp.568-576, 2015.
- [87] Li, J.; Han, Z.; Shen, C.; Lee, C.; *A Study on Biodiesel NO_x Emission Control with the Reduced Chemical Kinetics Model*. ASME J. Engr. Gas Turbines & Power. vol.136, 2014.
- [88] Yang, J.; Golovithcev, V.; Naik, C.; Meeks, E.; *Comparative Study of Diesel Oil and Biodiesel Spray Combustion Based on Detailed Chemical Mechanisms*. ASME J. Engr. Gas Turbines & Power, vol.136, 2014.
- [89] Zhu, H.; Bohac, S.; Huang, Z., Assanis, D.; *Defeat of the Soot/NO_x Trade-off Using Biodiesel-Enthanol in a Moderate Exhaust Gas Recirculation Premixed Low-Temperature Combustion Mode*. ASME J. Engr. Gas Turbines & Power, vol.135, 2013.
- [90] McGill, R.; Storey, J.; Wagner, R.; Irick, D.; Aakko, P.; Westerholm, M.; Nylund, N.; Lappi, M.; *Emission Performance of Selected Biodiesel Fuels*. SAE Technical Paper 2003-01-1866, 2003.
- [91] Sharp, C.; Howell, S.; Jobe, J.; *The Effect of Biodiesel Fuels on Transient Emissions From Modern Diesel Engines, Part I Regulated Emissions and Performance*. SAE Technical Paper 2000-01-1967, 2000.

- [92] Mueller, C.; Boehman, A.; Martin, G.; *An Experimental Investigation of the Origin of Increased NO_x Emissions When Fueling a Heavy-duty Compression-ignition Engine with Soy Biodiesel*. SAE Technical Paper 2009-01-1792, 2009.
- [93] Musculus, M.; *Effects of the In-Cylinder Environment on Diffusion Flame Lift-Off in a DI Diesel Engine*. SAE Technical Paper 2003-01-0074, 2003.
- [94] McCormick, R.; Graboski, M.; Alleman, T.; Herring, A.; *Impact of Biodiesel Source Material and Chemical Structure on Emissions of Criteria Pollutants from a Heavy-Duty Engine*. Environ. Sci. Tech. vol.35, pp.1742-1747, 2001.
- [95] McCormick, R.; Tennant, C.; Hayes, R.; Black, S.; Ireland, J.; McDaniel, T.; Williams, A.; Frailey, M.; Sharp, C.; *Regulated Emissions from Biodiesel Tested in Heavy-Duty Engines Meeting 2004 Emissions Standards*. SAE Technical Paper 2005-01-2200, 2005.
- [96] Lapuerta, M.; Armas, O.; Rodriguez-Fernandez, J.; *Effect of the Degree of Unsaturation of Biodiesel Fuels on NO_x and Particulate Emissions*. SAE Technical Paper 2008-01-1676, 2008.